THE ENDOPLASMIC RETICULUM STRESS RESPONSE IN THE PROGRESSION OF SANDHOFF DISEASE

THE ENDOPLASMIC RETICULUM STRESS RESPONSE IN THE PROGRESSION OF SANDHOFF DISEASE

BY: FIONA WEAVER, B.Sc.

A Thesis Submitted to the School of Graduate Studies in Partial Fulfilment of the Requirements for the Degree of Master of Science

McMaster University MASTER OF SCIENCE (2021) Hamilton, Ontario (Biology)

TITLE: The Endoplasmic Reticulum Stress Response in the Progression of Sandhoff Disease.

AUTHOR: Fiona Weaver
SUPERVISOR: Professor Suleiman Igdoura
PAGES: 146

LAY ABSTRACT

Lysosomal storage diseases are a rare group of inherited neurological disorders that are often fatal at a young age. Two diseases that fall within this category, Sandhoff and Tay Sachs disease, are similar in their cause and symptoms. Current research lacks a complete understanding of the mechanism behind these disorders making the development of new therapeutics challenging. This research highlights a group of cells in the spine that are vulnerable in these diseases. These cells show physical and functional changes in their structure as the diseases progress. We provide evidence of a new stress pathway which appears to be strongly implicated in the development and progression of these diseases. We also show an association between this pathway and the death of these vulnerable cells leading to the symptoms exhibited by patients. These findings expand our current knowledge of these disorders and open new avenues for therapeutic interventions.

ABSTRACT

Sandhoff disease (SD), a fatal lysosomal storage disease, results from a deficiency of the β-subunit of the β-hexosaminidase A and B enzymes. This deficiency leads to severe accumulation of GM2 gangliosides in lysosomes within the central nervous system (CNS) resulting in mass neuronal apoptosis. The mouse model of SD shows progressive neurodegeneration that closely resembles Sandhoff and Tay Sachs disease (TSD) in humans. SD and TSD consist of infantile, juvenile, and late-onset forms. These diseases can present with a multiplicity of symptoms including cognitive and speech impairments, ataxia, and lower motor neuron disease. Late-onset SD and TSD show motor neuron disease in over 40% of patients. In this study, we explore the role of endoplasmic reticulum (ER) stress and the unfolded protein response (UPR) in the spinal cord during the development and progression of disease in Sandhoff mice. Using immunocytochemistry and western blotting, we analyzed the expression level and localization of several ER stress and cellular apoptosis markers within the cervical, thoracic, and lumbar regions of the spinal cord of Sandhoff mice. Our results revealed significant upregulation of several ER stress markers in motor neurons that appeared to coincide with significant lysosomal accumulations. In addition, we observed sequential and age-dependent expression changes in ATF6 and CHOP and their prominent nuclear localization within anterior horn motor neurons. Markers of apoptosis, caspases and PARP also appeared to be activated in the spinal cords of Sandhoff mice starting as early as 60 days. Interestingly, we noted more than 50% reduction in neuronal numbers in all regions

of the spinal cord of Sandhoff mice between ages 80 and 120 days. Overall, this study

provides strong evidence for the role of chronic ER stress and UPR activation in the spine

pathophysiology of SD.

ACKNOWLEGDEMENTS

First and foremost, I would like to thank my supervisor Dr. Suleiman Igdoura. His unparalleled dedication and support over the past year has allowed me to grow exponentially as a researcher. He continued to challenge me to push the boundaries I had set for myself, as well as push the boundaries of research in the field. His unwavering encouragement and vast knowledge of life allowed for me to be successful. I will forever be grateful for his wisdom and for the experiences I had while in his lab. Next, I would like to thank the past and current members of Dr. Igdoura's lab. I also want to acknowledge my fellow lab mates, Allyson Peak, Rimika Sachdeva, and Johanna Enright, for their help with experiments and for accompanying me in the lab.

Next, I would like to thank my co-supervisor, Dr. Colin Nurse, as well as my committee members, Dr. Judith West-Mays and Dr. Richard Austin for their interest, enthusiasm, and contribution towards my project.

Lastly, I would like to thank my parents and my sister for motivating and encouraging me throughout the past two years. Thank you for always listening to me talk about my research and for your hours of dedication to help me through not only this endeavor, but my entire life. I am unbelievably lucky to have such wonderful and compassionate people in my life.

Table of contents

LIST OF FIGURES

ABBREVIATIONS

4-PBA	4-Phenylbutyric Acid
AAV	Adeno-Associated Virus
AHN	Anterior Horn Neuron
ALP	Autophagy-lysosome pathway
ALS	Amyotrophic Lateral Sclerosis
ASK1	Apoptosis Signal-Regulating Kinase 1
ATF4	Activating Transcription Factor 4
ATF6	Activating Transcription Factor 6
B-gal	β-galactosidase
Bcl-2	B-Cell Lymphoma 2
Bim	Bcl-2-Like Protein 11
BMT	Bone Marrow Transplant
c-Cas7	Cleaved Caspase 7
Ca^{2+}	Calcium
CAF	Central Animal Facility
CHOP	C/EBP Homologous Protein
CLEAR	Coordinated Lysosomal Expression and Regulation Network
CNS	Central Nervous System
DKO	Double Knockout
DNA	Deoxyribonucleic Acid
eIF2α	Eukaryotic Translation Initiation Factor 2α
ER	Endoplasmic Reticulum
Ero1-α	Endoplasmic Reticulum Oxidoreductase-1
ERT	Enzyme Replacement Therapy
GADD34	Growth Arrest and DNA Damage-Inducible 34
GBA	Glucocerebrosidase
GFAP	Glial Fibrillary Acidic Protein
GRP78	Glucose Regulated Protein 78
GRP94	Glucose Regulated Protein 94
HEXA	β-Hexosaminidase A
HEXB	β-Hexosaminidase B
IP3R	Inositol 1,4,5-Triphosphate Receptor
iPSC	Induced Pluripotent Stem Cell
IRE1	Inositol Requiring Enzyme 1
JNK	Jun-N-Terminal Kinase
LAMP2	Lysosomal Membrane Associated Protein 2
LDCD	Lysosomal-dependent cell death
LMN	Lower motor neuron
LMP	Lysosomal membrane permeabilization

LSDs	Lysosomal Storage Diseases
MAMs	Mitochondrial associated ER-Membranes
MAPK	Mitogen Activated Protein Kinase
MCS	Membrane Contact Sites
MPS II	Mucopolysaccharidosis II
mTOR	Mammalian Target of Rapamycin
NeuN	Neuronal Nuclei
NPC	Niemann-Pick Disease Type C
NSAIDs	Nonsteroidal Anti-Inflammatory Drugs
PARP	Poly(ADP-Ribose) Polymerase
PCR	Polymerase Chain Reaction
PDI	Protein Disulfide Isomerase
PERK	PKR-like endoplasmic reticulum kinase
RIDD	Regulated IRE1-Dependent Decay
RNA	Ribonucleic Acid
ROS	Reactive Oxygen Species
RYR	Ryanodine Receptor
S1P	Site Specific Protease 1
S2P	Site Specific Protease 2
SD	Sandhoff Disease
SERCA	Sarco- Endoplasmic Reticulum Ca^{2+} ATP-ase
siRNA	Small Interfering RNA
SNARE	SNAP Receptor
SOCE	Store Operated Ca^{2+} Entry
STIM	Stromal-Interacting Molecule
TFEB	Transcription Factor EB
TMAO	Trimethylamine-N-oxide
Tnfα	Tumor Necrosis Factor α
TRAF2	Tumor Necrosis Factor Receptor Associated Factor 2
TRPML-1	Mucolipin TRP Channel 1
TSD	Tay Sachs Disease
TUDCA	Turoursodeoxycholic
UPR	Unfolded Protein Response
XBP1	X-Box Binding Protein 1

DECLARATION

All work was performed by Fiona Weaver.

CHAPTER ONE

INTRODUCTION

Sandhoff disease (SD), a fatal lysosomal storage disease, results from a deficiency of the β-subunit of the β-hexosaminidase A and B enzymes. This deficiency leads to severe accumulation of GM2 gangliosides in lysosomes within the central nervous system (CNS) resulting in mass neuronal apoptosis. The mouse model of SD shows progressive neurodegeneration that closely resembles Sandhoff and Tay Sachs disease (TSD) in humans. SD and TSD consist of infantile, juvenile, and late-onset forms. These diseases can present with a multiplicity of symptoms including cognitive and speech impairments, ataxia, and lower motor neuron disease. Late-onset SD and TSD show motor neuron disease in over 40% of patients. Lysosomes, the endoplasmic reticulum (ER) and the unfolded protein response (UPR) are tightly interconnected during the onset and progression of SD and work concurrently to cause neurodegeneration.

LITERATURE REVIEW

Endoplasmic Reticulum

The largest organelle in the cell, the ER, is an extremely dynamic structure that plays a major role in a vast range of cellular functions which work in concert, under tight regulation, to maintain homeostasis. This multifunctional organelle requires specific proteins and a distinct structural makeup to complete its roles in calcium (Ca^{2+}) signaling, lipid biogenesis, and protein synthesis and folding [1]. The vitality of the ER to proper

cellular function means the ER must be able to rapidly respond to changes in the intracellular environment and coordinate with a range of other organelles [2]. The structural layout of the ER consists of the nuclear envelope and the peripheral ER which is further divided into rough sheets and smooth tubules [1]. Different cell types, depending on their main functions, will have varying ratios of tubules to sheets to accommodate their individualistic needs. The rough sheets of the ER are the main site of protein synthesis, protein folding, and post-translational modifications and are defined by the high density of ribosomes present [1]. In contrast the tubules have very few ribosomes and are defined by the three-way junctions which connect the individual tubules within the network [1]. This complex system of tubules is extremely dynamic, constantly rearranging and growing to maintain optimal ER functionality. In a recent study by Lu and colleagues, it was established that this dynamic ER remodeling seen within cells is actively driven by lysosomes [3]. Lysosomes were able to sense changes in the intracellular environment, such as metabolic changes, and repositioned accordingly in response to these alterations. This ultimately led to the redistribution of ER tubules and changes in the ERs global morphology [3]. This clearly demonstrates the tight interconnectivity that occurs between cellular organelles. ER can also interact with a multitude of other organelles, including the plasma membrane, mitochondria, peroxisomes, and Golgi, by forming membrane contact sites (MCSs) [4-7]. These contact sites allow the ER to communicate and coordinate with organelles to align their functions from which emerges a harmonized collection of functions that work in concert to maintain cellular homeostasis

[7-9]. Since the ER has such a central role in cellular function, if any part of its process is disturbed it can initiate a series of events such as ER stress and the unfolded protein response which can result in cell death and disease.

ER Stress and the Unfolded Protein Response

The ER is essential for maintaining cell functionality and homeostasis as it is vital for protein folding, lipid synthesis, and Ca^{2+} storage and release [4]. When homeostasis is disrupted through either inflammation, accumulation of unfolded proteins, oxidative stress, or other ER stressors, the UPR becomes activated (Figure 1). There are three transmembrane proteins constituting three arms of the UPR which are: inositol-requiring enzyme 1 (IRE1), PKR-like endoplasmic reticulum kinase (PERK), and activating transcription factor 6 (ATF6). Each of these proteins are held inactive by a resident ER chaperone protein, glucose regulated protein 78 (GRP78). After ER stress initiation, GRP78 is sequestered away from these proteins to help with the load of unfolded proteins, activating the three arms of the UPR [4, 10, 11]. Each arm utilizes unique signal transduction pathways, but they work concurrently to downregulate protein synthesis, increase the ER's folding and clearance capacities, and increase the synthesis of chaperones and foldases. Ultimately, the UPR aims to protect cells from stress and restore ER homeostasis.
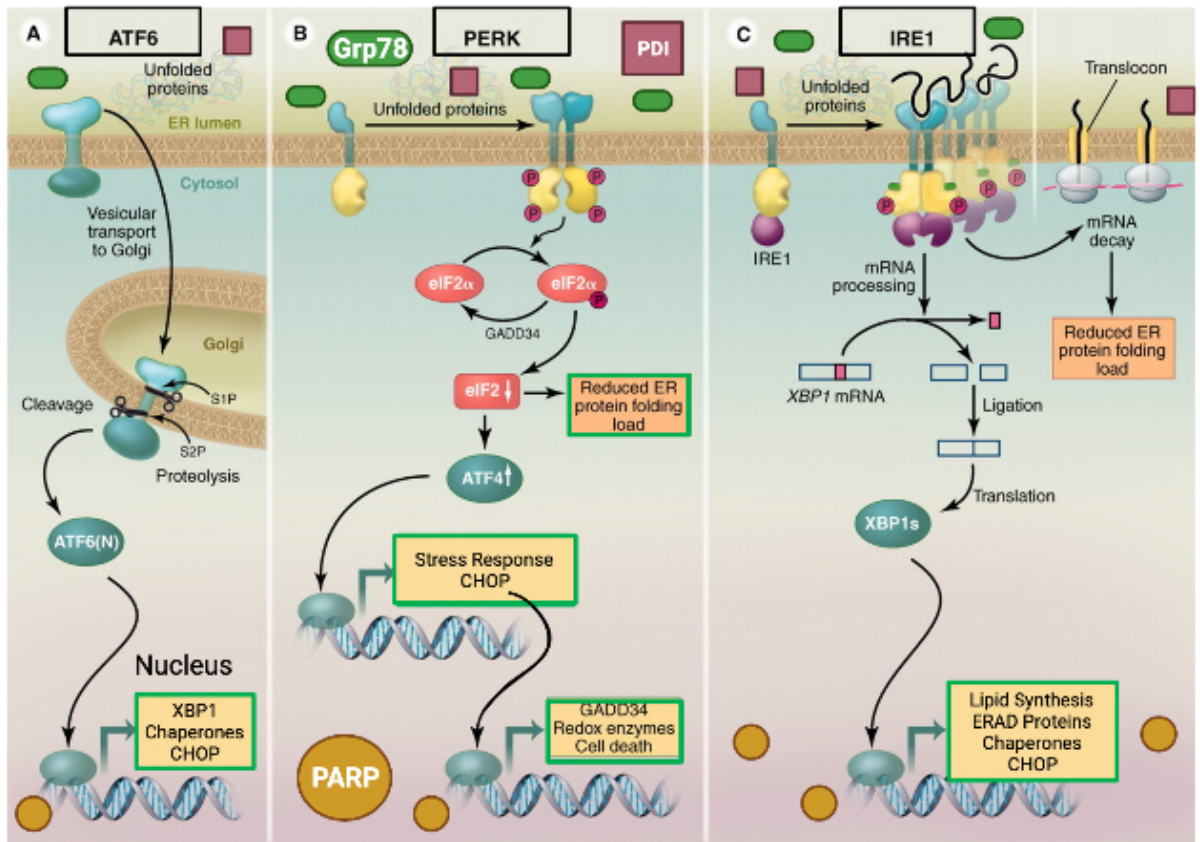
Figure 1. The three branches of the UPR and intracellular localization of various ER stress markers. Within the ER lumen, ER chaperone proteins are present including GRP78 (green ovals) and PDI (burgundy squares). These proteins play pivotal roles in protein folding, Ca^{2+} homeostasis, and sensing ER stress. Anchored within the membrane of the ER are three unique signal transducers (ATF6, PERK, and IRE-1) which become activated, in response to protein accumulation within the lumen, and transmit information to trigger a cascade of downstream effects, including upregulation of UPR target genes. (**A**) Specifically, ATF6, upon ER stress activation, translocates to the nucleus where it is cleaved releasing its cytosolic N-terminal fragment to move into the nucleus and activate UPR target genes including CHOP and XP1. (**B**) PERK, the second branch of the UPR, oligomerizes, autophosphorylates itself, and phosphorylates the translation initiation factor, eIF2α, inactivating it. This is followed by preferential translation of ATF4, which can upregulate CHOP expression. (**C**) The third and final arm of the UPR is IRE-1. When activated, IRE-1 oligomerizes in the ER membrane and is now able to cleave XBP1 mRNA. This allows for the creation of the active form of XBP1, which acts as a potent transcription factor within the nucleus, upregulating expression of CHOP and other UPR target genes. In the presence of severe and prolonged ER stress, PARP (orange circles), will be localized to the nucleus where its cleavage can initiate a cascade of apoptotic events. Figure adapted from Walter and Ron, 2011.

(i) PKR-like endoplasmic reticulum kinase (PERK) Signaling

The first arm of the UPR is mediated by the ER-resident transmembrane kinase PERK which becomes activated once ER stress has been sensed. PERK, upon the dissociation of GRP78, becomes fully activated through autophosphorylation and then continues to phosphorylate the eukaryotic translation initiation factor (eIF2α) [10-13]. This results in a brief halt of global cell translation to help reduce the protein load within the ER and provide relief. However, this response is short-lived in that specific mRNAs demonstrate preferential translation while eIF2α is inactivated, one of which encodes activating transcription factor 4 (ATF4). The induction of ATF4 translation overrides the global suppression of translation and leads to a greater folding capacity in the ER. Growth arrest and DNA damage-inducible 34 (GADD34) is one target gene of ATF4 that acts against PERK by leading to the dephosphorylation of eIF2α. The second target gene is transcription factor C/EBP homologous protein (CHOP) which has significant involvement in the activation of apoptotic pathways during chronic ER stress [12, 14, 15].

(ii) Inositol-required protein 1 (IRE1) Signaling

IRE1 delineates the second arm of the UPR and becomes activated similarly to PERK. Moving laterally through the ER membrane, IRE1 dimerizes and becomes fully activated through autophosphorylation which stimulates its endoribonuclease activity [10-13]. Activated IRE1 is now able to cleave the mRNA of X-box binding protein (XBP1), a UPR induced transcription factor. This produces a potent transcriptional activator

which can translocate to the nucleus to induce upregulation of a variety of UPR target genes such as ER chaperone proteins and CHOP. IRE1 can play a second role in the alleviation of ER stress through a process known as regulated IRE1-dependent decay (RIDD), in which IRE1 cleaves certain mRNAs or microRNAs to target them for degradation [16]. RIDD provides a potential alternative pathway to reduce protein load and mRNA abundance within the ER, although the actual impact of RIDD on ER stress mitigation has yet to be explained.

(iii) Activating Transcription Factor 6 (ATF6) Signaling

The third and final arm of the UPR is ATF6, an ER resident transmembrane protein. Once ER stress is initiated and unfolded proteins begin to accumulate within the ER, ATF6 is released from GRR78 and is transported to the Golgi apparatus for processing. At the Golgi, two site specific proteases, S1P and S2P, cleave the luminal domain of ATF6 creating transcriptionally active p50ATF6 which translocates to the nucleus [17, 18]. This pathway ultimately upregulates the expression of UPR targets such as chaperones and foldases (GRP78, GRP94, protein disulfide isomerase (PDI)), CHOP, and XBP1. Initially, ATF6 was documented to be strictly prosurvival, working to counteract the effects of ER stress [19]. In more recent literature, a clear association between ATF6 and apoptosis has frequently been reported [17, 20]. While its mechanism of inducing apoptosis, either through CHOP or a cascade of caspases, may vary between cell types and diseases, ATF6 clearly plays an influential role in the induction and execution of cell death.

Overall, the UPR is a concerted cellular response across all three arms, that initially begins as pro-survival to help cope with disruptions in physiological conditions but under chronic stress in which terminally misfolded proteins are accumulating to unmanageable levels, the response will switch to favour apoptosis. The three arms do not directly initiate apoptosis but rather through a series of downstream cascades such as CHOP, PARP, and caspases will trigger cell death.

Lysosomes and Lysosomal Storage Diseases (LSDs):

The lysosome, a membrane-bound organelle, first discovered in the 1950s by Christian de Duve, were originally deemed "suicide bags" because of their acidic pH and the many hydrolases contained within their lumen [21]. Lysosomes are an extremely abundant organelle with between 50-1000 lysosomes present in every mammalian cell and contain more than 60 luminal hydrolases as well as membrane proteins and lysosomal associated proteins [22, 23]. A very rigid view of lysosomes and their function has been upheld with lysosomes consistently being described as the recycling centre of the cell, degrading biological macromolecules. It was defined as a static organelle, solely dedicated to the clearance and recycling of cellular products such as proteins, nucleic acids, lipids, and carbohydrates [24]. Lysosomes were described as a separate entity, isolated and working relatively independent of other organelles within the cell. In the last several years, this narrowed view of lysosomes has been challenged and its role as a vital regulatory hub has been highlighted [21, 22, 24]. To begin, an array of additional lysosomal functions have been described including Ca^{2+} signaling, immunity, metabolic

signaling, and inflammation [21, 23-25]. Lysosomes have also been found to be highly

dynamic, repositioning throughout the cell in response to changes in the intracellular

environment [22, 25]. Lastly, lysosomes can interact and coordinate with other organelles

through two main mechanisms. Lysosomes can fuse with other cellular components and

this process is mediated by the assembly of a trans-SNARE complex and is further

promoted by the release of lysosomal lumen Ca^{2+} [26]. The other method is through non-

fusogenic events, facilitated through the formation of MCSs which ultimately utilize

tethering proteins to bring membranes of organelles into close proximity [8, 27]. This

more complex understanding of lysosomal roles and functions and the knowledge that

lysosomes are tightly integrated into the mechanisms that tirelessly work to maintain

cellular homeostasis implies that these organelles need to be able to adapt to the cellular

environment. EB is a transcription factor (TFEB) that allows for the global control of the

lysosomal network and is also the master regulator of the coordinated lysosomal

expression and regulation (CLEAR) network [28, 29]. Genes involved in lysosomal

biogenesis and degradation, lysosomal acidification, lysosomal Ca^{2+} regulation, the

positioning of lysosomes, and lysosomal exocytosis are among some of the genes

regulated by TFEB [28, 29]. Expanding the boundaries of the knowledge surrounding

lysosomes and their highly complex nature can enforce the understanding of how

lysosomal dysfunction can ultimately result in pathological outcomes. Defects in

lysosomes have been linked to many diseases including cancer, metabolic disorders, and

neurodegenerative diseases but lysosomal dysregulation is most prominently connected with lysosomal storage diseases (LSDs).

LSDs are a heterogeneous collection of inherited, monogenic disorders resulting from specific gene mutations leading to a disruption of lysosomal catabolism and ultimately lysosomal dysfunction. Collectively LSDs have a prevalence of 1 in 5000 to 1 in 5500 of live births, however individually some LSDs are much rarer with a prevalence of 1 in 50000 to 1 in 250000 live births [30]. In total there are 70 disorders that have been described to date, 67 of which are autosomal recessive and 3 are x-linked [30]. These can be further divided into 7 broad categories based on which substrate is accumulating during the disease: 1) Sphingolipidosis, 2) Oligosaccharidosis, 3) Mucopolysaccharidosis, 4) Neuronal Ceroid Lipofuscinosis, 5) Sialic Acid Disorders, 6) Mucolipodosis, and 7) Miscellaneous [31]. These disorders are all characterized by excessive accumulation of a specific substrate because of dysfunctional lysosomes.

Approximately 70% of LSDs are caused by mutations in genes which encode vital lysosomal enzymes while the remaining disorders have defects in activators or associated lysosomal proteins [31, 32]. Mutations within these diseases can vary but generally nonsense mutations have more severe consequences in comparison to missense mutations [31]. This provides a partial explanation for the vast range of severity seen within each disease. These diseases differ not only in mutation and gene affected but also the phenotypic presentation and pathophysiological outcomes. Depending on the specific substrate accumulating, different organs and systems can be impacted leading to a

multiplicity of symptoms, variation in the age of onset and the severity of the symptoms. Gaucher disease, one of the most common LSDs, is caused by mutations in the *GBA* gene leading to the accumulation of glucosylceramide in the lysosomes of macrophages [33]. This accumulation ultimately impacts the reticuloendothelial system, which includes the liver, spleen, and bone marrow, and results in inflammation and dysfunction of these organs [34]. In contrast, GM2 gangliosidoses, a rarer group of LSDs, characteristically presents with accumulation of GM2 ganglioside predominantly within the central nervous system [35]. The localization of this accumulation results in severe neurodegeneration accompanied by gliosis and inflammation [35]. This demonstrates the immense variation both between and within different LSDs. However, there is a connecting feature among this diverse group of disorders. It has been reported that about two-thirds of individuals with an LSD demonstrates significant neurological symptoms and neurodegeneration [36] [37, 38]. This neurodegeneration highlights the extreme vulnerability of neurons to the lysosomal dysfunction and subsequent accumulation seen in these disorders [37]. The fact that neurons rely heavily on lysosomes for the clearance of waste products contributes to their susceptibility to lysosomal dysfunction, but lysosomes have emerged as playing a central role in other vital processes including energy metabolism, Ca^{2+} signaling, and interacting with other organelles to maintain homeostasis [37]. Neurons rely heavily on Ca^{2+} for correct functioning and are therefore extremely sensitive to any alterations in Ca^{2+} levels [39]. This susceptibility of neurons and subsequent neurodegeneration highlights a possible connection between vastly diverse diseases, thereby providing an

opportunity to study neurological involvement and potentially discover therapeutics that could be largely applicable to many LSDs. Therefore, although the initial lysosomal dysregulation plays a significant role in the development of LSDs, processes that are activated as downstream consequences of lysosomal disruption, such as inflammation, mitochondrial dysfunction, ER stress, and Ca^{2+} dysregulation, are also emerging as crucial contributors in these diseases. The question that remains is how these subsequent mechanisms fit into the larger scheme of each disease specifically and how the disease progresses from lysosomal dysfunction and accumulation to the severe and ultimately fatal outcome seen in LSD patients.

GM2 Gangliosidoses

GM2 gangliosidoses are a group of rare, recessively inherited metabolic disorders that result from a deficiency of β-hexosaminidase or the GM2 activator protein leading to GM2 ganglioside accumulation in lysosomes. Included within this classification are two fatal neurodegenerative disorders: TSD and SD [40]. Two genes, HEXA and HEXB, encode the β-hexosaminidase α and β subunits respectively, which dimerize to produce a αβ heterodimer or a ββ homodimer. TSD is a result of a mutation in the HEXA gene leading to decreased functionality of the HexA (αβ) enzyme due to impairment of the α-subunit [40-42]. In contrast, SD is due to a mutation in the HEXB gene consequently effecting the enzymatic function of both the HexA (αβ) and the HexB (ββ) enzymes due to impairment of the β-subunit [42-44]. These diseases are characterized by lysosomal storage of GM2

ganglioside in neurons and glial cells within the central nervous system (CNS), where gangliosides are predominantly synthesized, classifying these as neurodegenerative diseases [32, 42, 43, 45]. Both diseases have a variety of forms depending on the specific mutations involved and the remaining residual enzymatic activity. SD consists of infantile, juvenile, and late-onset forms. These diseases can present with a multiplicity of symptoms including cognitive and speech impairments, ataxia, and lower motor neuron disease [40, 43]. Late-onset SD has been reported in an array of clinical case reports as presenting as a motor neuron disease such as spinal muscular atrophy and amyotrophic lateral sclerosis [41, 43, 45-50]. Lower motor neuron disease is prevalent in 42% of late onset SD cases and has been described as one of the main clinical features [41]. Diffuse neuronal degeneration and enlarged neurons within the anterior horn of the spinal cord, which closely resembles the pathophysiology of lower motor neuron disease, has been repeatedly reported in late-onset SD case studies [43, 45, 51, 52]. Therefore, the effectiveness of future therapeutics will depend heavily on the ability to reduce neuronal loss, which is what makes SD symptoms irreversible [53]. Through the use of $hexb^{-/-}$ mice, a well characterized model of SD that maintains the progressive neurodegeneration seen in SD and TSD, mechanisms which result in this neuronal loss can be evaluated.

Animal models play a key role that allow for advancements in the understanding of the development and progression of fatal, genetic diseases such as SD and TSD. Huang and colleagues created mouse models for both diseases but surprisingly $hexa^{-/-}$ mice, which should have exhibited the clinical manifestations of TSD, failed to show this

alternate phenotype [44] These mice were indistinguishable from wildtype mice to >1 year of age. When examined, these mice had minimal accumulation of GM2 ganglioside and membranous cytoplasmic bodies (MCB) in the brain, but this was not significant enough to trigger TSD pathology. In contrast, *hexb*^{-/-} mice, a model for SD disease, have severe accumulations and develop a disease phenotype. By 3 months of age these mice begin to present with severe motor deficits including impaired reflexes, muscle weakness and atrophy, ataxia, and tremors. Symptom onset is closely followed by death within 4 – 6 weeks for a total lifespan of ~4 months [44, 54, 55]. The pathophysiology and phenotypic display seen within these mice closely mimics that of SD and TSD , making this model vital in the examination and exploration of these fatal diseases.

The discordance of disease development and severity between the different mouse models (*hexb*^{-/-} vs *hexa*^{-/-}) was found to be a consequence of partial catabolism of GM2 in *hexb*^{-/-} mice. This pathway utilizes sialidases to convert GM2 to GA2 followed by subsequent degradation of GA2 by HexB [44, 54, 55]. This ulterior route for degrading GM2 therefore eliminates the need for HexA and maintains non-toxic GM2 levels. This pathway is in sharp contrast to the pathway in humans, in which GM2 degradation is almost solely completed by HexA. Therefore, any disruption in the enzymatic capacity of HexA in humans results in extensive storage of gangliosides and consequently the establishment of TSD [56].

Mechanisms of Disease

A common feature of many LSDs is severe neurodegeneration in the CNS, namely the brain and the spinal cord. The spinal cord is a highly complex circuit that controls our ability to breathe, move, and perceive external stimuli. The spinal cord can be divided into four regions: cervical, thoracic, lumbar, and sacral. Each region of the spinal cord can then be roughly divided into an additional three segments: posterior (dorsal), intermediate, and anterior (ventral), which have been identified to each have their own distinct functions (Figure 2) [57]. The posterior horn is ultimately responsible for mediating exteroceptive sensory processing, while the anterior horn is imperative for muscle innervation and motor execution. The intermediate area of the spinal cord has a vital role in which it is involved in the integration of ascending (sensory) and descending (motor) information to fine tune an informational output. [57-59]. Within these regions are highly heterogeneous populations of neurons that allow for this sophisticated sensorimotor processing [57] [60]. Recent experiments have identified cell type and circuit organizations within the spinal cord that result in populations of neurons playing relatively independent roles. The identification of these neuron types was done using a variety of features including morphology, physiology, molecular markers, behaviour, location, and connectivity [57, 60-62]. Therefore, due to their isolated roles, perturbations of specific populations does not result in a breakdown of motor control entirely, but rather the development of a distinct functional phenotype [57]. The specificity of neuron population function correlates with the clinical features exhibited by late-onset SD patients. Clinical

reports have reported wide-spread denervation that closely resembles the degeneration seen with lower motor neuron diseases, which connects functionally to symptomatic phenotypes such as muscle weakness and severe tremors [41, 51] [47-49, 63, 64]. The mechanisms of how the accumulation of GM2 results in the degeneration and death of motor neurons to produce symptoms are still being explored. Several hypotheses regarding the mechanisms behind the neurodegeneration seen in SD and TSD have been proposed, including lysosomal rupture, neuronal morphological changes, neuroinflammation, autophagy and mitochondria storage, and Ca^{2+} homeostasis [65-70]. Although there is evidence for each of these, the activation of ER stress and the unfolded protein response (UPR) leading to apoptosis of neurons holds significant promise. ER stress has been linked to all the mechanisms proposed above, making it an ideal candidate for examination in these diseases [10].

A

Dorsal

Cervical

Thoracic

Lumbar

Sacral

Ventral

Sensory

Motor

Preganglionic sympathetic

Postganglionic sympathetic

B

Dorsal root

Dorsal column

Dorsal root ganglion

Vascular smooth muscle, sweat glands, and arrector pili muscles in skin

Dorsal ramus

ramus

Ventral root

Gray ramus communicans

Sympathetic chain ganglion

White ramus communicans

Splanchnic nerve

Figure 2. A diagrammatic representation of the regions of the spinal cord, as well as the intraregional locations of specific neuronal populations. (**A**) A schematic depiction of an entire human spinal cord, with transverse sections from each of the four distinct regions: cervical, thoracic, lumbar, and sacral. Note that the white matter increases in an absolute amount, moving from caudal to rostral (Image retrieved from Netters Atlas of Neuroscience, 2nd edition). (**B**) A representation of a transverse section of the spinal cord, and the neuronal populations present. Neurons of the dorsal horn receive sensory information while the ventral horn contains motor neurons that innervate muscles. The intermediate/lateral region is responsible for integration of ascending (sensory) and descending (motor) information to fine tune an informational output (Image retrieved from Waxman's Clinical Neuroanatomy, 26th edition).

(i) Psychosine Hypothesis

This hypothesis suggests that defective enzymes in the degradative pathway for galactocerebrosides leads to an accumulation of psychosine, a substrate product [71]. Due to the defective enzymatic activity, psychosine accumulates at toxic levels resulting from a failed cleavage of galactose [71]. Neuronal death, a consequence from rapid loss of oligodendrocytes, can be the result of the storage of this cytotoxic substrate product and therefore could account for the neurodegeneration associated with LSDs [71].

(ii) Morphological Changes and Synaptic Dysfunction

Neurons in LSDs can undergo several morphological changes due to the accumulation of substrates. One change that is unique to storage diseases is the formation of meganeurites which is the formation of new dendritic neurites that are synapse-covered at the axon hillock [72]. Meganeurites contain storage material that correlates with the defective lysosomal enzyme and have been associated with an increased expression of GM2 ganglioside. In the case of GM2 gangliosides the formation of meganeurties seems to be in a cell autonomous manner in that only affected neurons develop meganeurites [65]. Another morphological change, that is not disease specific, is the formation of axonal spheroids, which is enlargement to the distal axon terminal [65]. These can be detrimental because they can interfere with the timing and efficiency of action potential propagation which can have effects on neuronal activity and brain function [65]. The morphological changes occurring in neurons that impact action potential propagation and signalling have a detrimental effect on brain function and

19

neuron functionality which can result in the disease development seen with LSDs. Many

aspects of these changes such as alterations in synaptic neurotransmission, changes in the

generation and recycling of synaptic vesicles, defects in synaptic spines, variations in

synaptic proteins, axonopathy and reduced dendritic spines have all been reported in Tay

Sachs disease as well as other LSDs. Other studies have also shown irregular distribution

of synaptic proteins, disorganized microtubule networks, reduced postsynaptic densities,

fewer synaptic vesicles, and alterations in frequency and amplitude of postsynaptic

potentials [38, 73, 74].

(iii) Inflammation/Gliosis

Another hypothesized mechanism resulting in neuronal death is inflammatory

response activation in the CNS. In LSDs but more specifically GM2 gangliosides, microglia

sense the preliminary damage resulting from glycolipid accumulation, become activated,

and begin removing damaged or dying neurons [70]. These activated microglia start

producing the proinflammatory cytokine TNF-alpha along with other cytokines, which can

have neurotoxic effects that can exacerbate the stress on neurons with glycolipid build up

[70]. In a study by Abo-ouf et al, a *hexb$^{-/-}$ Tnfα$^{-/-}$*double knockout mouse model was

developed to further explore the implications of TNFα on the development and

progression of SD [69]. It was found that the reduction of TNFα resulted in decreased

activation of astrogliosis and lower levels of neuronal apoptosis which ultimately

translated into improvements in neurological functioning, with no change in microgliosis

[69]. This study was also able to highlight that TNFα derived from both the CNS and bone-

marrow contributed to the pathogenesis of SD with CNS derived TNFα playing a more significant role.

The whole process of microgliosis and subsequent TNFα production/secretion is worsened by the dysfunctional enzymatic activity in the microglia resulting in the inability to degrade the endocytosed glycolipids [70]. It has been noted that prolonged inflammation can result in mass neuronal apoptosis and damage to neighbouring neurons [67]. An interesting observation surrounding this hypothesis in a study of Sandhoff mice was that these activated microglia are present in areas of the central nervous system that later show vast amounts of neuron death. This suggests that the inflammation is contributing to the neurodegeneration and disease progression rather than acting in response to the damage [70].

(iv) Autophagy and Mitochondrial Dysregulation

Lysosomes have many vital roles within cells that help maintain cellular homeostasis. One key pathway is the autophagy-lysosome pathway (ALP), in which unwanted cellular constituents are degraded and recycled [75]. Lysosomal storage impairs this process through pH changes and lysosomal destabilization, which results in an accumulation of polyubiquitinated proteins and dysfunctional mitochondria [65]. Cellular components that were targeted for degradation but have failed to undergo the process begin getting stored within the lysosome. The accumulation of a vast collection of other cellular substrates can continue to worsen the effect of the accumulation, forcing the lysosome to undergo severe or even detrimental stress. Loss of lysosomal regulation

produces an extensive cascade of issues within affected neurons and can thereby advance the neurodegeneration seen in most LSDs [65]. mTOR is a key player in the activation of autophagy, therefore if it cannot be activated, autophagy is unable to proceed. In Gaucher and Fabry disease, two types of LSDs, mTOR activity has been shown to be reduced and it is suggested that the accumulation of these metabolic substrates that occurs within lysosomes results in autophagolysosome formation which negatively effects mTOR activation [75]. Another potential mechanism proposed was that substrate accumulation results in impaired lysosomal functioning which impacts the lysosome's ability to fuse with autophagosomes and therefore inhibits the autophagic flux within the cell [36]. This ultimately leads to an accumulation of autophagosomes, toxic proteins, and aberrant mitochondria which can trigger ER stress, inflammatory response, and in chronic cases, apoptosis [36].

Dysfunctional mitochondria storage within the cell can also play a significant role in disease progression. The accumulation of these mitochondria may accentuate a cell's vulnerability to stimuli that can induce apoptosis [76, 77]. Mitochondria are also main production centres for reactive oxygen species (ROS), therefore if mitophagy is impaired and these faulty mitochondria cannot be degraded, an overproduction of ROS occurs. This triggers an inflammatory response which can lead to neuronal apoptosis as seen in LSDs [65]. Another potential aspect is that functional lysosomes are essential for autophagy ensuring that autophagolysosomes can produce metabolites from macromolecules, which move to the mitochondria and provide ATP for cell survival [75]. When lysosomes

begin to undergo dysfunction due to mitochondria accumulation, this process is disrupted which can have several downstream consequences, but the exact mechanisms of these processes remain to be fully understood. Overall, lysosomes and mitochondria are essential for several processes including autophagy, mitochondrial metabolism, and energy balance, all of which help to maintain cell homeostasis and survival [75].

Mitochondria are also closely linked with the ER through contact sites known as mitochondrial associated ER-membranes (MAMs). These reversible tethers between the two organelles concurrently influence cellular processes such as Ca^{2+} signaling/homeostasis, autophagy, the production and transportation of lipids and their intermediates, energy metabolism, the structural features of the mitochondria, and apoptosis [78]. Given the vitality of the functions regulated by MAMs it is understandable that any alterations in their lipid concentration or topology can drastically impact their abilities to regulate ER and mitochondrial processes and result in cell death and associated pathologies. Annunziata et al suggest that lipids that accumulate in the plasma membrane and lysosomes can undergo a redistribution to membranes of other organelles. This change in the localization of this lipid build-up can then impact the lipid composition of MCS, disrupting organelle crosstalk and their roles affecting the control of global cellular homeostasis [78]. A specific example of this is in GM1 gangliosidoses where GM1 undergoes a redistribution to the membrane of the ER, increasing the number of contact sites between the ER and mitochondria, and facilitating a persistent influx of Ca^{2+} into the mitochondria [78]. This can lead to ER Ca^{2+} depletion and mitochondrial Ca^{2+} overload,

both of which can cause chronic stress within the cell and lead to apoptosis and the phenotypic outcome characteristic of this disease.

(v) Lysosomal Rupture and Dysfunction

Lysosomes play such an essential role in cellular homeostasis and survival and therefore maintaining their integrity and function is imperative. In 1955, Christian de Duve and colleagues discovered the lysosome and shortly following this they proposed the "suicide bag hypothesis" which suggested that cellular death was a result of lysosomal hydrolases being released after membrane destabilization [79, 80]. Today, lysosomes are known to be implicated in a pathway of regulated cell death called lysosome-dependent cell death (LDCD). Lysosomal membrane permeabilization (LMP) is the hallmark characteristic of this pathway and is an indicator of lysosomal dysfunction [80]. It is still controversial as to whether lysosomal enlargement, which can be caused by the accumulation of undegraded materials, is required for LMP but it has been suggested that enlarged lysosomes are more susceptible [81]. When lysosomes become stressed, they swell and therefore can undergo LMP. In severe cases, where a large number of lysosomes are affected, lysosomes cannot be repaired through stress response mechanisms and they release hydrolases which results in mitochondrial damage and can trigger apoptosis [80]. A large number of stimuli have been implicated in LMP including reactive oxygen species, proteases, and accumulated sphingosine [82]. Lysosomal death is a complex process in which it can be the cause of cell death or a result from other contributing stressors within the cell and its mechanism is still not fully understood. It seems to be intricately connected

with other mechanisms and could be a crucial component in the puzzle that is the mechanism of LSDs.

(vii) Ca^{2+} Dysregulation

Ca^{2+} homeostasis disruption can impact a variety of cellular functions across many different cell types. For example, when microglia within the central nervous system are exposed to elevated intracellular Ca^{2+} levels, inflammasome activity can be activated as well as the release of cytokines that trigger an inflammatory response [67]. Another example is the sensitivity of neurons to Ca^{2+} levels. High Ca^{2+} concentrations are toxic to neurons and can lead to unsynchronized synapses and unregulated firing which can result in an increase in Ca^{2+} in neighbouring glia, worsening the response [67].

Altered Ca^{2+} concentrations can also affect the functionality of specific organelles including the ER and lysosomes [83, 84]. Variations in ER Ca^{2+} stores can induce ER stress which, in cases of chronic and prolonged stress, can trigger apoptosis through the activation of the UPR signaling cascades [67]. Within lysosomes, Ca^{2+} plays a significant role in signal transduction, exocytosis, nutrient sensing, and vesicular trafficking, all of which maintain cellular functionality [85]. Therefore, the disruption or dysregulation of lysosomal Ca^{2+} can lead to a vast array of consequences. Both ER and lysosomal Ca^{2+} influence cellular homeostasis and therefore when Ca^{2+} is disrupted, essential cellular processes are affected and can result in cell death [36].

The ER is the largest store of Ca^{2+} within the cell and maintains a high Ca^{2+} concentration [86]. This creates a Ca^{2+} gradient between the ER and the cytosol, with

lower Ca^{2+} concentrations within the cytosol. Ca^{2+} homeostasis within the ER is a tightly regulated process which is controlled by the concurrent actions of Ca^{2+} pumps, channels, and binding proteins. To begin, uptake of Ca^{2+} from the cytosol into the ER is primarily fulfilled by sarco/endoplasmic reticulum Ca^{2+} ATPase (SERCA) pumps which utilize ATP to drive Ca^{2+} across the ER membrane [87]. In contrast, Ca^{2+} release from the ER into the cytosol is mediated by two types of channels, IP3R and RYR, which are localized to the ER membrane. In cases when the ER Ca^{2+} store needs to be replenished, a process known as store operated Ca^{2+} entry (SOCE) or capacitive Ca^{2+} entry is initiated. This process utilizes an ER sensor, stromal-interacting molecule (STIM), which becomes activated when Ca^{2+} dissociates due to depleted levels [87]. Activation of STIM leads to an influx of Ca^{2+} from the extracellular environment into the cytosol where SERCA can then directly pump Ca^{2+} into the lumen of the ER. Overall, the ER is constantly working to maintain steady state Ca^{2+} levels to optimize and fulfil its plethora of vital functions such as protein synthesis and folding and maintenance of cellular homeostasis.

Many diseases including cardiovascular disease, diabetes, and neurodegenerative disorders are associated with ER Ca^{2+} dysregulation [85, 86, 88]. This suggests that this perturbation of ER Ca^{2+} stores can significantly contribute to the development and progression of a vast array of diseases. Of particular interest, ER dysfunction as a direct consequence of impaired Ca^{2+} homeostasis has been frequently reported as being intricately involved in the progression of a wide range of LSDs [89]. Pelled and colleges conducted a study in which they explored the implications of GM2 accumulation in

neuronal tissue collected from *hexb*$^{-/-}$ mice, a model for SD [66]. They were able to identify

a causal relationship between the endogenous accumulation of GM2 and rates of Ca^{2+}

uptake via SERCA. In microsomes collected from *hexb*$^{-/-}$ mice brains Ca^{2+} uptake via SERCA

into the ER was severely diminished as a result of decreased V_{max} of SERCA and not due to

variation in the overall expression of SERCA [66]. The authors suggest that the primary

accumulation of GM2 is directly responsible for this perturbation of SERCA. This reduction

in the uptake of Ca^{2+} into the ER was abolished when mice were treated with N-

Butyldeoxynojirimycin, which inhibits the synthesis of glycolipids and reduces the amount

of GM2 accumulation occurring [66]. The depleted internal Ca^{2+} stores within the ER,

which can functionally disrupt the ER and lead to the induction of ER stress and UPR

activation, provides a direct association between initial accumulation within the

lysosomes and chronic ER stress induction and subsequent neurodegeneration.

Similar findings were reported in a study released by the D'azzo group in which

they determined that through GM1 accumulation in *β-galactosidase* knockout mice, ER

Ca^{2+} was disrupted and there was buildup of gangliosides within the ER [90].

Neurospheres cultured from *β-gal*$^{-/-}$ mice, and their wildtype counterparts were treated

with thapsigargin, an inhibitor of the ER Ca^{2+} pump, resulting in instantaneous Ca^{2+}

release. This revealed that wildtype neurospheres released their Ca^{2+} stores while *β-gal*$^{-/-}$

neurospheres were not affected by the treatment suggesting that their stores were

already depleted [90]. Therefore, these results demonstrate a connection between GM1

accumulation and ER Ca^{2+} dysregulation.

Additionally, Ginzberg and Futerman reported defective ER Ca^{2+} regulation in Niemann-Pick A disease (NPD-A) [91]. The authors utilized microsomes prepared from the cerebellum and cortex of endpoint $ASM^{-/-}$ mice, a model of NPD-A. This revealed that Ca^{2+} homeostasis was not altered in the microsomes from the cortex but in contrast cerebellar microsomes showed ~60% reduction in Ca^{2+} uptake via SERCA [91]. Moreover, cerebellar microsomes also demonstrated reduced expression of SERCA and IP3R while cortex microsomes did not show similar trends. These alterations were further analyzed developmentally, and it was noted that by 2 months of age $ASM^{-/-}$ mice, who showed minimal phenotypic symptoms, demonstrated moderate reductions in IP3R expression [91]. Alterations in SERCA expression was not seen until 4 months of age, confirming that IP3R reduction precedes the reduction of SERCA. The degree of decreased expression and progressive dysregulation of Ca^{2+} within the cerebellum parallels the onset of phenotypic symptoms. This once again demonstrates the consequential effects of dysfunctional ER Ca^{2+} in LSDs.

Overall, these findings taken together indicate that across a broad range of LSDs there has been evidence of ER Ca^{2+} dysfunction which prompts the hypothesis that ER Ca^{2+} dysregulation results in ER stress and subsequently cell death. The direct mechanisms connecting primary accumulation to the resulting cell death and neurodegeneration seen in most LSDs has yet to be elucidated but these findings provide a general structure for a potential mechanism. An outstanding question is what leads to this disruption in ER Ca^{2+}. It has been suggested, specifically within GM2 gangliosidoses, that the substrate interacts

with SERCA to impair Ca^{2+} reuptake [66]. What has yet to be considered is the possibility

of a malfunction in the connection between the ER and lysosomes which could lead to

disruption in global Ca^{2+} homeostasis including depletion of ER Ca^{2+} stores and lysosomal

Ca^{2+} stores and alteration in cytosolic Ca^{2+}.

In more recent literature, lysosomes, known formerly as the recycling center of

the cell, have begun to emerge as alternate cellular Ca^{2+} stores that play important roles

in Ca^{2+} homeostasis [92]. Similar to the ER, lysosomes are equipped with channels and

transporters, such as TRPMLs and two-pore channels, to regulate Ca^{2+} concentrations but

the lysosomal Ca^{2+} pathway is still a controversial topic within the field [85]. There are two

main proposed mechanisms by which lysosomal Ca^{2+} is refilled. The first proposes that

Ca^{2+} stores are refilled via a pH-dependent process based on the observation that when

pH was altered either through v-ATPase inhibitors or by creating a more basic pH, there

was a decrease in lysosomal Ca^{2+} [93-95]. The second mechanism describes the ER as

being a major contributor to the refilling of lysosomal Ca^{2+} stores [96]. In a study by Garrity

et al, it was demonstrated that demolishing pH gradient did not eliminate refilling, but the

depletion of ER stores did abolish refilling [96]. Additionally, it was established that

inhibiting IP3Rs caused lysosomal dysfunction and a phenotype that resembles LSDs while

RyR inhibition did not have a similar impact, indicating the importance of IP3Rs for

refilling. An independent study by Ronco and colleagues found evidence in support of this

mechanism in that lysosomal Ca^{2+} refilling was prevented if SERCA activity was inhibited

[97]. Although both hypotheses provide potential mechanisms, the neighbouring cellular

localization of the ER with lysosomes and the notion that they form MCSs supports the critical role of the ER in refilling lysosomal Ca^{2+} stores suggested by Garrity et al [8, 9, 23, 96]. These studies provide a platform to better study the mechanisms of lysosomal Ca^{2+} refilling and its potential implications in disease.

The dysregulation of lysosomal Ca^{2+} has been associated with a variety of neurodegenerative diseases including Alzheimer's disease, Parkinson's disease, and ALS but of significance it has also been observed in LSDs [93, 98-100]. In Niemann-Pick Disease type C (NPC), lysosomal Ca^{2+} stores were depleted potentially due to inhibited Ca^{2+} reuptake or sphingosine accumulation which disrupted refilling [93]. Abnormal Ca^{2+} regulation has also been reported in Mucolipidosis Type IV, where mucolipin TRP channel 1 (TRPML-1), a lysosomal ion channel, is dysfunctional leading to defects in Ca^{2+} release and results in enlarged lysosomes and severe neurodegeneration [101]. TRPML-1 mediated Ca^{2+} release has also been reported as impaired in NPC, revealing that different aspects of lysosomal Ca^{2+} can be dysfunctional, including refilling, concentration, and release, and can lead to a variety of pathophysiological outcomes [36, 101]. Current findings indicate that ER Ca^{2+} levels are aberrantly handled in multiple LSDs and that the ER and its Ca^{2+} store have large implications in lysosomal Ca^{2+} homeostasis. From this a reasonable conjecture would be that not only is there lysosomal Ca^{2+} dysfunction found across a wide variety of LSDs which also have abnormal ER Ca^{2+} regulation, but that there is a tight interconnection between these two dysfunctional mechanisms that results in severe neurodegeneration.

(ix) ER Stress and the UPR

The ER has been the feature of a several studies which attempt to highlight a potential mechanistic pathway within various LSDs. Wei and colleagues examined common features across neurodegenerative and non-neurodegenerative LSDs that resulted in apoptosis. The authors evaluated a multitude of LSDs including Gaucher type 1 and 2, Tay Sachs, GM1, Niemann-Pick C type 2, and neuronal ceroid lipofuscinoses using cultured fibroblasts from LSD patients [102]. They were able to identify that ER stress activation and oxidative stress were common mediators for cellular death across both categories of LSDs. Results showed elevated levels of activated ATF6, GRP78, GRP94, and phosphorylated eIF2α, all of which are indicative of ER stress and the activation of the UPR [102]. In a similar study, Tessitore et al isolated primary neurons from a GM1 mouse model to assess the consequences of substrate accumulation. Initially, the authors noted that in spinal cord neurons of *β-galactosidase* knockout (*β-gal*$^{-/-}$) mice there were massive amounts of GM1 accumulation, and the ER was being compressed amongst multiple enlarged lysosomes [90]. This morphological disruption can independently have implications on ER function, but the authors also reported the initiation of ER stress and activation of the UPR in this disease. Cultured neurospheres from *β-gal*$^{-/-}$ mice demonstrated transcriptional upregulation of GRP78, CHOP, and XBP1 which not only indicate ER stress, but CHOP expression suggests chronic stress. To complement their in vitro work, real-time PCR mRNA levels were evaluated in spinal neurons of *β-gal*$^{-/-}$ mice. This confirmed that GM1 accumulation results in chronic ER stress and UPR activation,

which was demonstrated through increased levels of CHOP, GRP78, and cleaved ATF6 [90]. Despite the focus of this paper being GM1 gangliosidosis, this research provides strong evidence for ER stress involvement when ganglioside accumulation occurs within neurons. Overall, current evidence highlights the potential role of ER stress, due to ganglioside accumulation, in LSDs. More importantly it provides a possible link between lysosomal dysfunction and the severe neuronal loss seen in neurodegenerative LSDs, but further research is required to fully understand the role of ER stress in each LSD specifically.

ER stress and the UPR have clearly been implicated in a variety of LSDs, but we believe that ER stress provides only a partial link from lysosomal dysfunction to neuronal cell death seen in GM2 gangliosides and other neurodegenerative LSDs. Another possibility is that ER stress and the UPR occurs concurrently with other cellular dysfunctions such as Ca^{2+} dysregulation. ER stress is a steppingstone along the path connecting the characteristic accumulation and the development of neuronal apoptosis, which ultimately results in functionally correlated clinical phenotypes. The mechanism by which lysosomal accumulation and dysfunction results in ER stress initiation remains to be elucidated. A potential pathway is that lipid accumulation leads to a disruption in Ca^{2+} homeostasis not only within the ER but also within the lysosome itself which can activate ER stress. Therefore, there is an interdependency between cellular functions as well as organelles to maintain homeostasis and the resultant neurodegeneration seen in LSDs may be due to concurrent cellular dysfunctions.

The survival and correct functioning of cells requires tight maintenance of cellular homeostasis which is controlled by a multitude of organelles and processes working in concert. If any part of this system is impaired, cellular homeostasis is disrupted which results in acute cellular dysfunction and consequently cell death [103]. After the initial insult of lysosomal dysfunction and substrate accumulation, cellular dysfunction begins with changes in Ca^{2+} homeostasis, mitochondrial functioning, activation of inflammation, and initiation of ER stress. As discussed earlier, chronic ER stress activation has been a common finding reported in several categories of LSDs and acute activation of this response can lead to apoptosis [66, 90, 102, 104, 105]. ER stress and the UPR begin as a pro-survival mechanism employed by the cell, but if the stress cannot be alleviated apoptosis can ensue. The 3 arms of the UPR, PERK, IRE1, and ATF6 do not directly cause apoptosis but rather through their signal cascades activate a series of downstream pro-apoptotic factors [11, 18]. There is a multiplicity of pathways within the UPR that can trigger apoptotic pathways including downstream signaling from IRE1, activation of CHOP and initiation of a caspase signaling cascade. To begin, IRE1 plays a dual role in ER stress and the UPR such that in addition to its role in cell survival and protection, IRE1 can evoke the stimulation of tumor necrosis factor receptor associated factor 2 (TRAF2) which further activates apoptosis signal-regulating kinase 1 (ASK1). This initiates a signaling cascade which induces downstream kinases Jun-N-terminal kinase (JNK) and p38 MAPK to become activated. They further act on their own signaling pathways with JNK phosphorylating Bcl-2 and Bim, inhibiting and activating the factors respectively, and p38

MAPK activates CHOP through phosphorylation [106]. Secondly, all three arms of the UPR can induce the activation of CHOP which acts on its own collection of downstream target genes. Some targets of CHOP involved in apoptosis include GADD34, endoplasmic reticulum oxidoreductase-1 (Ero1-alpha), Bcl-2, and Bim [12]. GADD34, upon activation by CHOP, works to dephosphorylate eIF2-alpha, reversing the inhibition on global protein translation aiding in the accumulation of unfolded proteins as well as allowing for the translation of pro-apoptotic factors. Ero1-alpha, which under physiological conditions catalyzes disulfide bond formations but when targeted by CHOP can lead to hyper-oxidation of the ER and can also stimulate IP3R leading to substantial Ca^{2+} transport to the mitochondria from the ER, both of which can promote cell death [106, 107]. It has also been reported that CHOP can directly inhibit transcription of anti-apoptotic factor Bcl-2 while also inducing the expression of Bim, a pro-apoptotic factor, ultimately inducing apoptosis [12]. Lastly, apoptosis can be triggered through the activation of caspase-12, whose activation is ER stress specific [108]. Caspase-12 becomes activated by calpains and goes on to cleave procaspase-9 which then stimulates caspase-3, an executioner caspase [18, 109]. Caspase-12 serves as a marker for apoptosis in murine models but due to humans lacking a functional homologue, its role in human cells remains to be determined [108]. The proapoptotic factor poly (ADP-ribose) polymerase (PARP) has also been shown to be cleaved and activated in a variety of neurodegenerative LSDs [102]. This highlights the possibility that other caspases, such as caspase 7 which is responsible for the cleavage of PARP, may be intimately involved in the demise of cells mediated by ER stress [110].

Caspase 7 has also been suggested as a secondary pathway of activation for caspase 12 during ER stress induced apoptosis [18, 111].

Mechanisms of ER-stress induced apoptosis have been reported across numerous neurodegenerative diseases including Alzheimer's disease, Parkinson's disease, and amyotrophic lateral sclerosis, which have been reported to manifest in similar phenotypes as described with neurodegenerative LSDs, indicating there may be similarities in mechanisms of disease. The linking feature between vastly different activation pathways of apoptosis is chronic ER stress, suggesting that ER dysfunction may play a large role in neurodegenerative disease pathogenesis.

In LSDs, lysosomal catabolism is severely inhibited which can further affect a multiplicity of other cellular functions including Ca^{2+} homeostasis, autophagy, and proper functioning of the ER and mitochondria, which ultimately leads to apoptosis of cells leading to the phenotypic presentation of the disease. The question that remains is how does the primary accumulation and lysosomal dysfunction result in this mass cellular death, what processes occur in between to initiate the apoptotic events? Research by Tessitore and colleagues demonstrated that in a mouse model of GM1 gangliosidoses, the diseased samples had more TUNEL positive cells scattered throughout the spinal cord in comparison to the wildtype [90]. Also, mRNA levels of apoptotic associated factors such as CHOP, activated JNK2, and activated caspase-12 were elevated in spinal neurons of the knockout mice compared to wildtype. These changes were noted to be time dependent, with higher levels correlating with more severe symptoms that occur at later stages of the

disease. The authors also noted that ER stress and acute activation of the UPR was the cause of this neuronal death, which was demonstrated by the activation caspase 12, which is thought to be ER stress specific [90]. Caspase activation has also been reported in LSDs. Specifically, in MPS II patient derived TD35 neuronal cultures, levels of caspase 3 and 7, which are both executioner caspases for apoptosis, were significantly increased in comparison to controls [112].

A separate study by Sano et al, suggests a mechanism of Ca^{2+}-mediated apoptosis in which the accumulation of GM1, in specific fractions of mitochondria-associated ER membranes, alters Ca^{2+} homeostasis and activates both ER stress mediated, and mitochondria evoked neuronal apoptosis [113]. By focusing on a common manifestation seen in many LSDs, such as mass apoptosis and neurodegeneration, common mechanisms of activation may arise providing an opportunity for broad range therapeutics. This would allow for treatment across many diseases that are a part of such a heterogeneous group of disorders, that thus far have very limited treatment options due to their diverse and complex nature. Although the initial insult is known and several steps in the intervening pathway have been described, what ultimately connects lysosomal dysregulation to the activation of ER stress and apoptosis remains to be elucidated. Several proposed hypotheses as to what occurs within these cells during these diseases have been discussed but as mentioned earlier, a likely possibility is that Ca^{2+} dysregulation between lysosomes and the ER triggers a dysfunctional cycle which leads to decreased luminal ER Ca^{2+},

36

decreased lysosomal Ca^{2+}, and increased cytosolic Ca^{2+}, all of which can lead to acute ER

stress and the initiation of apoptotic signaling cascades.

Available Therapies and Therapeutics to Treat LSDs

(i) Substrate Reduction Therapy (SRT)

The concept behind this therapeutic technique is to prevent the accumulation of

substrates through the inhibition of specific substrate's biogenesis. The final goal is to

strike a balance between the dysfunctional enzymes ability to catabolize the substrate

and the rate at which the substrate is being produced [32]. A benefit of this treatment is

that it possesses the ability to cross the blood-brain barrier and can be given orally unlike

many other available treatments that are incapable of crossing the blood-brain barrier

[114]. Miglustat, used for the treatment of Type 1 Gaucher disease, is one example of this

type of therapy [115-117]. Miglustat is an imino sugar drug that inhibits disaccharides in

the gastrointestinal tract which helps reduce the burden of substrate accumulation [32,

115, 116]. It has some ability to cross the blood-brain barrier unlike other SRT treatments

such as eliglustat but can have some adverse side effects [32, 115, 116].

(ii) Enzyme Replacement Therapy (ERT)

Currently, enzyme replacement therapy is the most common therapeutic

approach being used to treat LSDs [118]. Unlike substrate reduction therapy, enzyme

replacement is one of the many therapies that is unable to cross the blood-brain barrier

and therefore is incapable of reaching the central nervous system leaving neurological symptoms untreated [119]. Due to the fact that the molecular signal for the specific enzyme to be taken up into the lysosome is known, a recombinant enzyme is then able to be administered intravenously to patients who are naturally lacking the enzyme[119]. In the case of Type 1 Gaucher disease, which was the first LSD that ERT was available for, Cerezyme is used for treatment [120]. It is a recombinant analogue of the deficient enzyme β-glucocerebrosidase that has been modified to expose mannose residues so that it can be taken up by the mannose receptors of macrophages and not the mannose-6-phosphate receptors [120]. This treatment has shown much success in the reduction of severity and management of most symptoms associated with Type 1 Gaucher disease but is not advisable for the acute neuronopathic form of Gaucher disease [120].

(iii) Small Molecule Chaperone Therapy

Small molecule chaperone therapy has been experimented with as a treatment for LSDs. This technique uses an active site inhibitor that binds to the active site of an enzyme resulting in the site becoming more stable and remaining stabilized even after the inhibitor has dissociated [32]. These small molecules may also have a secondary function as site specific chaperones in which case they would be able to assist in the folding of mutant proteins, increasing their ability to escape from the proteases [119]. A new generation of chaperones is being developed to help overcome limitations of active-site inhibitors. These new chaperones are allosteric enhancers that induce a conformational change that either prolongs the half-life of the enzyme or increases enzymatic activity

[32]. An example of this is migalastat, a therapeutic for Fabry disease. Migalastat is an imino sugar drug that interacts with the α-galactosidase A enzyme to stabilize it, facilitate its trafficking from the ER to the lysosome, and increase its lysosomal enzymatic activity [121]. Overall, this therapeutic technique aims to rescue enzyme activity and has shown the potential to treat neurological symptoms by reaching the central nervous system [114]. However, these small molecule chaperones are mutation specific and therefore disease specific meaning individual patients would need to be carefully assessed to ensure suitability for this treatment [32].

(iv) Bone Marrow Transplant (BMT)

Bone marrow transplants are a procedure in which a patient receives donor macrophages and microglia which, through continuous bone marrow turnover, will replace the deficient enzyme activity with normal enzymatic activity [122]. In a study by Wada et al, this treatment demonstrated success in SD mice. After treatment, mice had an increased lifespan and improvements in the severity of neurological symptoms [70]. Also, in SD mice that had been treated with a BMT, a lower density of activated microglia in the central nervous system was noted [70]. The reduction of activated microglia helped to reduce the inflammatory response occurring in the central nervous system of these diseased mice [70].

(v) Anti-Inflammatories

Similar to BMT, anti-inflammatories have been shown to increase the lifespan of mice with SD [123]. When nonsteroidal anti-inflammatory drugs (NSAIDs) were used with antioxidants to treat the diseased mice, survival rate was improved in comparison to untreated diseased mice. Surprisingly, when NSAIDS were combined with substrate reduction therapy, survival rate was further increased by about 66% [123]. This treatment has also shown success in other neurodegenerative diseases such as Alzheimer's and Parkinson's disease, with NSAIDS reversing microglia response [124].

(vi) Gene Therapy

Through the delivery of genetic material using a viral vector, the goal is to compensate for a dysfunctional enzyme within the body and restore enzymatic activity [125-127]. The vector can be given through an IV or through injection. An early vector that was used was a non-integrating adenovirus which has the capacity to carry a large genetic load and has a wide tropism. Unfortunately, it had a multitude of shortcomings such as being highly immunogenic and having a short transgene expression period [125]. A new avenue that is currently being explored is the use of the adeno associated virus (AAV). Although it has a lower genetic load capacity, it still possesses a wide tropism, is far less immunogenic, and has a longer transgene expression period [125]. The promising aspect of the AAV is that it has some stereotypes that have tropism for regions of interest such as the brain which is ideal for LSDs considering the prevalence of neurological symptoms and neurodegeneration [125]. A current example of the success of gene therapy in the

treatment of disease is Zolgensma, an FDA approved AAV based gene therapy used in the treatment of spinal muscular atrophy in pediatric patients. It targets the SMN1 gene to help reduce the progression of the disease in a onetime injection [128]. This type of therapy is particularly ideal for LSDs because cells that have been modified by the gene therapy could secrete functional enzyme that could have the ability to also correct the unmodified cells therefore providing long-term correction [125].

Therapeutics for LSDs is limited not only in the availability but also in terms of efficacy. Future treatments should focus on targeting the characteristic which is seen in many of these disorders and is also responsible for detrimental and irreversible phenotypes, mass neuronal loss. Targeting neurodegeneration could provide a broad-spectrum therapeutic which could potentially be applied to neurodegenerative diseases within LSDs as a whole and possibly other similar neuronal diseases such as spinal muscular atrophy and ALS.

Overall, current research indicates that chronic ER stress is prevalent and activation of the specific arms of the UPR has been shown in a variety of LSDs, including GM2 gangliosidoses [66, 90, 102, 104, 105]. We believe that this mechanism provides a clear link between the characteristic accumulation and the development of neuronal apoptosis, which ultimately results in functionally correlated clinical phenotypes. Therefore, we wanted to explore if ER stress is present within the spinal cord of $hexb^{-/-}$ mice, if there are interregional differences, intraregional patterns of activation, and if this stress results in death of specific types of neurons. To elucidate what is occurring at the cellular level we

also chose to specifically focus on histological outcomes within anterior horn neurons of the spinal cord. Ideally this will show vastly different histology between *hexb*$^{+/+}$ and *hexb*$^{-/-}$ mouse spinal samples which may provide information as to how the neurons are damaged during disease progression. By specifically choosing to focus on ER stress induction within a population of motor neurons, the aim is to elucidate disease mechanisms which may allow for the discovery of future therapeutic targets to treat SD. Primary GM2 accumulation is characteristic of a small collection of LSDs but secondary accumulation is a common finding across many LSDs indicating it could play a larger role in pathogenesis than originally thought [23]. Therefore, the elucidation of mechanistic pathways involved in GM2 gangliosidoses may be widely applicable to other LSDs and disorders presenting with secondary accumulation.

HYPOTHESIS

Spinal cord neurons of Sandhoff disease mice are exposed to prolonged ER stress, activating the UPR, which results in apoptosis and neurodegeneration.

OBJECTIVES

1. To analyze the expression of ER stress markers including CHOP, ATF6, and GRP78 within the different regions of the spinal cord of Sandhoff disease mice using molecular and immunocytochemical techniques.

2. To evaluate the activation of the UPR spatially and developmentally, determine the cell types involved, and note any differences of ER stress response among the 3 spinal regions.

CHAPTER TWO

METHODS/MATERIALS

(i) Mice

Mouse work was conducted under the animal utilization protocol (AUP) in accordance with the Ontario Animals for Research Act specifications and the Animal Research Ethics Board (AREB) guidelines. The Sandhoff model mice (*hexb*$^{-/-}$ on a C57BL/6 background) were generously donated by Dr. R. Gravel (University of Calgary, Canada) and have been previously characterized [55].

(ii) Genotyping

Mice were genotyped using isolated tail genomic DNA as a template for polymerase chain reaction. For Hexb genotyping, 2 forward primers were used. For wild type 5'-GGTTTCTACAAGAGACATCATGGC-3' and knock out 5'-GATATTGCTGAAGAGCTTGGCGGC-3', with a common reverse primer 5'-CAATCGGTGCTTACAGGTTTCATC-3' to generate a 141 bp product for the wild-type allele and a 700 bp product for the knockout allele. The thermocycler program consisted of 35 cycles of 94°C for 30s, 60°C for 30s and 72°C for 45s.

(iii) Immunocytochemistry

hexb$^{+/+}$ and *hexb*$^{-/-}$ mice were harvested at 40, 60, 80, 100, and 120 days. They were perfused with 1x PBS and fixed with 10% buffered formalin. The spinal cord was

harvested, sectioned into the three main regions (cervical, thoracic, and lumbar), and were then embedded in paraffin wax. Four-micrometer thick cross-sections of the spinal cord were cut and mounted on charged slides. Immunocytochemistry was then performed on these samples using Vectastain Elite ABC Universal Plus Kit (Vector Laboratories: PK-8200). Slides were rehydrated, first by washing slides with xylene then by washing them with a 1:1 solution of xylene and ethanol (EtOH) followed by washes in 100% EtOH, 95% EtOH, 70% EtOH, 70% EtOH/1% hydrogen peroxide solution (to quench endogenous peroxidase), 70% EtOH/1% lithium carbonate solution, 70% EtOH, and finally, 50% EtOH. Next, antigen retrieval in a sodium citrate buffer (pH 6) was performed by microwaving the slides at 1 min intervals until boiling and then maintaining a boil for 5 minutes. The slides were then washed with tap water followed by a wash in glycine. The slides were then incubated with bloxall blocking solution for 10 minutes, followed by a 5-minute wash with PBS. Slides were then blocked with 2.5% horse serum for 20 minutes. Primary antibodies for ER stress markers including anti-GRP78 (1:200, Novus Biologicals: NBP1-06277), anti-ATF6 (1:50, Novus Biologicals: NBP1-40256), anti-XBP1 (1:100, Novus Biologicals: NBP1-77681), anti-PDI (1:200, Cell Signaling), anti-CHOP (1:400, Novus Biologicals: NBP2-13172), anti-cleaved PARP (1:400, Novus Biologicals: NB100-56599), anti-PARP (1:400, Cell Signaling; 9542), anti-cleaved caspase 7 (1:400, Cell Signaling: 8438S), anti-NeuN (1:200, Novus Biologicals: NBP1-92693) and normal mouse serum (1:500, Santa Cruz Biotech: sc-2025) were used. Slides were incubated with antibodies overnight at 4ºC. Slides were washed with 1x PBS + 0.05% TWEEN20 for 3x 5 minutes,

prior to application of the secondary antibody. Slides were then incubated with prediluted

biotinylated horse anti-mouse/anti-rabbit IgG secondary antibody for 30 minutes. Slides

were then again washed with 1x PBS + 0.05% TWEEN20 and Vectastain elite ABC reagent

was then add to the slides for 30 minutes and then washed with 1x PBS. Equal amounts

of ABC reagent 1 and 2 were mixed and slides were incubated with the solution until

staining appeared (~5 – 20 minutes) and then were rinsed with tap water. Counterstaining

was then completed by placing slides into 0.1% methylene blue for 1.5 minutes and

removing excess with water. Slides were then washed in EtOH starting at 50% and going

up to 100%, then 1:1 xylene to EtOH, and finally 100% xylene. Lastly, glass slide covers

were mounted using Permount histological mounting medium (Fisher Scientific: SP15-

500). Images were captured at various magnifications via a Nikon Eclipse Ci microscope,

equipped with a Nikon DS-Ri2 camera (Dr. Austin's Lab, St. Josephs Health Care,

Hamilton).

(iv) Western Blot

Mice were anesthetized with 7.5% Avertin and were perfused with PBS through the

left ventricle of the heart. The spinal cord was harvested and divided into the three main

regions (cervical, thoracic, and lumbar), and snap frozen in liquid nitrogen. Lysis buffer

containing EDTA (ThermoFisher; 78440) and protease inhibitor (ThermoFisher; 78440)

that were diluted with RIPA (ThermoFisher; 89900) was added to the samples which were

then sonicated and homogenized. Homogenized samples were then aliquoted and

Laemmeli sample buffer (4x) was added to the lysate before being boiled for 10 minutes

at 100ºC. Samples were then loaded into an 10% SDS-PAGE resolving gel with a 5% stacking gel in equal protein quantity as determined by protein assay. SDS-PAGE was run at 90V for 120 min. Run gels were then transferred at 4ºC for 60 min at 100V onto a nitrocellulose membrane. Membranes were then blocked for 60 min using 5% non-fat powdered milk in tris-buffered saline with Tween-20 (TBST) (10mM Tris-HCl, 150mM NaCl, 0.05% Tween-20) on a rotator at 4ºC. Membranes were then incubated with a primary antibody, anti-GRP78 (Novus Biologicals: NBP1-06277, 1:1000: Anti-Rabbit), anti-ATF6 (Novus Biologicals: NBP1-40256, 1:1000: Anti-Mouse), anti-XBP1 (Novus Biologicals, 1:1000: Anti-Rabbit), anti-IRE1-phos (Novus Biologicals: NB100-2323, 1:1000: Anti-Rabbit), and anti-CHOP (Novus Biologicals: NBP2-13172, 1:1000: Anti-Rabbit) and were left overnight on a rotator at 4ºC. Blots were then washed with 1x TBST for 3x 5min. Next, the correct horseradish peroxidase conjugated secondary antibody was added to the membrane, with a dilution of 1:2000, for 60 minutes at room temperature followed by 3 washes in 1x TBST. Blotted membranes were then incubated with Amersham ECL western blotting detection reagent (Cytiva: RPN2106) for 1 minute before being exposed to Amersham Hyperfilm ECL high performance chemiluminescence film (GE Healthcare: 28906836) for varying lengths of time dependent on the antibody. The X-ray films of blots were scanned and saved as .TIFF files.

(v) Immunofluorescence

Spinal cords from *hexb*$^{-/-}$ and *hexb*$^{+/+}$ mice were harvested at 40, 60, 80, 100, and 120 days and embedded in paraffin as described above. Samples were rehydrated, first

by washing slides with xylene then by washing them with a 1:1 solution of xylene and

ethanol (EtOH) followed by washes in 100% EtOH, 95% EtOH, 70% EtOH, 70% EtOH/1%

lithium carbonate solution, 70% EtOH, and finally, 50% EtOH. Next, antigen retrieval in a

sodium citrate buffer (pH 6) was performed by microwaving the slides at 1 min intervals

until boiling and then maintaining a boil for 5 minutes. The slides were then washed with

tap water followed by a wash in glycine. Following, the slides were then incubated with

bloxall blocking solution for 10 minutes, followed by a 5-minute wash with PBS. Slides

were then blocked with 2.5% horse serum for 20 minutes. Samples where then double

labelled with a combination of anti-GFAP (1:100, Sigma: G9269), and anti-NeuN (1:100,

Novus Biologicals: N.BP1-92693). Slides were incubated with antibodies overnight at 4ºC.

Samples were washed with 1x PBS + 0.05% TWEEN20 for 3x 5 minutes, prior to application

of the secondary antibody. Following, slides were double labeled with appropriate Alexa

Fluor secondaries (Invitrogen, goat anti-rabbit 488: A11037, goat anti-mouse 594:

A11029) and then again washed with 1x PBS + 0.05% TWEEN20. Finally, the slides were

mounted with ProLong Diamond antifade mountant reagent with DAPI (Invitrogen:

P36966). Samples were imaged using Ziess Axiovert 200 scope equipped with an HBO 100

mercury lamp.

(vi) Statistical Software

For data sets with groups of two that needed to be compared, t-tests were used

to test for differences between means at P<0.05. Data sets of three or more groups were

tested for differences between means at P<0.05 using one-way ANOVA. This was followed

by Tukey's post hoc test for all data sets with equal variance and high normality between groups. For sample sets with unequal sample sizes or variance, Kruskal-Wallis test was used for a pairwise comparison. All statistical analyses were performed using GraphPad Prism 9 (V.9.3.0).

CHAPTER THREE

RESULTS

Disease Pathophysiology and ER Stress at 120d

1. **Histological and Morphological Evaluation of the Spinal Cord in *hexb*^{+/+} and *hexb*^{-/-} Mice**

Targeted disruption of the *hexb* gene resulted in a mouse model of SD with a wide range of behavioural, histological, and morphological abnormalities corresponding well to the manifestation of SD and TSD in humans. Histologically, spinal motor neurons, specifically anterior horn neurons (AHNs), show significant differences in their morphology and structural integrity between *hexb*^{+/+} and *hexb*^{-/-} mice. In *hexb*^{+/+} mice, AHNs show a fusiform, conical, or star-like shape with a smooth cell membrane and fine organelle structures, i.e., Nissl bodies within the cytoplasm. The nucleus and nuclear membrane are spherical and smooth (Figure 3 A). In contrast, anterior horn neurons in *hexb*^{-/-} mice at end point (120d) show an engorged and rounded shape due to the significant amount of lipid accumulation within the lysosomes. Their cell membrane is displaced due to swollen lysosomes, and organelle structures are no longer visible. Additionally, the nuclei are shrunken and have a star shaped halo surrounding the nuclear membrane, the size of which is dependent on the extent of accumulation (Figure 3 D).

Additionally, the degree of neuronal loss within the anterior horn was assessed temporally using a nuclear neuronal marker, NeuN (Figure 4 A-C). The number of NeuN positive cells within a defined region of the anterior horn were counted. Three

independent sets of spinal cords were evaluated, and the numbers were standardized as cells/mm^2. At 60 days, spinal cord samples across all three regions showed comparable anterior horn neuronal numbers between *hexb$^{+/+}$* and *hexb$^{-/-}$* mice. A similar trend was seen at 80 days and again was consistent throughout the three spinal cord regions. Later in disease progression, beginning at 100 days, a deterioration of neuronal numbers was observed in *hexb$^{-/-}$* spinal cords in comparison to *hexb$^{+/+}$* mice. By 120 days, severe neuronal loss was noted with a ~45% decrease in the cervical section, ~56% within the thoracic segment, and ~50% in the lumbar region. By the terminal stages of the disease an average of 50% of anterior horn neurons throughout the entire spinal cord had undergone cell death, which predictably resulted in a detrimental outcome (Figure 5 D,E). This data supports the notion that this specific population of spinal cord neurons is a major target for the disease and the loss of these neurons correlates with its clinical manifestation. Accompanying this mass neuronal loss and these intracellular variations, diseased neurons also appeared to have retracted and lost axonal projections starting as early as 40 days when compared to *hexb$^{+/+}$* neurons. (Figure 5 A-D).

To further document the neuronal variations observed during disease pathogenesis, the area of the cell body (um^2) and of the nucleus (um^2) were measured (Figure 6 A,B). As early as 60 days of age significant differences in the area of AHN cell bodies were noted between *hexb$^{+/+}$* and *hexb$^{-/-}$* mice. The area of the cell bodies of AHNs in *hexb$^{-/-}$* mice, increased in parallel with disease progression over time (Figure 6 C). Nuclear area exhibited an opposite trend in which the area decreased in *hexb$^{-/-}$* AHNs temporally

(Figure 6 D). At 60 days of age, the nuclear areas were similar between $hexb^{+/+}$ and $hexb^{-/-}$ AHNs, but a significant reduction was noted at 100- and 120-days old mice. Lastly, we compared the ratio of nuclear area to cell body area between $hexb^{+/+}$ and $hexb^{-/-}$ AHNs (Figure 6 E). At 60 days, the ratio was similar between $hexb^{+/+}$ and $hexb^{-/-}$ neurons, but this sharply changed at 80 days where $hexb^{-/-}$ AHNs showed a significant decrease in the nuclear/cell body ratio. This decrease in the ratio persisted from 80 days until the end point of the disease (120 days). These results indicated that lysosomal accumulation begins around 40 days of age and continues to amplify over time. Concurrently, the nuclear shrinkage/condensation observed throughout the disease acts as a potential indicator of apoptosis. These morphological differences accentuate the amount of neuronal damage occurring within $hexb^{-/-}$ mice.

Our lab has previously found increased expression of gliosis markers within the spinal cord of $hexb^{-/-}$ mice when compared with $hexb^{+/+}$ mice [69]. More specifically, GFAP levels were evaluated, and the number of activated astrocytes was quantified immunocytochemically to assess the level of astrogliosis. In $hexb^{+/+}$ spinal cord sections, most astrocytes showed very low GFAP immunoreactivity (Figure 3 B). In contrast, $hexb^{-/-}$ mice demonstrated overwhelming GFAP immunostaining indicating active astrogliosis within the spinal cord (Figure 3 E). Using immunofluorescence, a striking difference in GFAP activation was highlighted with early pathogenies (60d) showing very limited astrogliosis while endpoint (120d) mice again demonstrated a mass amount of astrocyte activation (Figure 3 G-P). MAC3 was also assessed in the spinal cord sections and

demonstrated large differences between *hexb*$^{+/+}$ and *hexb*$^{-/-}$ mice. MAC3, also known as LAMP2, showed no reactivity within the anterior horn neurons of the *hexb*$^{+/+}$ spinal cord (Figure 3 C). Spinal cord neurons in *hexb*$^{-/-}$ mice showed strong accumulation and staining within the cytoplasm (Figure 3 F). This is representative of the lysosomal accumulation that is a hallmark of lysosomal storage disorders.
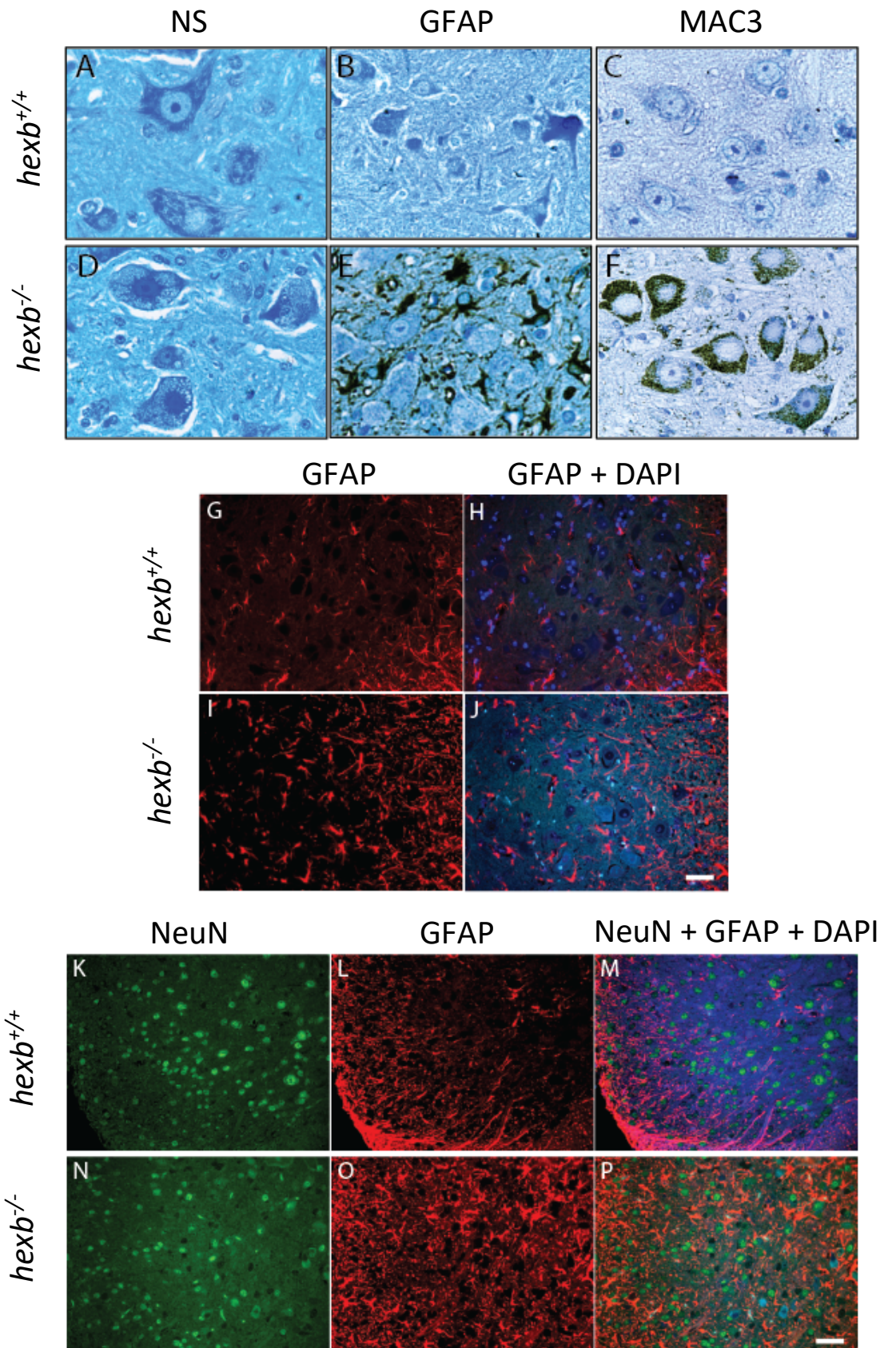
Figure 3. Deletion of *hexb*, creating a mouse model for SD, demonstrates a variety of morphological changes within the AHNs of the spinal cord, as well as increased GFAP and MAC3 immunoreactivity and severe neurodegeneration, determined by immunostaining. (**A-C**) Images of normal serum, GFAP, and MAC3/LAMP2 within the spinal cord, specifically the AHNs, of *hexb*$^{+/+}$ mice, respectively. The AHNs show good structural integrity, spherical nuclei, and conical/star-like shape. The AHNs are negative for both GFAP and MAC3/LAMP2 staining. (**D-F**) Normal serum, GFAP, and MCA3/LAMP2 immunoreactivity within the AHNs of *hexb*$^{-/-}$ mice. These neurons demonstrate vast lysosomal accumulation within the cytoplasm, a decline in structural integrity, swollen shape, and a halo surrounding the nuclear membrane. Images of spinal cord sections illustrates both GFAP and MAC3/LAMP2 staining in the AHNs, indicating activation of astrogliosis and lysosomal accumulation within the *hexb*$^{-/-}$ mice. (**G-H**) Immunofluorescence images of GFAP and GFAP+DAPI in the spinal cords of 60d *hexb*$^{+/+}$ mice showing very minimal astrogliosis. (**I-J**) Immunofluorescence images of GFAP and GFAP+DAPI in the spinal cords of 60d *hexb*$^{-/-}$ mice showing increased levels of astrogliosis induction in comparison to hexb$^{+/+}$ samples. (**K-M**) Immunofluorescence images of GFAP, NeuN and GFAP+NeuN+DAPI in the spinal cords of 120d *hexb*$^{+/+}$ mice showing very minimal astrocyte activation and a strong population of healthy neurons. (**N-P**) Immunofluorescence images of GFAP, NeuN, and GFAP+NeuN+DAPI in the spinal cords of 120d *hexb*$^{-/-}$ mice showing massively increased levels of astrogliosis induction and a marginal reduction in neuronal numbers in comparison to *hexb*$^{+/+}$ samples. Scale bar = 20um.
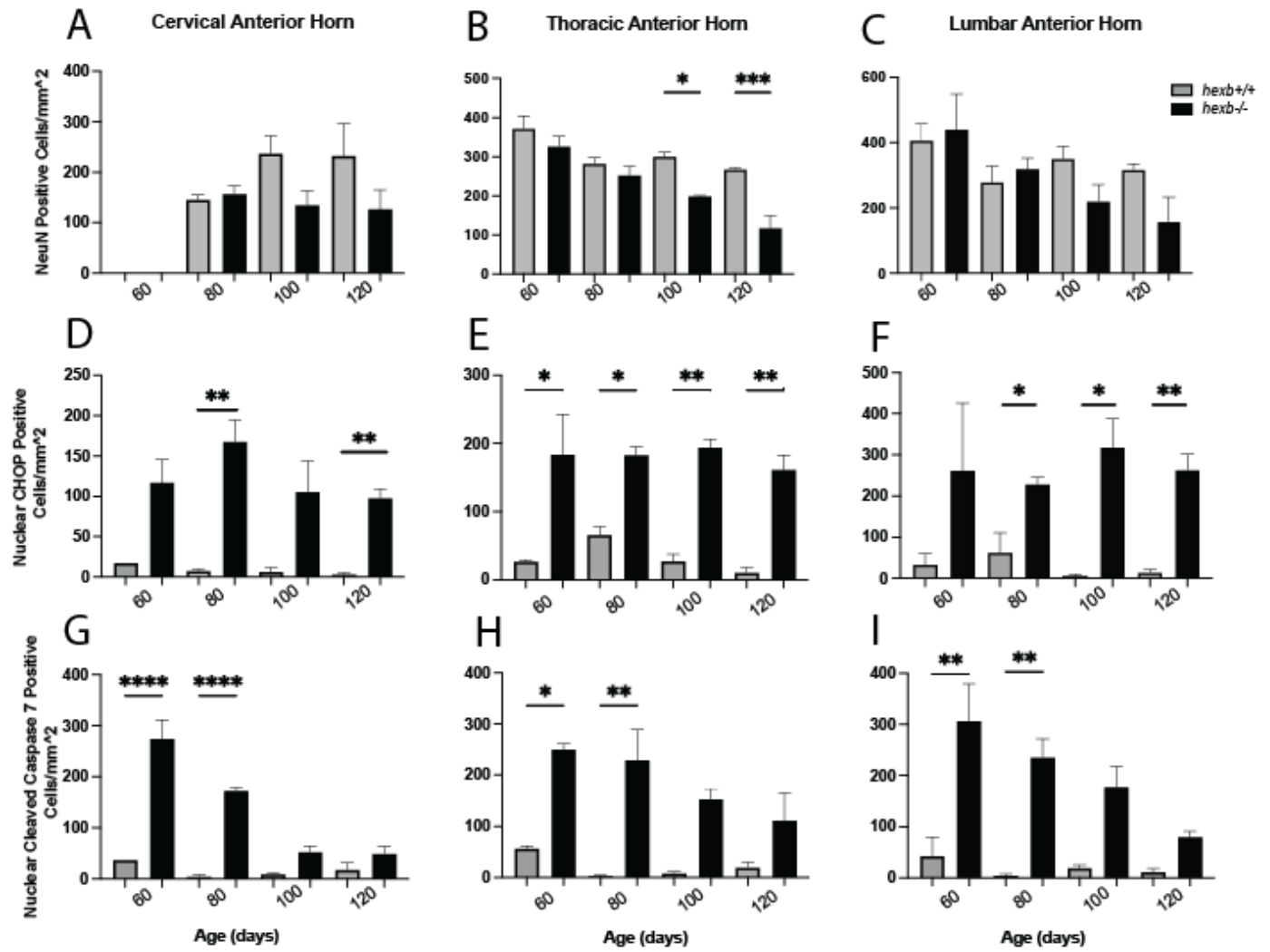
Figure 4. A quantitative analysis of neuronal numbers as well as the number of nuclear CHOP and nuclear cleaved caspase 7 positive cells within the anterior horn of immunohistological spinal sections from *hexb*$^{+/+}$ and *hexb*$^{-/-}$ (**A-C**) Quantification of neuronal numbers temporally in the development of SD for each specific region of the spinal cord in *hexb*$^{+/+}$ and *hexb*$^{-/-}$ mice. Each region demonstrates a similar stepwise pattern of neuronal loss in *hexb*$^{-/-}$ mice throughout the progression of SD, with relatively similar numbers seen consistently across the spinal cord regions of *hexb*$^{+/+}$ mice. (**D-F**) Quantification of nuclear CHOP positive cells temporally in the development of SD for each specific region of the spinal cord in *hexb*$^{+/+}$ and *hexb*$^{-/-}$ mice. Each region exhibited significant increases in the number of nuclear CHOP positive cells throughout development of SD. (**D**) Specifically, the cervical region demonstrated a peak of CHOP activation at 80d, (**E**) the thoracic region exhibits fairly consistent levels of CHOP activation across all ages, and (**F**) the lumbar region shows a later peak of CHOP at 100d. (**G-I**) Quantification of nuclear cleaved caspase 7 positive cells temporally in the development of SD for each specific region of the spinal cord in *hexb*$^{+/+}$ and *hexb*$^{-/-}$ mice. Each region exhibited significant increases in the number of nuclear cleaved caspase 7 positive cells during the early stages of SD development (60 and 80 days). All three regions also demonstrate a persistent stepwise reduction in cleaved caspase 7 activation, with each decrease corresponding to a later timepoint in disease pathogenesis. The lowest levels of nuclear cleaved caspase 7 positive cells were noted at 120d. (**G**) Specifically, the cervical region demonstrated a peak of cleaved caspase 7 activation at 60d, (**H**) the thoracic region

exhibits consistent levels of cleaved caspase 7 activation at both 60 and 80 days, and (**I**) the lumbar region also presented with a peak at 60d. n=3. *P ≤ 0.05, **P < 0.0022, ***P < 0.0002, ****P < 0.0001. Error bars, ±SEM.

hexb$^{+/+}$ *hexb*$^{-/-}$
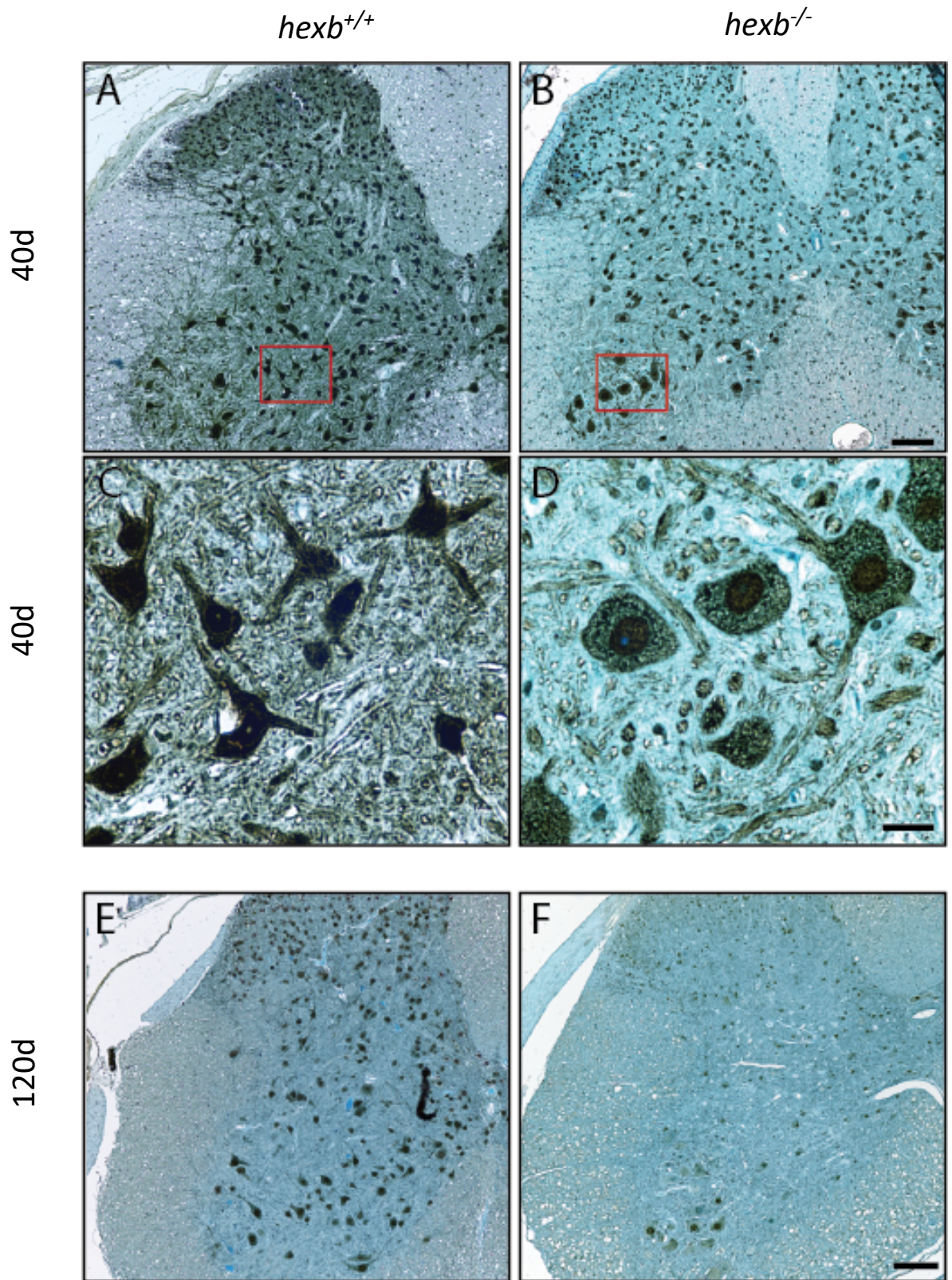
Figure 5. The mass neurodegeneration which is a hallmark of SD was evaluated temporally using a neuronal specific marker, NeuN, in the spinal cords of *hexb*$^{+/+}$ and *hexb*$^{-/-}$ mice. (**A-F**) NeuN immunostaining in the cervical region of the spinal cord of *hexb*$^{+/+}$ and *hexb*$^{-/-}$ mice. (**A**) A low magnification image of the vast NeuN immunoreactivity observed within 40d *hexb*$^{+/+}$ mice. (**B**) A low magnification image of NeuN immunoreactivity observed within 40d *hexb*$^{-/-}$ mice, which has already begun to show slight deterioration in comparison to *hexb*$^{+/+}$ samples. Scale bar = 100um. (**C-D**) High magnification images of anterior horn motor neurons of 40d *hexb*$^{+/+}$ and *hexb*$^{-/-}$ mice respectively, highlighting the retraction and loss of axonal extensions in the *hexb*$^{-/-}$ samples. Scale bar = 10um. (**E-F**) Low magnification images of NeuN immunoreactivity observed within 120d *hexb*$^{+/+}$ and *hexb*$^{-/-}$ mice, respectively, which shows a striking reduction in neuronal numbers compared to *hexb*$^{+/+}$ samples. Scale bar = 100um.
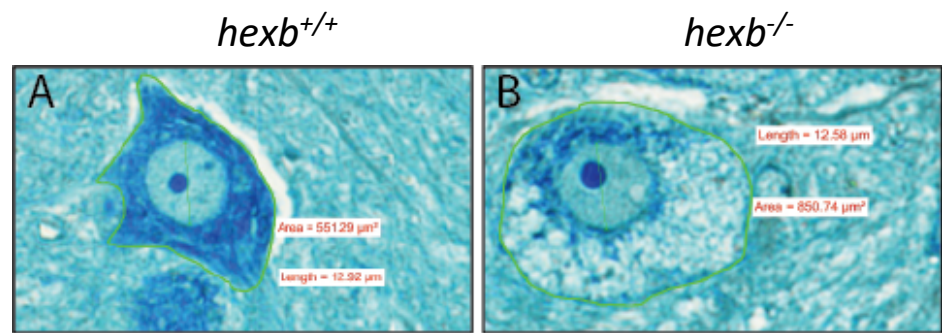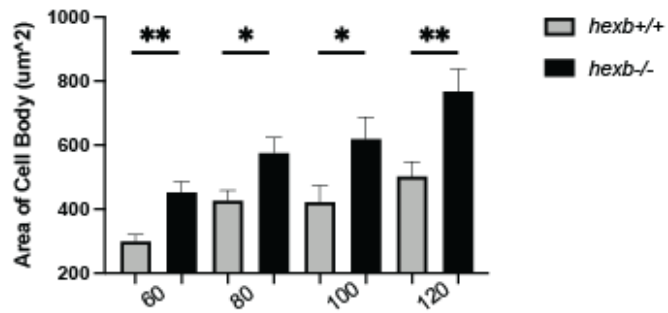
$hexb^{+/+}$ $hexb^{-/-}$
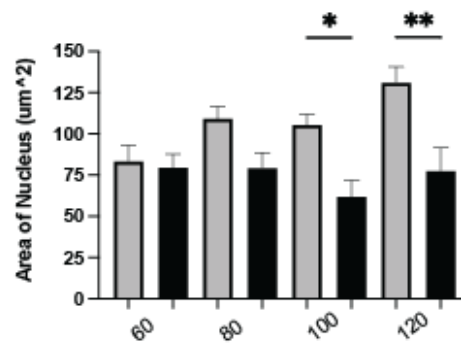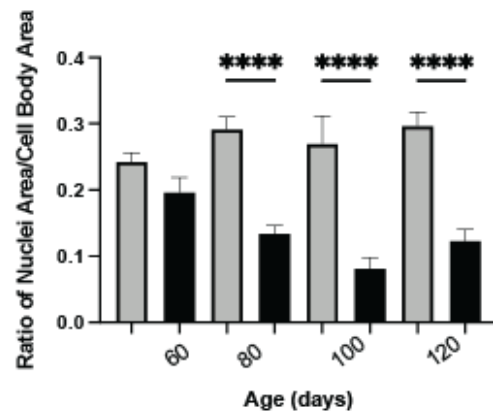
Figure 6. A quantitative analysis of neuronal morphological changes seen in the spinal cord motor neurons of *hexb*$^{+/+}$ and *hexb*$^{-/-}$ mice during the pathogenesis of SD. (**A-B**) Images of a single anterior horn motor neuron from *hexb*$^{+/+}$ and *hexb*$^{-/-}$ spinal cords, respectively. The anterior horn neuron from the *hexb*$^{+/+}$ spinal cord shows a sleek cell body and evidence of intracellular networks. The *hexb*$^{-/-}$ neuron highlights the massive vacuolar accumulation resulting in enlargement of the cell body, rippling of the cell membrane, and displacement of intracellular organelles. Area refers to the area of the cell body while length refers to the diameter of the nucleus. (**C-E**) Quantification of cell body area, nuclear area, and a ratio of nuclear area: cell body area, clearly demonstrates significant alterations in neuronal morphology which worsens in parallel with disease progression. (**C**) A progressive and significant increase in the area of the neuronal cell body can be noted in *hexb*$^{-/-}$ spinal cords when compared to *hexb*$^{+/+}$ samples. (**D**) An opposite trend is seen with nuclear area, in that it trends downwards in correlation with worsening lysosomal accumulations and increasing age, showing a significant decrease by 100 days in *hexb*$^{-/-}$ mice (**E**) The ratio reflects the results of both the area of the cell body and the nucleus. As cell body size increases, the nuclear area decreases, resulting in a smaller ratio of nuclear area to cell body area in *hexb*$^{-/-}$ spinal cord samples. There is a significant change observed beginning at 80d in *hexb*$^{-/-}$ mice in comparison to *hexb*$^{+/+}$. Cell Body Area n=9, nuclear area n=7, ratio n=6-7. *$P \leq 0.05$, **$P < 0.0022$, ***$P < 0.0002$, ****$P < 0.0001$. Error bars, ±SEM.

2. Expression Levels of ER Stress Markers

Neurodegeneration is a detrimental consequence observed in SD due to substrate accumulation. The events that connect the lysosomal storage of gangliosides to denervation within the CNS remain unknown. We hypothesized that the substrate accumulation within neurons of the spinal cord leads to ER stress induction and neuronal apoptosis. To assess if lysosomal storage leads to the activation and persistence of ER stress in the spinal cord, the global expression levels of multiple ER stress markers, including GRP78, ATF6, XBP1, IRE1-phos, and CHOP were examined using western blot analysis of cervical, thoracic, and lumbar spinal cord lysates from 120-day-old $hexb^{+/+}$ and $hexb^{-/-}$ mice (Figure 7). We recognize that expression of UPR markers in the total lysate of the spinal cords, which includes several cell types, does not accurately represent neuronal expression levels. Nevertheless, differential expression among the distinct regions of the spinal cord was observed. The expression of ER chaperone protein, GRP78, showed comparable expression within the cervical spinal segment of $hexb^{-/-}$ mice relative to $hexb^{+/+}$ mice. Similar trends in expression levels were observed in the thoracic and lumbar spinal segments. Next, phosphorylated IRE1 showed similar levels of expression in the cervical region and lumbar regions, while the thoracic section of the spinal cord showed increased levels, indicating that the IRE1/XBP1 pathway is being activated during the late stages of the disease. In addition, ATF6 levels were also elevated within the cervical and lumbar regions of $hexb^{-/-}$ mouse spinal cords with the thoracic section showing a decrease. Furthermore, XBP1, a potent downstream transcription factor regulated by ATF6 and

phosphorylated IRE1, also demonstrated comparable levels within the cervical and lumbar regions in *hexb*^{-/-} mice. However, XBP1 had reduced expression within the thoracic segment. Lastly, the pro-apoptotic factor CHOP was investigated to determine if severe and prolonged ER stress, which can result in apoptosis, exists within *hexb*^{-/-} spinal cord segments. Elevated expression levels of CHOP were observed within the cervical and lumbar regions of the spinal cord of *hexb*^{-/-} mice in relation to *hexb*^{+/+} mice. This suggests that the global ER stress within the cervical and lumbar regions appears to be more severe. Overall, these results demonstrate that ER stress is being induced within the spinal cords of *hexb*^{-/-} mice and that the stress is persistent and severe.
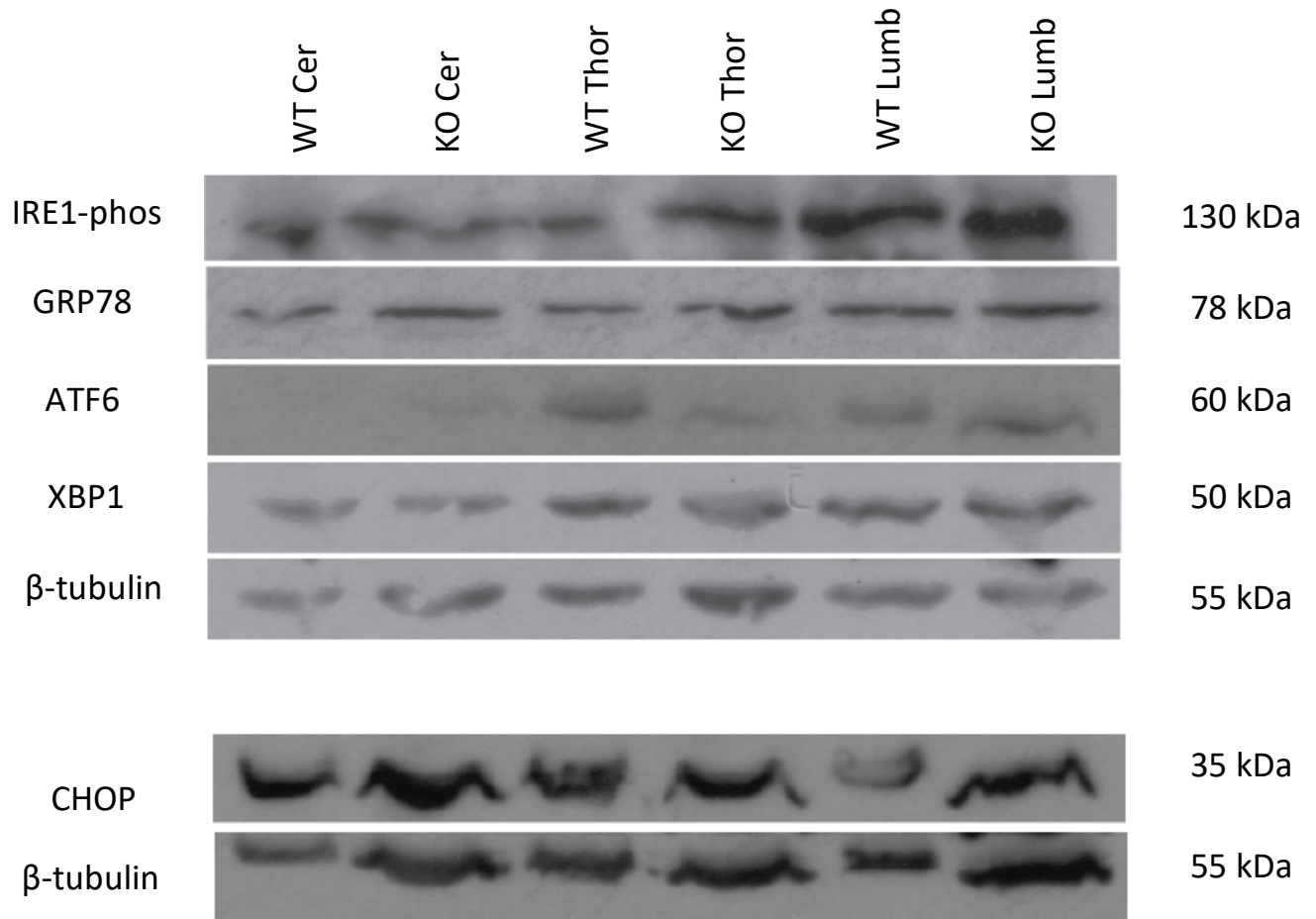
Figure 7. The targeted disruption of the *hexb* gene in mice results in ER stress marker elevation. Phosphorylated IRE1, GRP78, ATF6, XBP1, and CHOP expression were assessed in the spinal cord of 120-day-old *hexb$^{+/+}$* and *hexb$^{-/-}$* mice using western blot analysis. β-tubulin was used a loading control. Phosphorylated IRE1 expression shows a trend of upregulation in *hexb$^{-/-}$* mice in the thoracic region with similar levels in the cervical and lumbar segments of the spinal cord in comparison to *hexb$^{+/+}$* mice. GRP78 demonstrates comparable levels expression across all regions of *hexb$^{-/-}$* spinal cords in relation to *hexb$^{+/+}$* samples. ATF6 expression revealed upregulation within the lumbar regions of *hexb$^{-/-}$* mice, comparable levels in the thoracic region with no signal apparent in *hexb$^{+/+}$* and *hexb$^{-/-}$* mice cervical regions. XBP1 expression demonstrates comparable levels in the cervical and lumbar regions of *hexb$^{-/-}$* spinal cord samples in relation to in *hexb$^{+/+}$* samples. However, within the thoracic region, XBP1 expression appears to be downregulated relative to *hexb$^{+/+}$* expression levels. CHOP appears to have an increase in *hexb$^{-/-}$* with the cervical and lumbar regions relative to *hexb$^{+/+}$* mice with similar levels noted within the thoracic segment.

3. Immunocytochemical Localization of ER Stress Markers

The expression analysis using western blots alludes to the occurrence of ER stress in the spinal cord of $hexb^{-/-}$ mice, with interesting interregional variations. To examine the expression levels of UPR markers at the cellular level, we examined the immunocytochemical localization of ER stress markers between and within each of the spinal cord regions, specifically in AHNs. Immunocytochemistry was performed on paraffin-embedded sections of spinal cords from 120-day-old $hexb^{-/-}$ and $hexb^{+/+}$ mice using several markers of ER stress: GRP78, PDI, ATF6, XBP1, and CHOP, as well as PARP, a marker of apoptosis (Figure 8, Figure 9). We also included a negative control using normal mouse serum to verify that the staining seen within $hexb^{+/+}$ and $hexb^{-/-}$ spinal cord sections was specific (Figure 8 A,B). The examination of the expression of these markers spatially within the spinal cord, and their intracellular localization provides insight regarding spinal cord histopathology, and morphological alterations of AHNs, allowing for a more comprehensive understanding of how this disease impacts the neurons.

$hexb^{+/+}$ $hexb^{-/-}$
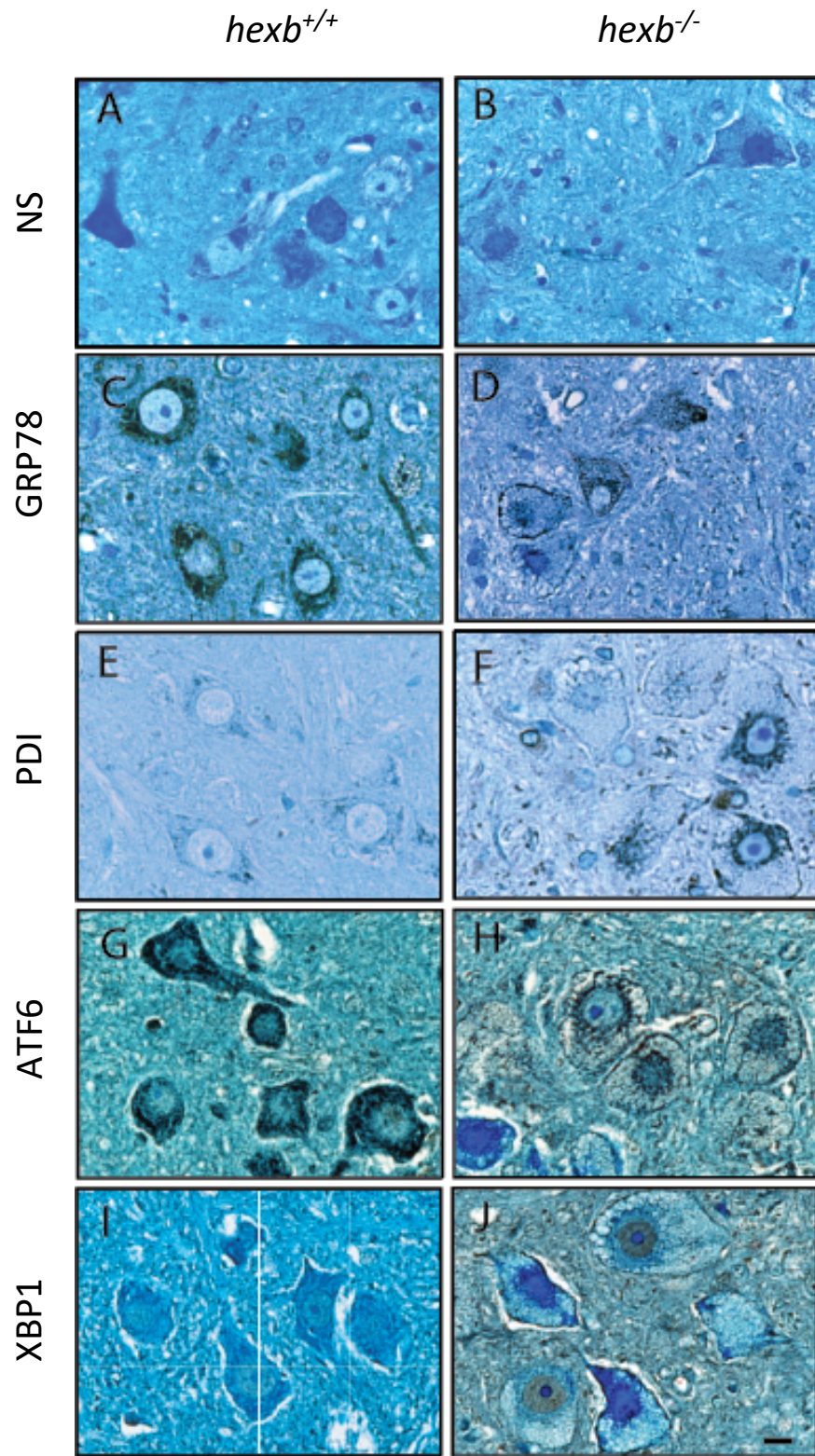
Figure 8. A summary ER stress marker, GRP78, PDI, ATF6, and XBP1, and their immunohistological intracellular localization within the anterior horn motor neurons of 120-day-old *hexb*$^{+/+}$ and *hexb*$^{-/-}$ mouse spinal cords. (**A-B**) A negative control of *hexb*$^{+/+}$ and *hexb*$^{-/-}$ spinal cord sections, using normal mouse serum, was included to demonstrate that staining present within these experiments was due to a reaction with the antibody and was not non-specific. Both the *hexb*$^{+/+}$ and *hexb*$^{-/-}$ spinal cord neurons showed no reactivity. (**C-D**) The localization of resident ER chaperone GRP78 within motor neurons of *hexb*$^{+/+}$ and *hexb*$^{-/-}$ mouse spinal cords. (**C**) At high magnification, GRP78 follows a punctate pattern within the cytoplasm known as Nissl bodies, indicating that GRP78 is being sequestered within the ER under non-stressed conditions. (**D**) In *hexb*$^{-/-}$ motor neurons GRP78 displays multiple cellular localizations including the cell membrane, cytosol, and ER, which is now restricted around the nucleus. There is a loss of the Nissl body staining pattern in diseased motor neurons. (**E-F**) The localization of resident ER chaperone PDI within anterior horn motor neurons of *hexb*$^{+/+}$ and *hexb*$^{-/-}$ mouse spinal cords. (**E**) At the cellular level PDI is evident in the cytoplasm where it accumulates within Nissl bodies creating a punctate pattern. (**F**) In *hexb*$^{-/-}$ mice, the cellular distribution of PDI is more concentrated but remains within the cytoplasm. The sequestration pattern in these neurons indicates the ER has been pushed towards the nucleus due to the vast amount of accumulation occupying much of the cytoplasmic space. (**G-H)** The localization of ER stress marker ATF6 within the motor neurons of the anterior horn of *hexb*$^{+/+}$ and *hexb*$^{-/-}$ mouse spinal cords. (**G**) Clear cytosolic staining is observed in *hexb*$^{+/+}$ neurons indicating inactive

and ER bound ATF6. (**H**) Contrastingly, *hexb^{-/-}* neurons demonstrate a combinatory staining pattern with many cells now exhibiting nuclear localization of ATF6. This is indicative of its activation, cleavage, and subsequent translocation to the nucleus. (**I-J**) The localization of ER stress marker XBP1 within anterior horn neurons in *hexb^{+/+}* and *hexb^{-/-}* mouse spinal cords. (**I**) Within the anterior horn of the *hexb^{+/+}* sections, XBP1 is seen within the cytoplasm of neurons with a select number showing mild nuclear staining. (**J**) In *hexb^{-/-}* mice, the immunoreactivity of XBP1 demonstrates strong nuclear accumulation in anterior horn motor neurons, resulting in little cytoplasmic staining, which is a clear differentiation from the *hexb^{+/+}* cells. This indicates XBP1 activation and translocation in response to ER stress. Scale bar = 10um.

3.1. ER Chaperone Proteins, Sensors of ER Stress

ER chaperone proteins contribute significantly to the continued maintenance of proper ER functioning through increasing protein folding efficiency, regulating Ca^{2+} homeostasis, and of most significance, their ability to detect ER stress within the cell (30). GRP78, which is one of the most abundant proteins within the ER, holds the 3 arms of the UPR inactive and is imperative in the activation of the ER stress response (32). In spinal cord sections collected from *hexb*$^{+/+}$ mice, GRP78 staining was observed in all three regions of the spinal cord with intraregional variability of its dispersal. Within the dorsal horn mild staining was observed, with slightly heavier staining within the intermediate column and anterior horn. Comparing GRP78 immunoreactivity interregionally in wild type mice indicted that the thoracic segment contained elevated staining intensity in comparison to the cervical and lumbar segments. At a cellular level, GRP78 showed a unique punctate cytoplasmic pattern illustrated by the dark spots scattered throughout the cytoplasm (Figure 8 C). These punctations are known as Nissl bodies which contain rough ER. This type of staining aligns with the functionality of GRP78, as it contributes to the formation of functional proteins, and its intracellular localization within the ER under nonstress conditions. The distinct visibility and vast dispersal of the Nissl bodies within the cytoplasm was noted. In contrast, *hexb*$^{-/-}$ spinal cord sections showed a decrease in the staining intensity per cell, but the total staining levels in each region of the spinal cord showed increases in the number of cell types that contain GRP78 staining.

In *hexb*$^{-/-}$ mice, a modest increase in the amount of immunoreactivity within cells of the dorsal horn of the cervical section was observed when compared to the *hexb*$^{+/+}$ samples. Sections from *hexb*$^{-/-}$ mice appeared to show less intense accumulation of GRP78 within the anterior horn in comparison to the *hexb*$^{+/+}$, potentially due to the extensive change in intracellular localization caused by lysosomal storage and ER stress activation. Supporting this notion, the spinal motor neurons displayed clear localization discrepancies of GRP78 between the *hexb*$^{+/+}$ and the *hexb*$^{-/-}$ mice, as well as variation exclusively within the AHNs of *hexb*$^{-/-}$ mice. Specifically, AHNs present in the cervical spinal section showed staining localized to a halo surrounding the nuclear membrane, while neurons within the thoracic region displayed a combination of diffuse cytosolic and cellular membrane localization (Figure 8 D). The cytoplasmic staining seen within these knockout neurons was immensely different from the Nissl bodies seen within the *hexb*$^{+/+}$, as the staining was now diffused throughout the entire cytoplasm and the punctate patterning was no longer present. Overall, the variation in the total amount of staining within the spinal cord sections and the unique cellular localization seen within the *hexb*$^{-/-}$ sections suggested that ER stress is activated and changes in GRP78 occurred in response.

A second ER resident protein, PDI, was also evaluated because of its significant functions within the ER, including disulfide formation and protein folding. PDI in response to stress, like GRP78, has been reported to be upregulated as the cell attempts to reduce the load of misfolded proteins accumulating in the ER. The *hexb*$^{+/+}$ spinal cord segments showed very minimal staining which was mainly restricted within the anterior horn. PDI

exhibited identical intracellular localization as GRP78, with the degree of staining being much less intense for PDI. Nissl bodies were again prevalent throughout the cytoplasm of the AHNs. Due to the less intense nature of PDI's stain, the highly specific sequestration within Nissl bodies was observed with a greater magnitude (Figure 8 E). In sharp contrast to the $hexb^{+/+}$, the $hexb^{-/-}$ spinal cord sections showed an amplification in the total amount of staining seen within each section. An evaluation of staining dispersal intraregionally revealed that the dorsal horn cell population contained the least amount of PDI immunoreactivity in comparison to the intermediate column and anterior horn. Again, $hexb^{-/-}$ spinal cord motor neurons showed a conspicuous shift in the localization and staining intensity in contrast to the intracellular localization seen in $hexb^{+/+}$ AHNs. Neurons showing heavy lysosomal accumulations typically showed PDI localization in a halo around the nucleus (Figure 8 F). This sequestration pattern, paired with an identical observation seen with GRP78 in $hexb^{-/-}$ motor neurons, suggested that due to the amount of accumulation within the lysosomes, the ER becomes constricted against the nuclear membrane creating a halo encompassing the nucleus. Neurons with a lesser degree of accumulation showed fewer Nissl bodies paired with intense, diffused cytosolic staining, all of which is indicative of PDI upregulation. Taken together, the results of these ER chaperone proteins immunoreactivity and localization within $hexb^{-/-}$ spinal samples provided evidence of increased ER stress activation, alterations in chaperone protein expression, and accentuated substrate accumulation within lysosomes which disrupts organelle intracellular localization.

3.2. Indicators of Activation for UPR Signal Cascades

The ER stress response consists of multiple pathways that work in concert to initiate a variety of downstream cellular events that will either act to protect the cell, i.e., pro-survival, or in the case of severe and prolonged ER stress will result in the triggering of apoptotic events. To begin to dissect this complex process, we characterized changes in the immunocytochemical localization of ATF6 and XBP1 within *hexb*$^{-/-}$ spinal cords compared to *hexb*$^{+/+}$ mice. ATF6 is a membrane bound ER protein that is cleaved and activated, allowing for it to act as a potent transcription factor that stimulates upregulation of XBP1 mRNA expression. XBP1 mRNA is subsequently processed by phosphorylated IRE1 to create its activated form, which can then enter the nucleus where it acts to upregulate a variety of UPR target genes. Based on the results of GRP78 and PDI immunolocalization within AHNs, we hypothesized that ATF6 and XBP1 would also demonstrate differences in their localization between *hexb*$^{-/-}$ and *hexb*$^{+/+}$ spinal samples indicative of their activation.

In the *hexb*$^{+/+}$ spinal cord sections, ATF6 immunoreactivity was observed throughout each of the three regions, with more intense staining focused within the AHNs and dorsal horn. Between the three sections, the lumbar region showed marginally less staining in comparison to the cervical and thoracic regions. Within the AHNs specifically, equally diffuse and intense cytoplasmic staining was observed (Figure 8 G). This localization pattern indicated the presence of inactive, ER bound ATF6 within the cell. The *hexb*$^{-/-}$ spinal sections demonstrated decreased amounts of overall staining, especially within the

cervical region. Upon examination of intracellular localization, we noted a marked change from cytosolic, in the *hexb^{+/+}*, to primarily nuclear accumulation within the AHNs of *hexb^{-/-}* mice (Figure 8 H). Nuclear staining of ATF6, which is a conformational indicator that ATF6 was cleaved, indicated that it was now functioning as a transcription factor, and that the UPR was instigated within these spinal cord neurons. Interestingly and unique to ATF6, we observed that in all three regions there were enhanced levels of staining specifically in the dorsal horn. Next, XBP1 localization and immunoreactivity discrepancies between *hexb^{+/+}* and *hexb^{-/-}* mice were examined. Spinal sections of *hexb^{+/+}* mice showed XBP1 immunoreactivity dispersed throughout each region, with a decline in staining intensity moving posteriorly through the section. The AHNs mainly exhibited cytosolic staining with a discrete number of cells presenting with nuclear staining (Figure 8 I). Cytosolic staining is indicative of inactivate XBP1, which was expected under homeostatic cellular conditions. In contrast, the knockout spinal cord sections appeared to have a lower amount of total staining within the regions, with the ventral horns displaying more concentrated XBP1 staining. The AHNs clearly showed lipid accumulation within the lysosomes but more importantly they exhibited salient nuclear XBP1 accumulation that was not detected in the *hexb^{+/+}* spinal cord samples (Figure 8 J). XBP1 cleavage, which activates its ability to regulate transcription of UPR target genes, is completed after the induction of ER stress. This allows for the translocation of XBP1 to the nucleus, which was the localization pattern observed in the AHNs of *hexb^{-/-}* mice. Activated ATF6 and XBP1, both with clear nuclear localization within the *hexb^{-/-}* spinal cord sections, provided

further evidence that ER stress response was highly activated and that at least 2 of the 3 UPR signaling mechanisms were involved.

3.3. Terminal Stress and Cellular Apoptosis

The intensity of the ER stress we had observed within the spinal cord of *hexb$^{-/-}$* mice led us to determine if ER stress could potentially result in neuronal apoptosis. This was achieved by evaluating the localization of CHOP, a pro-apoptotic factor, as well as cleaved caspase 7 and cleaved PARP, potent regulators of apoptosis (Figure 9). CHOP is an important downstream factor to explore because it plays a vital role in the cells decision to undergo apoptosis and its expression can be regulated by all 3 arms of the UPR. All three wild type *hexb$^{+/+}$* spinal sections, at low magnification, appear negative for CHOP staining. Upon examination of AHNs specifically, we noted a small number of neurons had cytosolic staining or, in a few rare cases, nuclear staining, otherwise most other AHNs were void of CHOP immunoreactivity (Figure 9 A). In contrast, *hexb$^{-/-}$* mice spinal cords sections showed strong CHOP immunostaining. Within the cervical, thoracic, and lumbar regions there was a very sharp increase in the total number of cells exhibiting CHOP immunoreactivity in all intraregional locations. There was also a dramatic difference in the intracellular localization of CHOP in AHNs. These neurons showed strong accumulation in the nucleus resulting in intense staining (Figure 9 B). The morphological effects of lipid accumulation, such as engorged structures, ER halos around the nucleus, and loss of cell membrane integrity were quite noticeable in the AHNs. This type of accumulation suggests that there had been prolonged ER stress within these cells and CHOP had been

invoked. To expand the understanding of the differences in CHOP expression between

hexb$^{+/+}$ and *hexb*$^{-/-}$ mice, we quantified the number of nuclear CHOP positive cells within

the anterior horn of spinal cord sections (Figure 4 D-F). This was completed by counting

the total number of cells within the anterior horn of the cervical, thoracic, and lumbar

regions, that presented with strictly nuclear CHOP staining. These results provide

evidence that there are interregional differences within the spinal cord and that the

thoracic and lumbar regions, at end point, exhibit slightly stronger signs of apoptosis,

demonstrated by the augmentation of cells containing nuclear CHOP staining.

A potent inducer of apoptosis is cleaved caspase 7 (c-Cas7), an executioner caspase,

which, upon its cleavage, becomes activated and localizes to the nucleus where it

processes and activates PARP, a signature of cell death in neurodegeneration. Therefore,

we evaluated its immunohistological localization and expression between 120-day-old

hexb$^{+/+}$ and *hexb*$^{-/-}$ mice. In *hexb*$^{+/+}$ samples, ultimately no staining was observed

throughout all three regions of the spinal cord. AHNs were negative for staining except

for a few cells which presented with weak nuclear staining (Figure 9 C). On the contrary,

hexb$^{-/-}$ mice exhibited differential levels of expression. The staining was widely dispersed

within and between each region of the spinal cord and AHNs of each section presented

with clear, intense nuclear accumulation of c-Cas7 (Figure 9 D). Obvious engorgement of

AHNs and disruption in cellular integrity can be observed concurrently with this nuclear

localization and activation of c-CAS7. The striking difference of c-CAS7 immunoreactivity

between *hexb$^{+/+}$* and *hexb$^{-/-}$* mice highlights a novel mechanism of neurodegeneration in SD.

Lastly, as an evaluation of the prevalence of apoptosis within the spinal cord of *hexb$^{-/-}$*, the immunoreactivity of cleaved PARP was examined. Cleaved PARP staining was not generally observed within *hexb$^{+/+}$* spinal section. The vast majority of spinal motor neurons located within the anterior horn exhibited no staining, which was expected under homeostatic conditions (Figure 9 E). The *hexb$^{-/-}$* sections, in contrast, showed an increase in the global staining of cleaved PARP throughout all regions of the spinal cord. Specifically, the localization of cleaved-PARP staining within the AHNs of *hexb$^{-/-}$* was intense and strictly nuclear (Figure 9 F). This exclusively nuclear localization of cleaved PARP indicated it had been cleaved and the apoptotic pathway had been activated. Overall, the results observed strongly support the notion that PARP is being activated as a downstream factor in response to lysosomal accumulation and potentially ER stress within the spinal cord of *hexb$^{-/-}$* mice. This in turn results in the induction of apoptotic pathways which can account for the drastic neurodegeneration seen in this disease.

In summary, these results provided evidence that severe ER stress, caused by lysosomal accumulation, is present within the spinal cords of *hexb$^{-/-}$* mice and this is accompanied by increased rates of apoptosis. Using ER stress markers, we were able to identify intraregional differences within the spinal cord including morphological alterations and drastic intracellular localization changes specifically within AHNs.

$hexb^{+/+}$ $hexb^{-/-}$
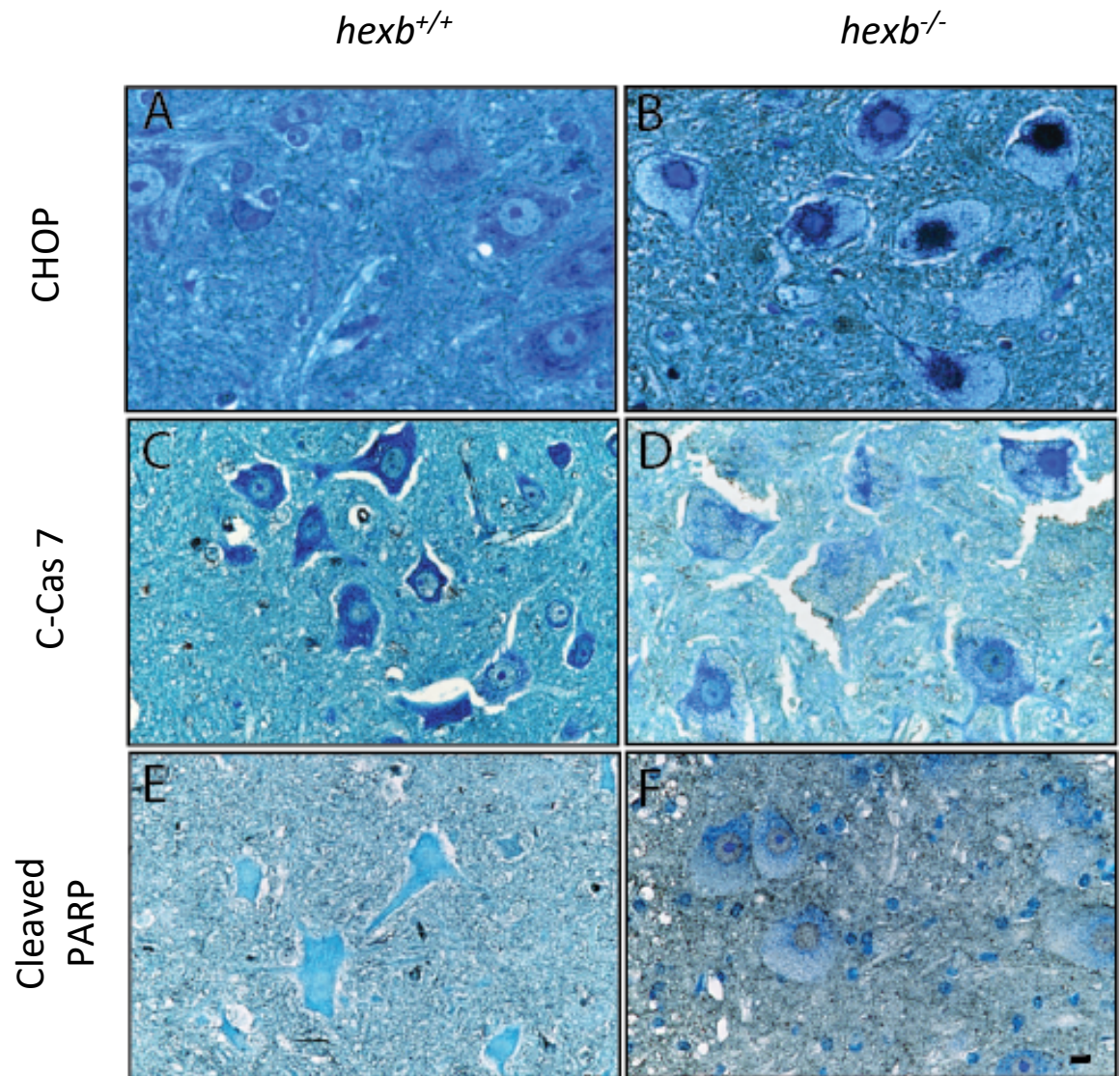
Figure 9. A summary of pro-apoptotic, CHOP, and apoptosis inducing markers, cleaved caspase 7 and cleaved PARP, and their immunohistological intracellular localization within the anterior horn motor neurons of 120-day-old *hexb*$^{+/+}$ and *hexb*$^{-/-}$ mouse spinal cords. (**A-B**) The localization of CHOP within the motor neurons *hexb*$^{+/+}$ and *hexb*$^{-/-}$ mouse spinal cords. (**A**) AHNs of *hexb*$^{+/+}$ mice showed normal morphology and the majority of cells were negative for CHOP staining or showed staining within the cytosol, with a very limited number showing nuclear staining. (**B**) Contrary to what was observed within *hexb*$^{+/+}$ samples, the motor neurons of *hexb*$^{-/-}$ mice presented with strong accumulation of CHOP staining within the nucleus in addition to severe morphological changes. Localization of CHOP in the nucleus denotes its upregulation and activation due to ER stress. (**C-D**) The intracellular localization of cellular apoptosis marker cleaved caspase 7 in *hexb*$^{+/+}$ and *hexb*$^{-/-}$ mouse motor neurons. (**C**) The *hexb*$^{+/+}$ anterior horn neurons ultimately showed no immunoreactivity, except for a few neurons which demonstrated very weak nuclear staining. (**D**) Contrastingly, *hexb*$^{-/-}$ neurons showed strong nuclear accumulation, indicating activation of cleaved caspase 7 and initiation of apoptotic cascades. (**E-F**) Localization pattern of cellular apoptosis marker cleaved PARP within anterior horn motor neurons in *hexb*$^{+/+}$ and *hexb*$^{-/-}$ mouse spinal cords. (**E**) Motor neurons of *hexb*$^{+/+}$ mice were relatively negative for cleaved PARP immunostaining, which is expected under homeostatic conditions. (**F**) Disease motor neurons exhibited a strong increase in staining accompanied by localization of cleaved PARP to the nucleus. This indicates its activation and again the activation of apoptotic signaling cascades. Scale = 10um.

80

Disease Pathogenesis Developmentally

Following the identification of ER stress as a major mechanistic pathway involved in the terminal aspect of SD, the question as to how does the induction ER stress and the UPR change developmentally throughout the disease emerged. The above data indicated that a mass neuronal death occurs during the progression of SD; however, the timeline of these events during development and what factors are playing significant roles required further investigation. We therefore evaluated the relationship between SD pathology, UPR activation, and symptom onset/progression at different ages of the SD mouse model.

Expression of ER Stress Markers Within the Spinal Cord During Development

In continuation of the observations seen with the immunostaining at 120-days, we examined the immunocytochemical localization of ER stress markers developmentally throughout the progression of SD. This analysis focused on the intracellular localization of these markers, specifically within AHNs. Immunocytochemistry was performed on paraffin-embedded spinal cords sections from 60, 80, and 100-day-old *hexb*$^{-/-}$ and *hexb*$^{+/+}$ mice using several markers of ER stress: GRP78, ATF6, XBP1, and CHOP, as well as cleaved caspase 7 and cleaved PARP; the latter two are markers of apoptosis. The examination of the expression of these markers spatially within the spinal cord, and their intracellular localization provides insight regarding mechanistic pathways which contribute to the pathology of SD, as well as morphological alterations of AHNs, allowing for a more comprehensive understanding of how this disease impacts neurons within the spinal cord.

1. Redistribution and Altered Expression of ER Chaperone Protein

As previously mentioned, GRP78 is a widely abundant ER chaperone protein that plays a role in sensing and responding to ER stress. Under homeostatic conditions GRP78 holds the three arms of the UPR inactive. In *hexb*$^{+/+}$ spinal cord samples GRP78 was present within all three regions at 60, 80, and 100-days (Figure 10 A,C,E). Similar to the 120-day findings, the intraregional dispersion varied at every age. The posterior horn had lower levels of staining when compared to the intermediate column and the anterior horn. When examined at the cellular level, GRP78 continued to exhibit unique punctate cytoplasmic sequestration that was observed in the 120-day *hexb*$^{+/+}$ sections. The distinct visibility of Nissl bodies within the cytoplasm and dispersed staining pattern was representative of the functional role of GRP78 within the ER during homeostatic conditions. The intensity and pattern of staining appeared consistent across the various ages. This was in sharp contrast to the *hexb*$^{-/-}$ sections which showed GRP78 tapering off following the course of disease progression.

By 60d of age sections of the *hexb*$^{-/-}$ spinal cords showed a mild reduction in immunoreactivity but many AHNs presented with heavy, punctate, ER staining (Figure 10 B). The cervical and thoracic regions showed slight variation in the cytosolic dispersal of GRP78, with some neurons showing loss of the highly specific punctate pattern and began to demonstrate more diffuse staining. Overall, at this age the knockout AHNs still closely resemble the staining seen within the neurons of the wild type mice. This observation does not hold in older mice. At 80-days, there is a sharp decline in the intensity of the

GRP78 immunostaining in the *hexb*$^{-/-}$ sections across all regions of the spinal cord (Figure 10 D). Consistent with this notion, the spinal motor neurons showed clear incongruities in localization of GRP78 between the *hexb*$^{+/+}$ and the *hexb*$^{-/-}$ mice, as well as variation specifically within the AHNs of *hexb*$^{-/-}$ mice. During ER stress the role of GRP78 becomes highly important to assist in the restoration of homeostatic conditions and therefore can result in a diverse range of intracellular localizations. AHNs present across all three regions of the spinal cord displayed immunostaining localized to a halo surrounding the nuclear membrane, similar to the staining pattern seen in the 120-day samples. Note that AHNs within the cervical segments of the spinal cord predominantly displayed staining within the ER halo while the thoracic and lumbar neurons highlighted a combination of cell surface and diffuse cytosolic GRP78 staining. The cytoplasmic staining seen within the *hexb*$^{-/-}$ neurons was drastically different from the Nissl bodies present in the *hexb*$^{+/+}$ samples. The staining seen was more diffused throughout the entirety of the cytoplasm with a loss of the distinct punctate pattern noted in the wild type. Similar staining distribution was seen within the 100-day samples (Figure 10 F). The *hexb*$^{-/-}$ samples exhibited a widely dispersed cytosolic staining with several neurons showing strong staining within the ER halo and at the cell membrane, while the classic intense punctate, immunolabeling was observed in *hexb*$^{+/+}$ sections. Note that the drastic reduction in immunostaining intensity between *hexb*$^{+/+}$ and *hexb*$^{-/-}$ was still observed, as previously noted in the 80-day group.

Overall, the relocalization of GRP78 within the *hexb*$^{-/-}$ spinal segments is indicative of its activation caused by ER stress induction, which starts as early as 60 days. A drastic change in immunostaining intensity between 60 and 80 days was also observed, suggesting a potential change in GRP78 abundance and mechanistic ability, as well as a loss of ER functionality. Further supporting this notion is the formation of an ER halo surrounding the nuclear envelope beginning at 60 days and becoming increasingly evident by 80 and 100 days. This indicates a disruption in the ER network due to lysosomal accumulation, causing the ER to be pushed against the nucleus, starting early in disease pathogenesis. This disruption, in combination with an apparent reduction in GRP78, can result in a whole host of consequences involving cellular function and homeostatic regulation, all of which can potentiate ER stress and UPR activation.

hexb^{+/+}   *hexb*^{-/-}
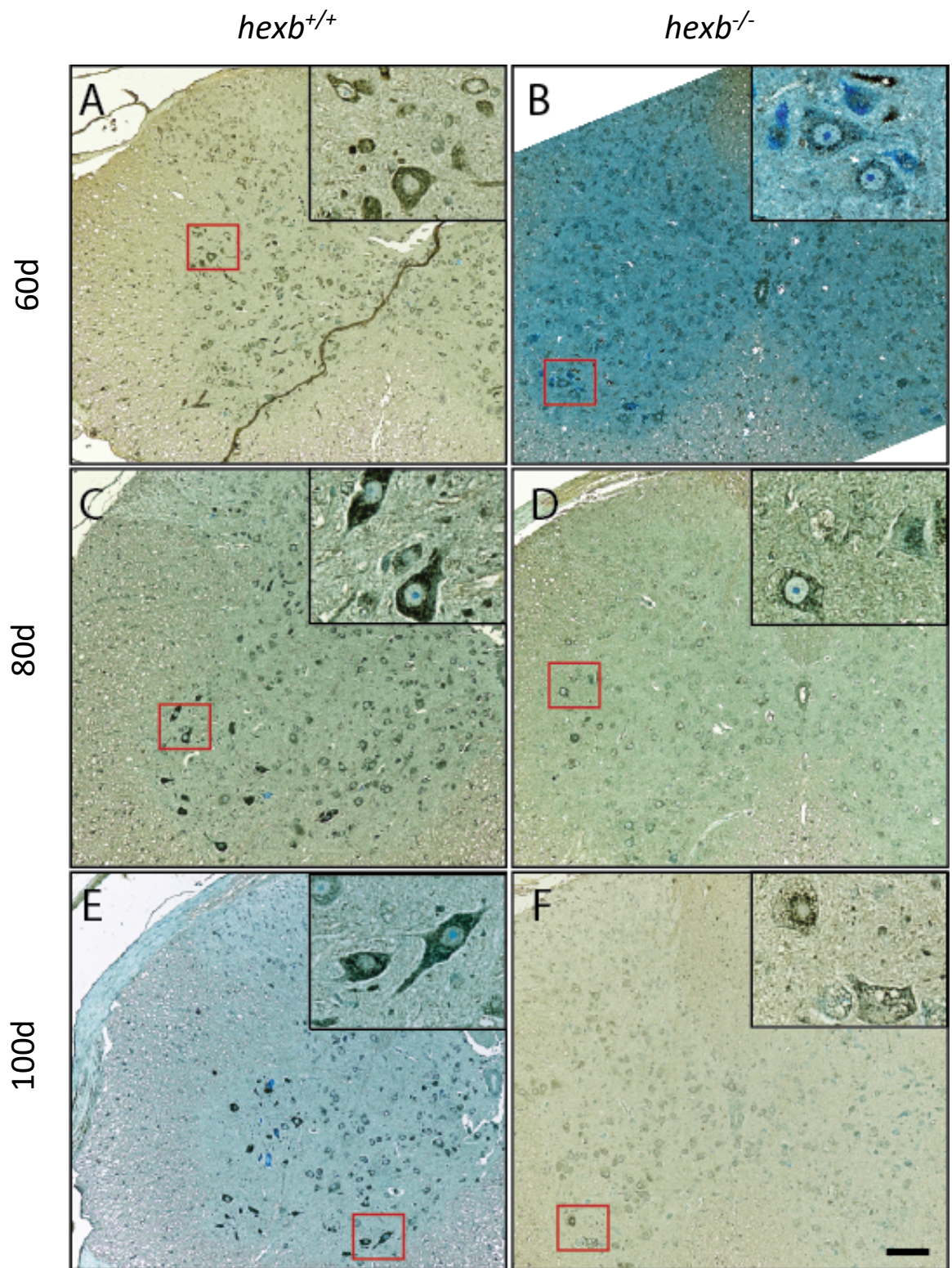
Figure 10. The localization of resident ER chaperone GRP78 developmentally within the cervical spinal cord region of 60-, 80-, and 100-day old *hexb$^{+/+}$* and *hexb$^{-/-}$* mice. Immunocytochemical localization in paraffin- embedded sections of *hexb$^{+/+}$* and *hexb$^{-/-}$* mouse spinal cords of GRP78 specifically among the population of anterior horn motor neurons. (**A,C,E**) The spinal cords of *hexb$^{+/+}$* at 60, 80, and 100 days, respectively, consistently demonstrated a punctate, reticular staining pattern with intense levels of immunostaining. (**B,D,F**) In contrast, *hexb$^{-/-}$* samples highlighted a decrease in global staining of GRP78 as well as a redistribution to the cell membrane and cytosol, with some cells still showing reticular staining, across all ages. This reticular staining pattern differs from the *hexb$^{+/+}$* samples in that the punctate pattern was lost, and the ER appears to be restricted to an area surrounding the nucleus. (**D**) It was noted that the 80d sample signified a drastic reduction in the overall immunoreactivity of GRP78 relative to the 80d *hexb$^{+/+}$* sample. Scale bar = 100um.

2. Indicators of Activation of the UPR Signal Cascades

2.1. ATF6

The UPR and ER stress is a highly complex process with multiple cascades working differentially over time to help restore homeostasis or in cases of chronic stress, induce apoptosis. After identifying the activation of ATF6 and XBP1 during the terminal stage of SD, we set to characterize expression of these markers at different ages during disease development. In *hexb*$^{+/+}$ spinal sections, ATF6 immunostaining was widespread throughout all three regions and within each region, with more intensive staining occurring in the AHNs. This pattern of staining was consistent in all *hexb*$^{+/+}$ samples across 60-, 80-, and 100-day sections (Figure 11 A,C,E). Between the three regions, the cervical and thoracic segments showed marginally more staining in comparison to the lumbar segment. The intracellular localization, specifically within the AHNs, revealed equally diffused, punctate, intense, cytosolic staining. This observed pattern indicated that inactive, ER bound ATF6 was present within the cells of *hexb*$^{+/+}$ spinal samples. On the other hand, the *hexb*$^{-/-}$ spinal sections exhibited some contrasting immunostaining that changed during disease development. A pattern indicative of ER bound, or Golgi retained ATF6 was observed within the 60-day *hexb*$^{-/-}$ spinal cords. Albeit staining intensity was notably decreased compared to the *hexb*$^{+/+}$ sections, it remained in the reticular structures within the cytosol (Figure 11 B). Interestingly, AHNs displayed enhanced levels of staining in comparison to cells within the intermediate zone and posterior horn. Upon examination of 80-day *hexb*$^{-/-}$ samples, we noted a translocation and redistribution of

ATF6 immunostaining from strictly reticular cytosolic to partially cytosolic and predominantly nuclear (Figure 11 D). Despite some staining remaining within the cytosol, the distribution of cytosolic immunolabeling changed from diffuse and punctate to clustered around the nucleus in an ER halo. Having a significant proportion of ANHs exhibiting nuclear staining acts as a conformational indicator that ATF6 has been cleaved and is translocated to nucleus. Furthermore, the staining intensity displayed an additional reduction between 80-day *hexb*$^{-/-}$ samples and age matched *hexb*$^{+/+}$ sections but also between 60-day *hexb*$^{-/-}$ and 80-day *hexb*$^{-/-}$ samples which signified that ATF6 begins to taper off in parallel with disease progression. Similarly, 100-day samples also showed a combination of ER halo and nuclear staining, with a large proportion of staining focused within AHNs (Figure 11 F). These results indicated a transient activation and translocation of ATF6 between 80 and 100 days of age. In summary, the mechanistic shift between ER associated/Golgi retained ATF6 in 60-day *hexb*$^{-/-}$ spinal cord segments to the combinatorial labeling seen in 80-day *hexb*$^{-/-}$ and 100-day *hexb*$^{-/-}$ samples highlighted the differential expression of ATF6 and, by extension, the differential activation of ER stress temporally and spatially in SD mouse model.

hexb$^{+/+}$ *hexb*$^{-/-}$
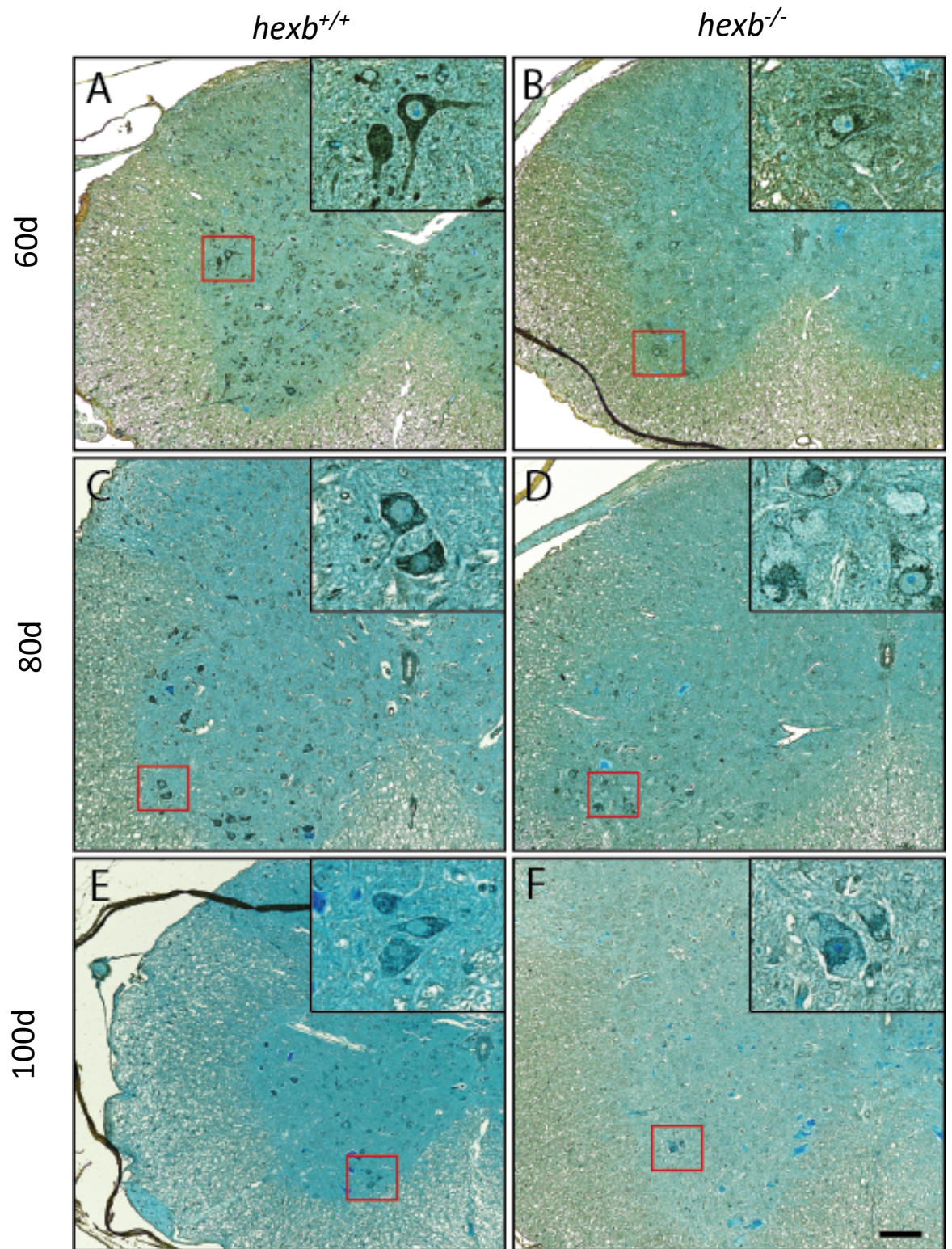
Figure 11.The localization of ATF6, an arm of the UPR, developmentally within the AHNs of the cervical spinal cord region. Immunocytochemical localization in paraffin- embedded sections of 60-, 80-, and 100-day old *hexb*$^{+/+}$ and *hexb*$^{-/-}$ mice. (**A,C,E**) The spinal cords of *hexb*$^{+/+}$ at 60, 80, and 100 days, respectively, consistently demonstrated a punctate, reticular staining pattern with intense levels of immunostaining indicating inactive and ER-bound ATF6. (**B,D,F**) In contrast, *hexb*$^{-/-}$ samples highlighted a decrease in global staining of ATF6 that started as early as 60 days. A redistribution to the nucleus that begun at 80 days and continued through disease development was also noted, with some cells still showed ER staining. The nuclear localization of ATF6 demonstrates its cleavage and subsequent translocation to the nucleus where it acts as a potent transcription factor. Scale bar = 100um.

2.2. XBP1

To extend our investigation to downstream targets of ATF6 and IRE1, we further examined the temporal and spatial expression of XBP1. Spinal cords from 60-day old *hexb*$^{+/+}$ mice revealed minimal levels of cytosolic immunoreactivity across many cell types in all three regions (Figure 12 A). A reduction in staining intensity was observed toward the posterior region of each section. The AHNs exhibited the heaviest cytosolic staining with very few cells displaying weak nuclear staining. This staining pattern indicated the presence of inactive or uncleaved XBP1 which is a direct conformation of the inactivity of IRE1. Therefore, this demonstrated a lack of ER stress and UPR activation, which was expected in wild type conditions. Similar findings were noted in the remaining 80- and 100-day *hexb*$^{+/+}$ spinal cord samples (Figure 12 C,E). In contrast, the *hexb*$^{-/-}$ mice revealed differential staining patterns, localization, and expression levels in the various ages examined. At 60-days old *hexb*$^{-/-}$ mice, all three regions of the spinal cord showed similar levels of total staining when compared to *hexb*$^{+/+}$ samples. The same dispersal pattern was also maintained in which staining decreased moving from the ventral horn to the dorsal horn. However, the AHNs showed a striking translocation of XBP1 from the cytosol into the nucleus which was not noted in the *hexb*$^{+/+}$ spinal sections (Figure 12 B). Translocation of XBP1 was also observed within cells, most prominent in the AHNs, of 80- and 100-day *hexb*$^{-/-}$ mice (Figure 12 D,F). Comparably to the 60-days sections, the 80-day *hexb*$^{-/-}$ cervical and lumbar regions showed a marginal increase in overall staining while the thoracic region exhibited a salient increase in immunoreactivity in comparison to

hexb$^{+/+}$ segments. On the contrary, at 100 days, the *hexb$^{-/-}$* spinal cord sections appeared to show a decrease in the total staining present, as well as a change in the distribution of the staining. The AHNs within the cervical region had minimal staining or were completely negative, with most nuclear labeled cells localized in the intermediate zone (Figure 12 F). Heavy nuclear staining was still observed within the AHNs of the thoracic and lumbar sections. Comparatively, the 80-day samples emerged to represent the peak of XBP1 expression and nuclear translocation throughout the spinal cord of *hexb$^{-/-}$* mice. Nuclear XBP1, which is regulated by IRE1, solidifies the role of this signaling cascade in the induction ER stress during the pathogenesis of SD.

hexb^{+/+}   *hexb*^{-/-}
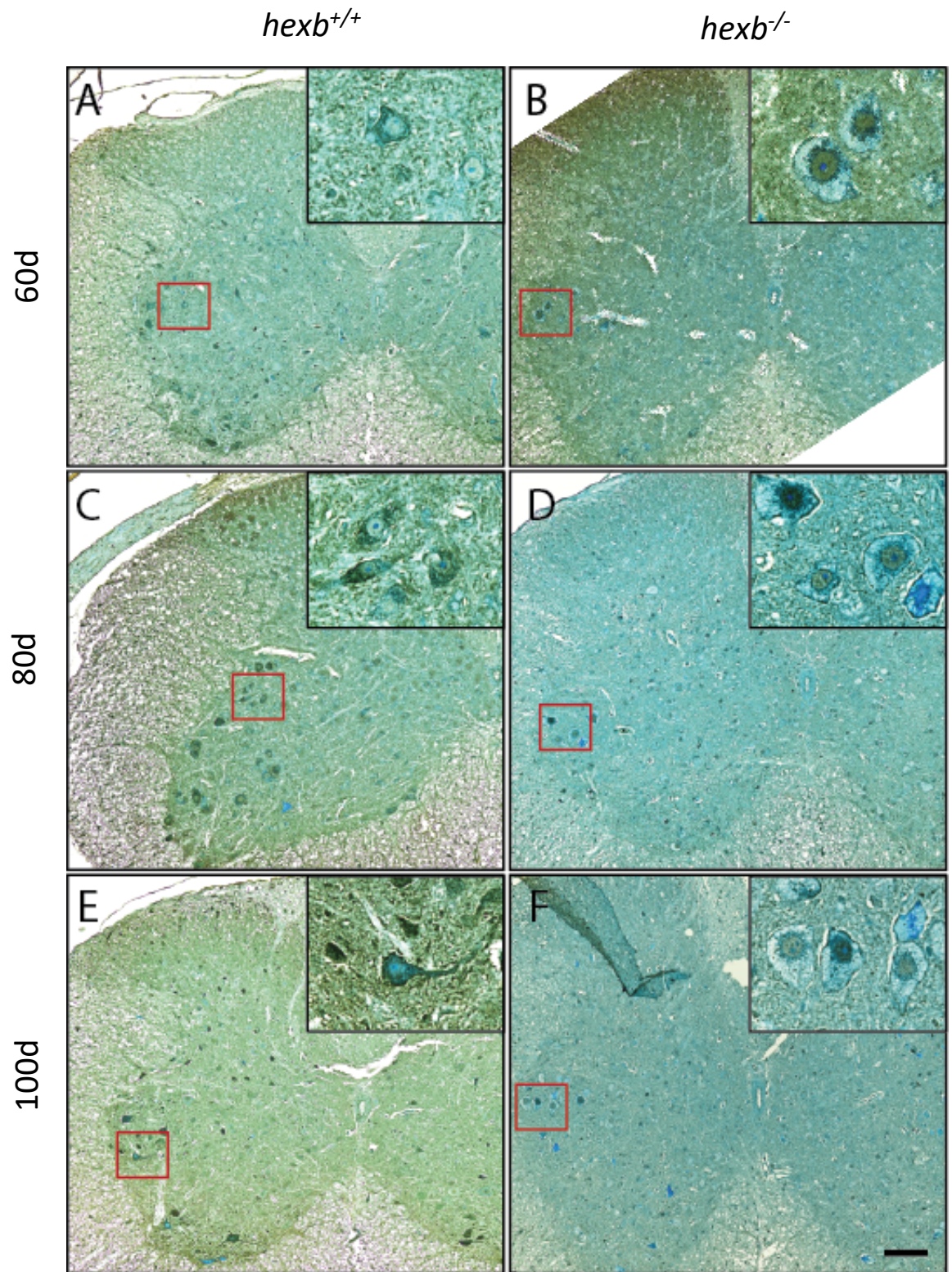
Figure 12. The immunocytochemical localization of XBP1, a downstream target of multiple UPR arms, developmentally within the cervical region of paraffin- embedded spinal cord sections from 60-, 80-, and 100-day old *hexb*$^{+/+}$ and *hexb*$^{-/-}$ mice. (**A,C,E**) The spinal cords of *hexb*$^{+/+}$ at 60, 80, and 100 days, respectively, consistently demonstrated a diffuse cytosolic staining pattern with intense levels of immunostaining indicating the presence of uncleaved XBP1, most prominent within the neurons of the anterior horn. (**B,D,F**) In contrast, *hexb*$^{-/-}$ neurons presented with a striking redistribution of XBP1 strictly to the nucleus. This localization began at 60 days (**B**) and persisted through to 100 days (**F**). This nuclear localization demonstrates XBP1 is being cleaved by IRE1 and is now able to translocate to the nucleus where it acts as a potent transcription factor, which denotes ER stress activation. Scale bar = 100um.

3. Chronic Stress and Neuronal Apoptosis

The identification of activated ER stress markers such as ATF6 and XBP1 as early as 60 days within the spinal cords of *hexb*$^{-/-}$ mice posed the question whether neuronal apoptosis occurs much earlier than the expected end point of 120 days of age. We therefore evaluated the expression and localization of CHOP, a pro-apoptotic transcription factor, and two markers of apoptosis: cleaved PARP, and cleaved caspase 7.

3.1 CHOP

CHOP is a key regulator in cell fate determination as it plays a vital role in the apoptotic decision of the cells. Cytosolic immunostaining of CHOP, predominantly within AHNs, was observed in all three regions of *hexb*$^{+/+}$ spinal sections, with most other cell types void of CHOP immunoreactivity (Figure 13 A,C,E). CHOP is ubiquitously expressed at low levels and therefore cytosolic expression was expected under homeostatic conditions. This localization pattern was seen consistently between regions but also across all three ages of *hexb*$^{+/+}$ mice. In contrast, *hexb*$^{-/-}$ spinal sections demonstrated a striking translocalization of CHOP to the nucleus. Interestingly, at 60 days several AHNs were already exhibiting nuclear staining ranging from light to quite intense and upon further evaluation, focals were noted in several of the stained nuclei (Figure 13 B). Global immunoreactivity levels within each spinal cord region were marginally less to that of the *hexb*$^{+/+}$ sections and were comparable between the segments. Similarly, 80-day *hexb*$^{-/-}$ spinal sections demonstrated a clear nuclear localization of CHOP with conspicuous intra-nuclear punctate staining (Figure 13 D). By 100 days, the AHNs showed clear

95

morphological characteristics of lipid accumulation and distress. This was accompanied by nuclear immunostaining of CHOP, as seen in earlier ages (Figure 13 F). Immunoreactivity was more concentrated within the anterior and posterior horns, with lesser amounts in the intermediate zone. Interregional differences were also apparent, as the cervical and thoracic regions appeared to exhibit lower numbers of CHOP positive AHNs, suggesting a peak in CHOP activation around 80 days of age, while the lumbar region maintained dominant staining in the AHNs. To further elucidate the differences in CHOP expression and localization temporally between $hexb^{+/+}$ and $hexb^{-/-}$ mice, we quantified the number of nuclear CHOP positive cells within the anterior horn of spinal cord samples. This was completed by counting the total number of cells within a defined area of the anterior horn of the cervical, thoracic, and lumbar regions, that presented with strictly nuclear CHOP staining. Three independent sets of spinal cords were evaluated and the numbers were standardized as cells/mm^2. Within the cervical segment across all ages, there was a clear increase in the number of nuclear CHOP positive cells located within the anterior horn of $hexb^{-/-}$ spinal cords compared to $hexb^{+/+}$, with significant changes noted at 80 and 120 days (Figure 4 D). The peak of CHOP activation in this region was noted at 80 days, while all other ages showed similar numbers between $hexb^{-/-}$ samples. The thoracic region only showed a slight variation in the activation pattern of CHOP in that all ages showed comparatively similar numbers between $hexb^{-/-}$ sections but exhibited significant differences between $hexb^{+/+}$ and $hexb^{-/-}$ samples (Figure 4 E). Finally, the lumbar section revealed similar overall numbers of cells displaying nuclear CHOP between

hexb$^{-/-}$ mice but again demonstrated significant increases across all ages between *hexb*$^{+/+}$ and *hexb*$^{-/-}$ samples (Figure 4 F). However, a peak point of CHOP activation within the SD lumbar sections appeared at 100 days of age. At endpoint (120d), all three regions had a significant increase in the number of nuclear CHOP positive cells (Figure 4 D-F). More specifically, the thoracic and lumbar regions of the *hexb*$^{-/-}$ spinal cord presented with the most dramatic increase, while the cervical section showed a marginally lower increase in comparison.
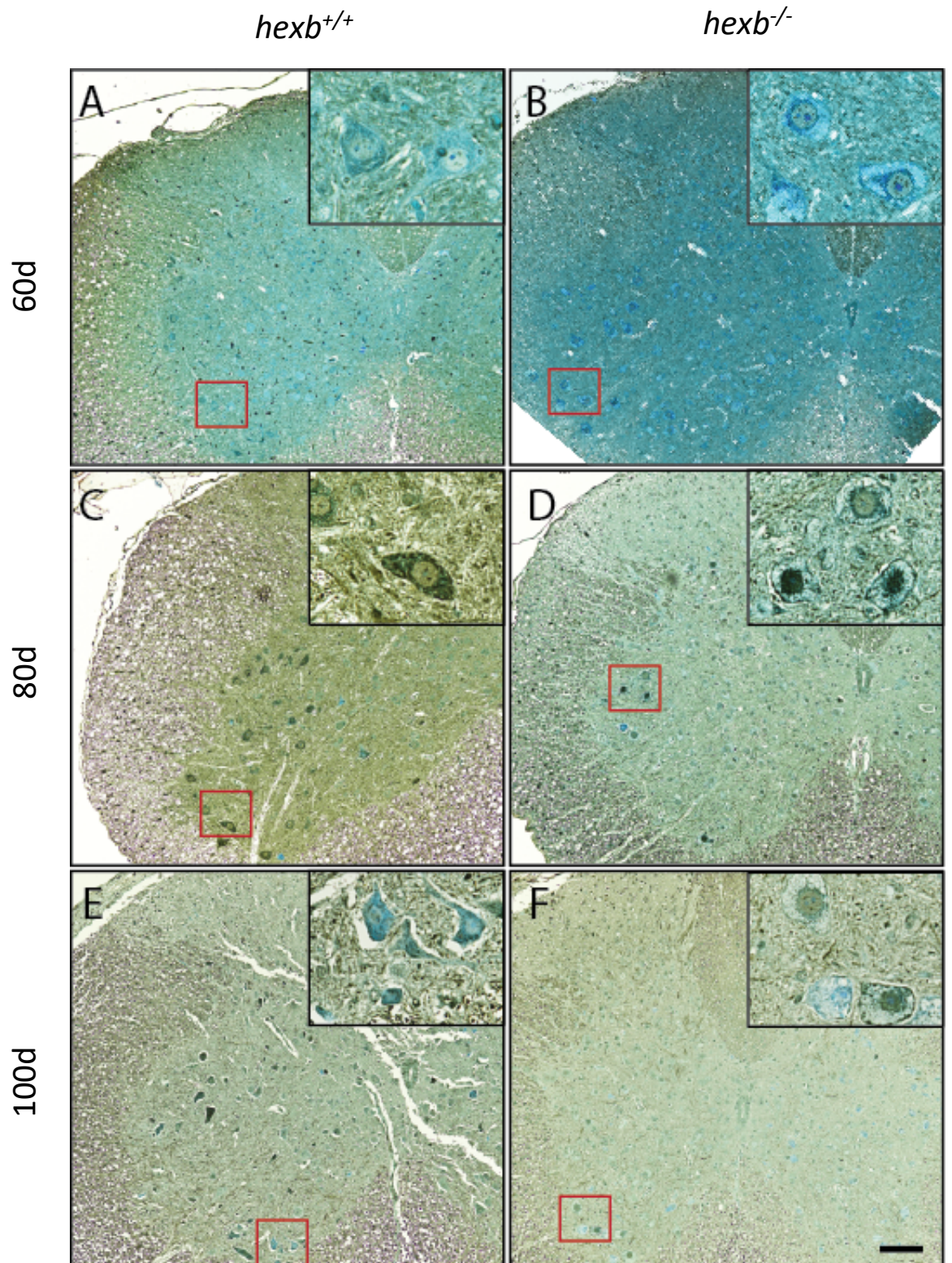
Figure 13. The localization of CHOP, a pro-apoptotic factor, developmentally within the cervical spinal cord region of 60-, 80-, and 100-day old *hexb$^{+/+}$* and *hexb$^{-/-}$* mice. Immunocytochemical localization in paraffin- embedded sections of *hexb$^{+/+}$* and *hexb$^{-/-}$* mouse spinal cords of CHOP specifically among the population of anterior horn motor neurons. (**A,C,E**) The spinal cords of *hexb$^{+/+}$* mice at 60, 80, and 100 days, respectively, consistently exhibited an intense, diffuse cytosolic staining pattern indicating the presence of inactive CHOP. (**B,D,F**) In contrast, *hexb$^{-/-}$* neurons presented with a striking redistribution of CHOP strictly to the nucleus. This nuclear localization of CHOP, which begins as early as 60 days (**B**) and progresses with disease development, shows that ER stress is chronic early in disease pathogenesis and an apoptotic cell fate has been determined. Scale bar = 100um.

3.2. Cleaved Caspase 7 and Cleaved PARP

Previously identifying activation of two vital potentiators of ER stress at terminal stages of SD led us to evaluate the intracellular localization of these apoptotic markers temporally in the spinal cords of *hexb*$^{+/+}$ and *hexb*$^{-/-}$, to determine a timeline of the mass neuronal death known to be associated with SD pathology. Within wildtype *hexb*$^{+/+}$ sections, the vast majority of AHNs were negative for c-Cas7 immunoreactivity (Figure 14 A,C,E). This was true across all ages, with the most notable cytosolic staining at 100 days. Conversely, the *hexb*$^{-/-}$ spinal cord segments demonstrated clear nuclear localization of c-Cas7, which is an indication of its activation. Within the 60-day SD spinal cords, we observed AHNs and other neurons clearly expressing nuclear c-Cas7 (Figure 14 B). This staining pattern persisted at 80 and 100 days, but a small pool of AHNs which were negative for staining were also observed (Figure 14 D,F). Throughout the pathogenesis of the disease, a decrease in the total immunostaining of c-Cas7 within each region of SD mice was noted. Marginal variations began at 80 days and were followed by a continual decline throughout 100 days of age and into the terminal stages of the disease, as previously mentioned. Although a decrease was seen in total staining of c-Cas7 among *hexb*$^{-/-}$ spinal cords, the differences in the presence of nuclear c-Cas7 between *hexb*$^{+/+}$ and *hexb*$^{-/-}$ samples of all ages were very clear and statistically significant. To further elucidate the differences in c-Cas7 expression and its variation in localization temporally between *hexb*$^{+/+}$ and *hexb*$^{-/-}$ mice, we quantified the number of nuclear c-Cas7 positive cells within the anterior horn of spinal cord samples. Within the cervical, thoracic, and lumbar regions,

a predefined area of the anterior horn was established and the total number of cells that

presented with strictly nuclear c-Cas7 staining were counted (Figure 4 G-I). Three

independent sets of spinal cords were evaluated, and the numbers were standardized as

cells/mm^2. Consistent trends in the amount of nuclear c-Cas7 positive cells present were

seen across all three regions of *hexb$^{-/-}$* spinal cords. Interestingly, the peak of c-Cas7 was

seen at 60 days, which is far earlier than previously hypothesized, and this was true for all

three regions. Subsequent deterioration of activated c-Cas7 cell numbers was seen in a

stepwise manner throughout the remainder of the ages. Levels in the cervical region at

60 and 80 days were significantly higher in *hexb$^{-/-}$* samples in comparison to *hexb$^{+/+}$*

sections, while variations at 100 and 120 were not. This finding remained consistent for

both the thoracic and lumbar sections and parallels the mass neuronal loss seen at the

later ages. These observations clearly demonstrate the immense activation of c-Cas7 early

during disease progression and provides evidence that this mechanism of apoptosis

occurs much earlier than expected leading toward the neuronal degeneration that is

prominent in the SD mouse model.

One of the many roles of c-Cas7 is to cleave PARP, a potent inducer of apoptosis,

which confirms a fate of death for the cell. Therefore, with evidence demonstrating the

activation of c-Cas7 during SD pathogenesis, we anticipated the subsequent induction of

down-stream apoptotic factors such as cleaved PARP. In wildtype *hexb$^{+/+}$* spinal cord

segments, minimal immunoreactivity toward cleaved PARP was observed with very few

cells showing cytosolic staining (Figure 15 A,C,E). This pattern of immunolabeling was

consistent among the different regions of the spinal cord. Interestingly, *hexb*^-/- spinal

sections demonstrated increased nuclear staining of cleaved PARP. Nuclear localization of

PARP, albeit at minimal levels, was noted as early as 60 days in *hexb*^-/- samples, where a

regional specific presentation of nuclear staining was observed (Figure 15 B). Cervical

segments presented minimal staining in total but contained some nuclear labelled AHNs.

Conversely, thoracic and lumbar regions also contained multiple AHNs with clear nuclear

staining, but the global staining of these regions was augmented in comparison to cervical

sections. As SD progressed and accumulations were exacerbated, a sharp increase in

cleaved PARP total staining was seen within 80-day *hexb*^-/- samples (Figure 15 D).

Interregionally, the staining appeared most abundant within the lumbar segment and

more modest in the cervical and thoracic regions. Nuclear staining was also more

dispersed throughout the entirety of the lumbar and thoracic sections, differing from

cervical which seemed to have much of its staining in the anterior horn, specifically within

the AHNs. When evaluated intracellularly, the nuclear abundance of cleaved PARP

amongst AHNs was striking. At 100 days *hexb*^-/- samples showed a drastic decrease of

cleaved PARP immunoreactivity which was concurrent with the observed decrease in c-

Cas7 (Figure 15 F).

Our results indicate that the activation of c-Cas7, leading to the cleavage of PARP

and the induction of apoptosis, peaks at 60 days of age and tapers off as the SD mouse

approaches end point at 120d of age. In parallel, cleaved PARP showed a similar pattern

of decrease overtime but its peak appeared to be at 80 days. Therefore, the conception

of this intense activation of two factors which are vital for apoptotic events, indicates that

neuronal apoptosis is occurring in the spinal cord at high frequencies as early as 60 days

of age in mouse models of SD.

$hexb^{+/+}$ $hexb^{-/-}$

60d

80d
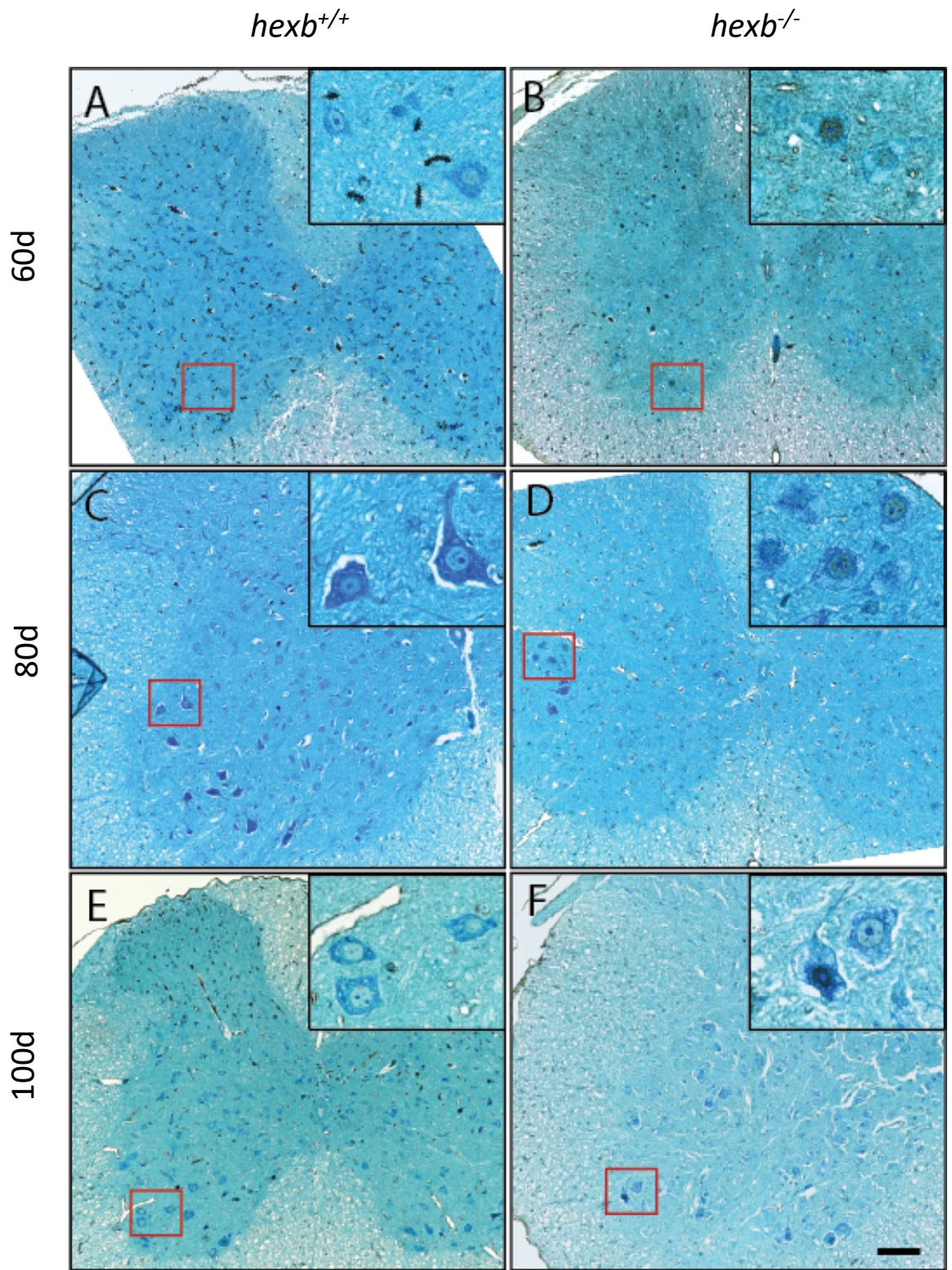
100d

Figure 14. The immunocytochemical localization of cleaved caspase 7 (c-Cas7), an executioner caspase known to be a marker of cellular apoptosis, developmentally within the cervical spinal cord region of 60-, 80-, and 100-day old *hexb*$^{+/+}$ and *hexb*$^{-/-}$ mice, specifically among the population of anterior horn motor neurons. (**A,C,E**) The spinal cords of *hexb*$^{+/+}$ at 60, 80, and 100 days, respectively, appeared to be negative for c-Cas7 staining. However, there were a few cells which presented with weak nuclear staining and other cells, noticeably at 100 days (**E**) which showed cytosolic staining. (**B,D,F**) The *hexb*$^{-/-}$ neurons showed opposing trends in which a salient redistribution of c-Cas7 to the nucleus was observed. This nuclear localization of c-Cas7, was most intense in 80-day anterior horn neurons (**D**) but was present throughout disease development. This highlights a mechanistic pathway of apoptosis which can result in the hallmark neurodegeneration seen in SD. Scale bar = 100um.

hexb$^{+/+}$ *hexb$^{-/-}$*
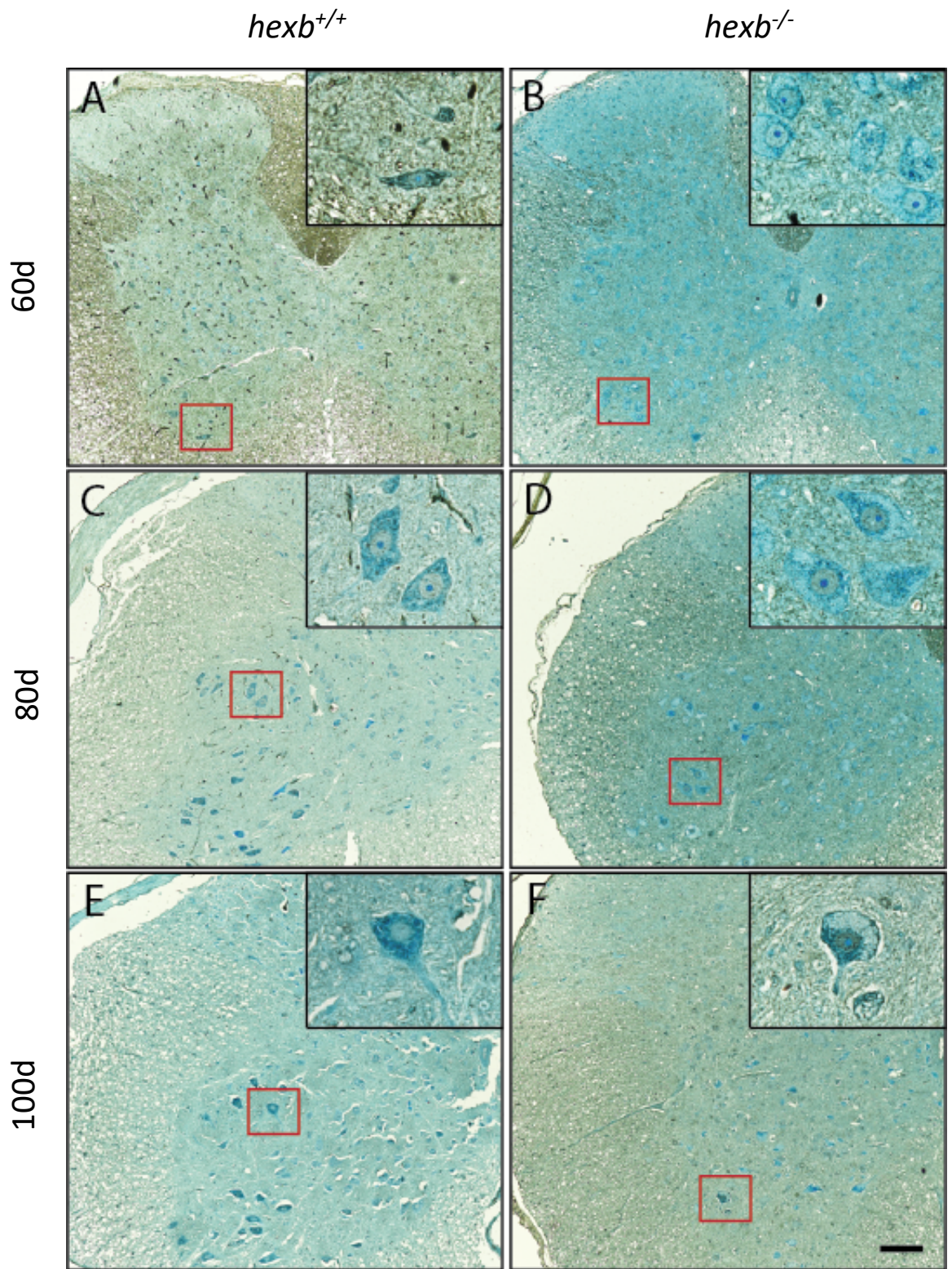
Figure 15. The immunocytochemical localization of cleaved PARP, a known marker of apoptosis, developmentally within the cervical spinal cord region of 60-, 80-, and 100-day old *hexb*$^{+/+}$ and *hexb*$^{-/-}$ mice, specifically among anterior horn motor neurons. (**A,C,E**) The spinal cords of *hexb*$^{+/+}$ at 60, 80, and 100 days, respectively, showed immunoreactivity of cleaved PARP, with select cells demonstrating weak cytosolic staining (**B,D,F**) The *hexb*$^{-/-}$ neurons however, presented with a prominent translocation of cleaved PARP to the nucleus. This nuclear localization of cleaved PARP began as early as 60 days (**B**) albeit staining was weak and continued to intensify as the disease worsened over time (**D,F**). This highlights a novel pathway of apoptosis execution which consequentially contributes to the hallmark neurodegeneration seen in SD. Scale bar = 100um.

CHAPTER FOUR

DISCUSSION

The spinal cord contributes to all vital physiological functions including movement, breathing, and sensory processing [58, 59]. A hallmark of GM2 gangliosidosis is massive substrate accumulation within lysosomes of neurons throughout the CNS, particularly the spinal cord. Lysosomal lipid accumulation is histologically prominent within the spinal anterior horn motor neurons of *hexb*-/- mice [54]. This lysosomal accumulation can trigger a wide range of consequences within neurons including lysosomal rupture, ER stress induction, and Ca^{2+} dysregulation with consequences seen throughout the spinal cord, which shows mass amounts of neuronal death. At the terminal stages of the disease, lysosomal storage disrupts the spinal cord cytology and functions. Our results demonstrate that *hexb*-/- AHNs showed extensive lipid accumulations leading to lysosomal enlargement and overall swelling of the neuron. Here we reported a drastic increase in the size of these anterior horn neuronal cell bodies by 100 and 120 days in *hexb*-/- spinal cord samples. This lysosomal induced swelling leads to alterations of the intracellular location of the ER, as well as other organelles. This additional disturbance of the ER may potentially exacerbate the overall negative impact this disease has on neuronal survival. The location of affected neurons within the CNS is critical and although neuronal loss is gradual, the overall reduction in AHN numbers within the spinal cord is expected to have a severe impact on motor neuronal circuitry and motoneuronal function. Circuitry loss may occur in a sequential manner, but further investigation is required to fully uncover

this pathological process. We also observed ~50% reduction in *hexb*^{-/-} AHN abundance throughout the entirety of the spinal cord by the terminal stage of the disease (120 days). These morphological changes in combination with the loss of AHNs in *hexb*^{-/-} mice parallels the phenotypic onset observed around 100 days. Initial symptoms include impairment of motor function involving balance and coordination defects which are directly related to AHNs and their normal functioning. As accumulations worsen and depletion of AHNs continues, these symptoms quickly escalate into severe muscle wasting, limited ability to move limbs, and extreme tremors and shortly after the mice succumb to the detrimental consequences of this lipid storage and neuronal loss. Similar trends have been clinically reported in patients with late-onset TSD and SD. Late on-set SD has been described as showing strong similarities in symptomology to that seen in lower motor neuron disease. Examination of these patients reveals distended neurons and widespread denervation within the anterior horn of the spinal cord. Several clinical reports have also highlighted the marked neuronal loss that occurs during disease pathogenesis within the anterior horn of the spinal cord specifically [51]. The location of neuronal loss functionally correlates to the phenotypic outcome seen in these patients, which is gait disturbances, severe muscle weakness, muscle atrophy, fasciculations, and tremors [43]. Although a highly reported phenomenon, the exact mechanism of how the initial insult of accumulation in GM2 gangloisidoses leads to the stark depletion of AHNs remains unknown. The results from our study may help provide a further understanding of disease pathogenesis and progression.

In GM2 gangliosidoses, the connection between lipid accumulation within lysosomes and neuronal cell death, which translates into the clinical outcome seen in patients, is still not completely understood. Our examination of ER stress markers provides a potential pathway connecting the enzymatic deficiency and lysosomal storage to an apoptotic outcome. The results highlighted a multitude of ER stress markers that are differentially upregulated temporally throughout the regions of the spinal cord. They also uncovered great diversity in the inter-regional localization patterns, striking changes in cellular localization, neuronal cell loss, morphological changes, and apoptosis (Figure 16).
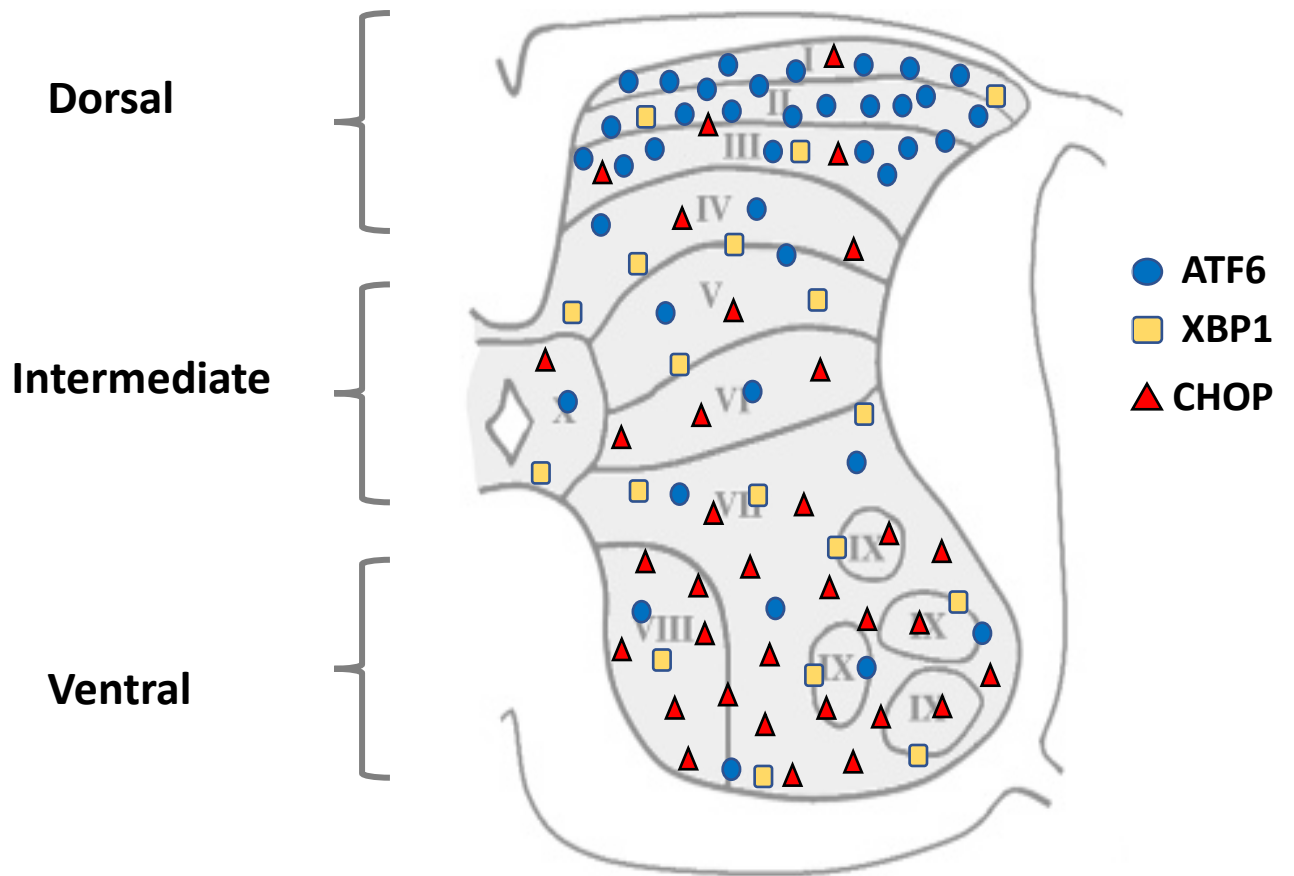
Figure 16. A summary of ATF6, XBP1, and CHOP intraregional immunoreactivity in the spinal cord of 120-day *hexb*$^{-/-}$ mice. ATF6, represented by blue circles, accumulates more within the dorsal horn region of the spinal cord, intermediate accumulation in the anterior horn and lowest detection within the intermediate column. CHOP, represented by red triangles, shows an inverse spatial relationship compared to ATF6 in that its strongest accumulation was within the AHNs and lower immunoreactivity in the dorsal horn and intermediate column. Lastly, XBP1, represented by yellow squares, showed little locational specification, and instead demonstrated dispersed staining throughout the entirety of all regions.

The ER has been at the center of several studies which attempted to highlight a mechanistic pathway within several lysosomal storage disorders. Pelled and colleges (2003) examined the implications of GM2 accumulation in neuronal tissue collected from *hexb*^{-/-} mice. They were able to identify a causal relationship between the intercellular accumulation of GM2 and rates of Ca^{2+} uptake via the sarco/endoplasmic reticulum Ca^{2+} ATPase (SERCA). In microsomes collected from *hexb*^{-/-} mouse brains, there was a severely diminished Ca^{2+} uptake via SERCA into the ER [66]. Depleting internal ER Ca^{2+} stores, which disrupts Ca^{2+} homeostasis, is highly likely to induce ER stress. In addition, Virgolini et al, also suggested that a depletion of ER Ca^{2+} stores and activation of PERK can be caused by GM2 accumulation within neurons [105]. Although these results appear to support the notion of involvement of ER stress after GM2 accumulation, the study used cell culture of cell lines that were differentiated and then exposed to high concentrations (2μM) of exogenous GM2 in an attempted to mimic substrate accumulation through the addition of GM2 gangliosides in culture media [105]. This does not accurately represent the accumulation that accompanies the enzymatic deficiency within GM2 gangliosidoses. Gangliosides can also cluster at the cell membrane where they are capable of interacting with membrane proteins to modulate a variety of cellular functions such as cell-cell recognition, phenotypic changes, cell growth, and signal transduction [129, 130]. When ganglioside levels are altered, it can lead to reduced membrane fluidity which negatively impacts the cell and generates cellular dysfunction [131]. In Virgolini's study, the addition of GM2 exogenously creates an alteration in ganglioside levels and may result in cellular

stress independent of substrate accumulation. This approach causes additional accumulation, independent of β-hexosaminidase deficiency associated with SD. The study failed to account for significant physiological differences between cell cultures and primary neurons from SD models. Therefore, despite the promising results suggesting ER stress involvement, the relevance of these findings is brought into question due to the improper representation of the substrate accumulation that is central to the disease.

Similar studies have been conducted where primary neurons were isolated from a different lysosomal storage mouse model to evaluate the effects of substrate accumulation. The D'azzo group released a study where they determined that through GM1 accumulation in spinal neurons from *β-galactosidase* knockout, ER Ca^{2+} was disrupted because of buildup of gangliosides within the ER [90]. They also reported upregulation of CHOP within these neurons which coincided with severe neuropathological symptoms and neuronal loss. Despite the focus of this paper being GM1 gangliosidosis, this research provides strong evidence for ER stress involvement when ganglioside accumulation occurs within neurons. Our current findings concur with these results meaning we also found strong indicators for ER stress activation following GM2 accumulation within AHNs of *hexb$^{-/-}$* mice. A separate study by Kobolak and colleagues utilized a disease-specific induced pluripotent stem cell (iPSC) line representative of mucopolysaccharidosis II (MPS II) to evaluate disease related neuropathy [112]. These cells were differentiated into neuronal progenitor cells (NPCs) and then terminally differentiated towards cortical neurons. Although this study didn't

specifically assess the role of ER stress, they were able to identify an increase in expression of cleaved caspase 7, an executioner for apoptotic events, within the diseased cell line when compared to the control [112]. Therefore, this provided evidence of increased apoptotic activity occurring within neurons of LSD patients. Incidentally, there are several studies that reported c-Cas7 upregulation in ALS patients which could be used to extrapolate a potential common mediator of LMN disease symptoms seen between these disorders [132, 133].

Current evidence highlights the potential role of ER stress, due to ganglioside accumulation or Ca^{2+} dysregulation, in neurodegenerative lysosomal storage diseases, but fails to identify a connecting mechanism of how apoptosis occurs. Our results document multiple activated UPR markers which are potential mediators of apoptosis. We identified early induction of UPR related factors, ATF6 and XBP1, as early as 60 days. It was also noted that ATF6 was retained within the ER/Golgi at 60 days but by 80 days demonstrated a translocation to the nucleus and a subsequent decrease in its overall expression. GRP78 also exhibited variations in its intracellular localization and expression patterns, with what appeared to be a reduction in overall expression and relocalization to the cell surface occurring between 60 and 80 days. In addition, we also successfully identified CHOP, cleaved caspase 7, and cleaved PARP as potential mediators of neuronal death. All three of these factors were clearly activated starting at 60 days and had peaks ranging between 60 and 100 days, which aligned with the most intense levels of neuronal loss we observed. Collectively, the subsequent activation of each of these markers and their peaks parallels

the initial symptom onset period of 80-100 days seen in $hexb^{-/-}$ mice. At 100 days, our

findings showed an initial decrease in neuron numbers which was succeeded by significant

activation of both CHOP and c-Cas7 which ultimately intersects with when mice begin to

display muscle weakness, tremors, and coordination defects. This indicates these factors

are playing a significant role in neurodegeneration and at 100 days or slightly prior, there

is an accelerated rate of apoptotic events.   Further examination of their full involvement

in the process of neuronal death will be required. These findings are novel and are more

specific than previous studies due to its intricate evaluation of a highly specific and

affected group of neurons. By evaluating the spinal cord spatially and temporally, we

demonstrated both neuronal morphological variations and neuronal loss, as well as an

induction of multiple mechanistic pathways that connect ER stress activation with

mediators of apoptosis. Additionally, our results highlight the early stimulation of these

factors at 60 days of age, which is much earlier than expected. Taken together, this

research provided possible therapeutic targets which could be targeted through a variety

of techniques including genetically, siRNA, pharmacologically, and using chaperones but

it also emphasized the importance of early therapeutic intervention.

SD and TSD, while differing in enzymatic deficiencies, present with virtually identical

phenotypes in humans. The $hexb^{-/-}$ mouse model not only accurately mirrors the

progression of SD but is also representative of TSD seen in humans. Our results therefore

may also be highly relevant to the more common Tay Sachs disease. There may be

possibilities to further extend these discoveries to various types of lysosomal storage

diseases seeing as current literature indicates similarities between mechanisms of disease. Moreover, as previously mentioned, late-onset SD frequently gets misdiagnosed as ALS or other lower motor neuron diseases which suggests that these findings might be applicable to those diseases as well. Overall, the relevancy of these results may extend far beyond the current disease of interest which would allow for significant advances in the mechanistic unravelling of several detrimental diseases and therapeutic innovations.

Many UPR factors can play multiple roles throughout the initiation and subsequent activation of downstream cascades depending on a multitude of factors, such as the length and intensity of ER stress as well as cell type [17]. One of the factors whose net outcome on the cell is still being debated is ATF6. The role of ATF6 is still not completely understood but most research surrounding it has delved into its role as a pro-survival factor. ATF6 has been observed exhibiting a pro-survival role in response to chronic, yet mild ER stress [134]. Other studies have demonstrated its vital protective role through targeted downregulation of ATF6 which resulted in increased melanoma cellular sensitivity to ER stress inducers, thapsigargin and tunicamycin [134, 135]. The literature reports ATF6 as a pro-survival factor that works to counteract ER stress activation by upregulating ER chaperones, such as GRP78, and XBP1 to improve the efficiency of protesostasis [20]. Contrastingly, some studies have also highlighted the roles of ATF6 in the apoptotic events induced by ER stress. In vascular endothelial cells, high expression of activated ATF6 was observed to exacerbate ER stress-induced apoptosis [17]. Conversely, ATF6 has been shown to activate and up-regulate the expression of a multitude of

apoptosis invoking factors, such as CHOP and cleaved caspase 9, but it can also trigger inflammation through induction of the NF-kB pathway [17, 136, 137]. Ultimately, our current results question the true role of ATF6 in SD and which cascade it activates, pro-survival or pro-apoptotic. At 60 days we observed a retention of ATF6 within the ER/ Golgi of $hexb^{-/-}$ AHNs, which suggests incomplete activation of ATF6. ATF6 at 60 days also demonstrated marginally reduced levels of expression in comparison to the $hexb^{+/+}$ samples. In sharp contrast, at 80 days we observed a further reduction in overall expression, as well as cells exhibiting nuclear localization. Some neurons still had ER staining which is due to the transient nature of ATF6 as it gets made, cleaved, and translocated. The nuclear localization however indicates that ATF6 has been fully processed by S1P and S2P in the Golgi allowing for localization to the nucleus where it can act as a potent transcription factor. Once in the nucleus ATF6 can lead to the expression of CHOP, a proapoptotic factor. In support of this idea, levels of nuclear CHOP positive cells peaked at 80 days succeeding the relocalization of ATF6. This suggests that in the case of SD progression, ATF6 appears to be contributing to the induction of cell death. We also noted consecutive downregulation of GRP78 at 80 days. Therefore, it could be postulated that GRP78 may play a role in the retention of ATF6 to the ER at 60 days. Other potential mediators of ATF6 retention are S1P and S2P, with S2P being necessary for complete cleavage of the ATF6. Thus, the evaluation of the expression levels and activation of both site-specific proteases as well as the relationship between GRP78 and ATF6 at 60 days should be conducted in future studies. Additionally, our research suggests

a potential mechanistic pathway connecting ATF6 and the execution of neurons through apoptosis. Observing that ATF6 and c-Cas7 are activated early within disease development allows for the postulation of an apoptotic cascade. ATF6 has been shown to activate cleaved caspase 9 which modulates the activation of c-Cas7 which then develops the ability to cleave PARP, ultimately resulting in cell death [17, 110, 138]. Although the relationship isn't completely defined, c-Cas7 activation and ATF6 activation seen in SD provide a potential mechanistic pathway connecting ER stress to neurodegeneration. Overall, these results emphasize key markers of ER stress and apoptosis that could be evaluated as therapeutic targets in future studies.

Interestingly, our results also indicated a highly specific localization pattern and expression levels of GRP78. It has been highly recognized that GRP78 becomes upregulated during ER stress through means of all three arms of the UPR and functions as an ER chaperone protein to help reduce the load of unfolded proteins accumulating within the ER [20, 137, 139]. Our results suggest differential GRP78 expression accompanied by localization to the cell membrane. Within the spinal cords of SD mice, we observed neurons exhibiting localization of GRP78 to the cell membrane. This redistribution isn't a novel finding in that there have been multiple reports of GRP78 sequestration at the cell surface, which is actively promoted by ER stress, where it functions to regulate processes such as proliferation, inflammation, and apoptosis [15, 140]. What is novel is the relationship between localization and SD pathogenesis and its initiation early in disease progression. Some studies propose this confers a protective response leading to a

decrease in ER stress and neurodegeneration while others report a potential connection

to apoptosis [17, 20, 141]. Another interesting aspect of our results is the apparent

decrease in GRP78 expression in $hexb^{-/-}$ spinal cord samples throughout disease

advancement in comparison to $hexb^{+/+}$ samples. Although this could be due to the drastic

change in intracellular localization because of ER stress activation and disruptions in

cellular morphology, a consequence of lysosomal accumulation, this variation has the

potential to result in induction of proapoptotic cascades involving various caspases. Of

particular interest, it has been observed that increased expression of GRP78 promoted by

ER stress, is capable of binding to caspase 7, suppressing its activation [15, 142]. The

expression levels and cellular localization we noted could provide evidence of a potential

secondary apoptotic cascade. Along the same lines, downregulation of GRP78 has been

correlated with an increase in the expression of multiple caspases, including caspase 7

[143]. Within our model it could be suggested that a down regulation in GRP78 during SD

and its subsequent redistribution throughout the cell and to the cell membrane could

result in a diminished ability to bind caspase 7 therefore allowing for activation and

initiation of caspase 7's apoptotic cascade. Our research provides data which supports

this notion in that we saw a reduction of GRP78 immunohistological expression in $hexb^{-/-}$

samples beginning at 60 days. This tapering aligns with the peak of nuclear c-Cas7 positive

cells in the anterior horn of $hexb^{-/-}$ samples. However, there are other potential

mechanisms that could result in the consequential activation of caspase 7, independent

of ER stress factors [110]. Further research to elucidate the relationship between GRP78

and caspase 7 and the functional consequences of GRP78 cell membrane localization in SD needs to be conducted.

The uncovering of mechanistic pathways involved in SD development and advancement provide promising data identifying many factors as potential therapeutic targets. The next step to further evaluate these pathways and their relationship with SD would be to utilize *in vitro* techniques. First, iPSC's from SD and TSD patients could be isolated and directed towards neuronal differentiation. Importantly, this creates a highly specific cellular model for the disease of interest which harbours the naturally occurring mutations making this a vital tool for the study of the pathological storage seen in many LSDs. From here a variety of chemical chaperones, including tauroursodeoxycholic (TUDCA), trimethylamine-N-oxide (TMAO), and 4-phenylbutyric acid (4-PBA), which work to increase protein folding capacity or increase efficiency and function of the ER, could be used to treat cells. This would help illuminate effective therapeutic options for these detrimental disorders. Findings from *in vitro* models could further be extended into *in vivo* models to fully elucidate their impact on disease progression.

Further studies using double knockout (DKO) mouse models may help us determine the role of several factors that contribute significantly to the neurodegenerative processes in the disease. Since we have established that caspase 7 is intricately involved in the molecular mechanisms of SD pathogenesis, caspase 7 knockout mice which present with a normal phenotype, could be an ideal model for the generation of a DKO of *Cas7$^{-/-}$ hexb$^{-/-}$* mice. Another possibility is the generation of a *chop$^{-/-}$ hexb$^{-/-}$*

mouse, in hopes of preventing apoptosis initiation and subsequent neuronal loss. Both DKO mouse models could shed significant light on the roles of the Cas7 and CHOP during SD progression.

CONCLUSION

In summary, our research was able to highlight significant changes in morphological features of anterior horn neurons as well as severe neuronal loss of ~50% in the spinal cord by the terminal stages of SD in *hexb*$^{-/-}$ mice. We also established differential immunohistochemical localization and expression of ATF6, XBP1, GRP78, CHOP, c-Cas7 and cleaved PARP between *hexb*$^{-/-}$ and *hexb*$^{+/+}$ spinal cord sections. While factors such as ATF6 and GRP78 appeared to taper off temporally in comparison to the expression observed in *hexb*$^{+/+}$ samples, c-Cas7 and CHOP showed irrefutable upregulation, with their peak expression occurring between 60 and 80 days. We also provided evidence demonstrating that ER stress induction and apoptotic events occur considerably earlier in the timeline of SD progression, around 80 days, compared to the original prediction of onset between 100 – 120 days. The ER is emerging as a vital regulator of cell fate and apoptosis, and these findings present ER stress and the UPR, as well as subsequent activation of potent inducers of apoptosis, as novel mechanistic pathways involved in SD pathogenesis.

Studies have noted underlying similarities between SD and other neurodegenerative diseases such as ALS and spinal muscular atrophy [41, 43, 47, 48, 51]. Therefore, our observations could be extended to these other neurodegenerative

disorders, where motor neuron loss is highly significant. Overall, our study highlights ER

stress, the UPR, and the consequential apoptosis, as a pathway of interest and as a

therapeutic target and treatment for SD.

REFERENCES

1.   Schwarz, D.S. and M.D. Blower, *The endoplasmic reticulum: structure, function and response to cellular signaling.* Cell Mol Life Sci, 2016. **73**(1): p. 79-94.

2.   Metcalf, M.G., et al., *Beyond the cell factory: Homeostatic regulation of and by the UPR.* Sci Adv, 2020. **6**(29): p. eabb9614.

3.   Lu, M., et al., *The structure and global distribution of the endoplasmic reticulum network are actively regulated by lysosomes.* Sci Adv, 2020. **6**(51).

4.   Phillips, M.J. and G.K. Voeltz, *Structure and function of ER membrane contact sites with other organelles.* Nat Rev Mol Cell Biol, 2016. **17**(2): p. 69-82.

5.   Giamogante, F., et al., *ER-Mitochondria Contact Sites Reporters: Strengths and Weaknesses of the Available Approaches.* Int J Mol Sci, 2020. **21**(21).

6.   Annunziata, I. and A. d'Azzo, *Interorganellar membrane microdomains: dynamic platforms in the control of calcium signaling and apoptosis.* Cells, 2013. **2**(3): p. 574-90.

7.   Burgoyne, T., S. Patel, and E.R. Eden, *Calcium signaling at ER membrane contact sites.* Biochim Biophys Acta, 2015. **1853**(9): p. 2012-7.

8.   Scorrano, L., et al., *Coming together to define membrane contact sites.* Nat Commun, 2019. **10**(1): p. 1287.

9.   Wu, H., P. Carvalho, and G.K. Voeltz, *Here, there, and everywhere: The importance of ER membrane contact sites.* Science, 2018. **361**(6401).

10.   Adams, C.J., et al., *Structure and Molecular Mechanism of ER Stress Signaling by the Unfolded Protein Response Signal Activator IRE1.* Front Mol Biosci, 2019. **6**: p. 11.

11.   Hetz, C., K. Zhang, and R.J. Kaufman, *Mechanisms, regulation and functions of the unfolded protein response.* Nat Rev Mol Cell Biol, 2020. **21**(8): p. 421-438.

12.   Hu, H., et al., *The C/EBP Homologous Protein (CHOP) Transcription Factor Functions in Endoplasmic Reticulum Stress-Induced Apoptosis and Microbial Infection.* Front Immunol, 2018. **9**: p. 3083.

13.   Walter, P. and D. Ron, *The unfolded protein response: from stress pathway to homeostatic regulation.* Science, 2011. **334**(6059): p. 1081-6.

14.   Kato, H., et al., *ER-resident sensor PERK is essential for mitochondrial thermogenesis in brown adipose tissue.* Life Sci Alliance, 2020. **3**(3).

15.   Lee, A.S., *Glucose-regulated proteins in cancer: molecular mechanisms and therapeutic potential.* Nat Rev Cancer, 2014. **14**(4): p. 263-76.

16.   Coelho, D.S. and P.M. Domingos, *Physiological roles of regulated Ire1 dependent decay.* Front Genet, 2014. **5**: p. 76.

17.   Huang, J., et al., *High expression of active ATF6 aggravates endoplasmic reticulum stress-induced vascular endothelial cell apoptosis through the mitochondrial apoptotic pathway.* Mol Med Rep, 2018. **17**(5): p. 6483-6489.

18.   Doyle, K.M., et al., *Unfolded proteins and endoplasmic reticulum stress in neurodegenerative disorders.* J Cell Mol Med, 2011. **15**(10): p. 2025-39.

19.   Szegezdi, E., et al., *Mediators of endoplasmic reticulum stress-induced apoptosis.* EMBO Rep, 2006. **7**(9): p. 880-5.

20.   Hillary, R.F. and U. FitzGerald, *A lifetime of stress: ATF6 in development and homeostasis.* J Biomed Sci, 2018. **25**(1): p. 48.

21.   Turk, B. and V. Turk, *Lysosomes as "suicide bags" in cell death: myth or reality?* J Biol Chem, 2009. **284**(33): p. 21783-21787.

22.   Trivedi, P.C., J.J. Bartlett, and T. Pulinilkunnil, *Lysosomal Biology and Function: Modern View of Cellular Debris Bin.* Cells, 2020. **9**(5).

23.   Ballabio, A. and J.S. Bonifacino, *Lysosomes as dynamic regulators of cell and organismal homeostasis.* Nat Rev Mol Cell Biol, 2020. **21**(2): p. 101-118.

24.   Inpanathan, S. and R.J. Botelho, *The Lysosome Signaling Platform: Adapting With the Times.* Front Cell Dev Biol, 2019. **7**: p. 113.

25.   Perera, R.M. and R. Zoncu, *The Lysosome as a Regulatory Hub.* Annu Rev Cell Dev Biol, 2016. **32**: p. 223-253.

26.   Wang, N., et al., *Combining different types of multifunctional liposomes loaded with ammonium bicarbonate to fabricate microneedle arrays as a vaginal mucosal vaccine adjuvant-dual delivery system (VADDS).* J Control Release, 2017. **246**: p. 12-29.

27.   Stefan, C.J., et al., *Membrane dynamics and organelle biogenesis-lipid pipelines and vesicular carriers.* BMC Biol, 2017. **15**(1): p. 102.

28.   Palmieri, M., et al., *Characterization of the CLEAR network reveals an integrated control of cellular clearance pathways.* Hum Mol Genet, 2011. **20**(19): p. 3852-66.

29.   Settembre, C. and D.L. Medina, *TFEB and the CLEAR network.* Methods Cell Biol, 2015. **126**: p. 45-62.

30.   Platt, F.M., et al., *Lysosomal storage diseases.* Nat Rev Dis Primers, 2018. **4**(1): p. 27.

31.   *StatPearls*. 2021.

32.   Platt, F.M., *Emptying the stores: lysosomal diseases and therapeutic strategies.* Nat Rev Drug Discov, 2018. **17**(2): p. 133-150.

33.   Sun, A., *Lysosomal storage disease overview.* Ann Transl Med, 2018. **6**(24): p. 476.

34.   Linari, S. and G. Castaman, *Clinical manifestations and management of Gaucher disease.* Clin Cases Miner Bone Metab, 2015. **12**(2): p. 157-64.

35.   Demir, S.A., et al., *GM2 ganglioside accumulation causes neuroinflammation and behavioral alterations in a mouse model of early onset Tay-Sachs disease.* J Neuroinflammation, 2020. **17**(1): p. 277.

36.   Liu, E.A. and A.P. Lieberman, *The intersection of lysosomal and endoplasmic reticulum calcium with autophagy defects in lysosomal diseases.* Neurosci Lett, 2019. **697**: p. 10-16.

37.   Toledano-Zaragoza, A. and M.D. Ledesma, *Addressing neurodegeneration in lysosomal storage disorders: Advances in Niemann Pick diseases.* Neuropharmacology, 2020. **171**: p. 107851.

38.   Rebiai, R., et al., *Synaptic Function and Dysfunction in Lysosomal Storage Diseases.* Front Cell Neurosci, 2021. **15**: p. 619777.

39.   Gleichmann, M. and M.P. Mattson, *Neuronal calcium homeostasis and dysregulation.* Antioxid Redox Signal, 2011. **14**(7): p. 1261-73.

40.   Sun, A., et al., *Lysosomal Storage Disorders*, in *Emery and Rimoin's Principles and Practice of Medical Genetics and Genomics*. 2021, Elsevier. p. 563-682.

41.   Delnooz, C.C., et al., *New cases of adult-onset Sandhoff disease with a cerebellar or lower motor neuron phenotype.* J Neurol Neurosurg Psychiatry, 2010. **81**(9): p. 968-72.

42.   Leal, A.F., et al., *GM2 Gangliosidoses: Clinical Features, Pathophysiological Aspects, and Current Therapies.* Int J Mol Sci, 2020. **21**(17).

43.   Jamrozik, Z., et al., *Late onset GM2 gangliosidosis mimicking spinal muscular atrophy.* Gene, 2013. **527**(2): p. 679-82.

44.   Huang, J.Q., et al., *Apoptotic cell death in mouse models of GM2 gangliosidosis and observations on human Tay-Sachs and Sandhoff diseases.* Hum Mol Genet, 1997. **6**(11): p. 1879-85.

45.   Alonso-Pérez, J., et al., *Late onset Sandhoff disease presenting with lower motor neuron disease and stuttering.* Neuromuscular Disorders, 2021.

46.   Yokoyama, M., E.G. Trams, and R.O. Brady, *Sphingolipid antibodies in sera of animals and patients with central nervous system lesions.* Proc Soc Exp Biol Med, 1962. **111**: p. 350-2.

47.   Kohno, Y., et al., *[Adult Sandhoff disease presented as a motor neuron disease phenotype with slow progression].* Rinsho Shinkeigaku, 2001. **41**(1): p. 36-9.

48.   Takado, Y., et al., *[A patient with GM2 gangliosidosis presenting with motor neuron disease symptom in his forties].* Rinsho Shinkeigaku, 2007. **47**(1): p. 37-41.

49.   Khoueiry, M., E. Malek, and J.S. Salameh, *Adult onset Sandhoff disease: a rare mimicker of amyotrophic lateral sclerosis.* Amyotroph Lateral Scler Frontotemporal Degener, 2020. **21**(1-2): p. 144-146.

50.   Shibuya, M., et al., *A 23-year follow-up report of juvenile-onset Sandhoff disease presenting with a motor neuron disease phenotype and a novel variant.* Brain Dev, 2021. **43**(10): p. 1029-1032.

51.   Yokoyama, T., et al., *Late onset GM2 gangliosidosis presenting with motor neuron disease: an autopsy case.* Neuropathology, 2014. **34**(3): p. 304-8.

52.   Scarpelli, M., et al., *Natural history of motor neuron disease in adult onset GM2-gangliosidosis: A case report with 25 years of follow-up.* Mol Genet Metab Rep, 2014. **1**: p. 269-272.

53.   Cachon-Gonzalez, M.B., et al., *Reversibility of neuropathology in Tay-Sachs-related diseases.* Hum Mol Genet, 2014. **23**(3): p. 730-48.

54.   Sango, K., et al., *Mouse models of Tay-Sachs and Sandhoff diseases differ in neurologic phenotype and ganglioside metabolism.* Nat Genet, 1995. **11**(2): p. 170-6.

55.   Phaneuf, D., et al., *Dramatically different phenotypes in mouse models of human Tay-Sachs and Sandhoff diseases.* Hum Mol Genet, 1996. **5**(1): p. 1-14.

56.   Lawson, C.A. and D.R. Martin, *Animal models of GM2 gangliosidosis: utility and limitations.* Appl Clin Genet, 2016. **9**: p. 111-20.

57.   Osseward, P.J., 2nd and S.L. Pfaff, *Cell type and circuit modules in the spinal cord.* Curr Opin Neurobiol, 2019. **56**: p. 175-184.

58.   Felten, D.L. and A. Shetty, *Netter's Atlas of Neuroscience E-Book: with STUDENT CONSULT Online Access*. 2011: Elsevier Health Sciences.

59.   Bican, O., A. Minagar, and A.A. Pruitt, *The spinal cord: a review of functional neuroanatomy.* Neurol Clin, 2013. **31**(1): p. 1-18.

60.   Russ, D.E., et al., *A Harmonized Atlas of Spinal Cord Cell Types and Their Computational Classification.* bioRxiv, 2020.

61.   Lu, D.C., T. Niu, and W.A. Alaynick, *Molecular and cellular development of spinal cord locomotor circuitry.* Front Mol Neurosci, 2015. **8**: p. 25.

62.   Alaynick, W.A., T.M. Jessell, and S.L. Pfaff, *SnapShot: spinal cord development.* Cell, 2011. **146**(1): p. 178-178 e1.

63.   Holzer, H.T., et al., *Cerebellar atrophy on top of motor neuron compromise as indicator of late-onset GM2 gangliosidosis.* J Neurol, 2021.

64.   Schnorf, H., et al., *Early and severe sensory loss in three adult siblings with hexosaminidase A and B deficiency (Sandhoff disease).* J Neurol Neurosurg Psychiatry, 1995. **59**(5): p. 520-3.

65.   Bellettato, C.M. and M. Scarpa, *Pathophysiology of neuropathic lysosomal storage disorders.* J Inherit Metab Dis, 2010. **33**(4): p. 347-62.

66.   Pelled, D., et al., *Inhibition of calcium uptake via the sarco/endoplasmic reticulum Ca2+-ATPase in a mouse model of Sandhoff disease and prevention by treatment with N-butyldeoxynojirimycin.* J Biol Chem, 2003. **278**(32): p. 29496-501.

67.   Bosch, M.E. and T. Kielian, *Neuroinflammatory paradigms in lysosomal storage diseases.* Front Neurosci, 2015. **9**: p. 417.

68.   Tessitore, A., et al., *GM1-ganglioside-mediated activation of the unfolded protein response causes neuronal death in a neurodegenerative gangliosidosis.* Mol Cell, 2004. **15**(5): p. 753-66.

69.   Abo-Ouf, H., et al., *Deletion of tumor necrosis factor-alpha ameliorates neurodegeneration in Sandhoff disease mice.* Hum Mol Genet, 2013. **22**(19): p. 3960-75.

70.   Wada, R., C.J. Tifft, and R.L. Proia, *Microglial activation precedes acute neurodegeneration in Sandhoff disease and is suppressed by bone marrow transplantation.* Proc Natl Acad Sci U S A, 2000. **97**(20): p. 10954-9.

71. Suzuki, K., et al., *Mice deficient in all forms of lysosomal beta-hexosaminidase show mucopolysaccharidosis-like pathology.* J Neuropathol Exp Neurol, 1997. **56**(6): p. 693-703.

72. Walkley, S.U., et al., *Distribution of ectopic neurite growth and other geometrical distortions of CNS neurons in feline GM2 gangliosidosis.* Brain Res, 1990. **510**(1): p. 63-73.

73. Pará, C., P. Bose, and A.V. Pshezhetsky, *Neuropathophysiology of Lysosomal Storage Diseases: Synaptic Dysfunction as a Starting Point for Disease Progression.* J Clin Med, 2020. **9**(3).

74. Wang, Y., M. Song, and F. Song, *Neuronal autophagy and axon degeneration.* Cell Mol Life Sci, 2018. **75**(13): p. 2389-2406.

75. Ivanova, M.M., et al., *Impaired autophagic and mitochondrial functions are partially restored by ERT in Gaucher and Fabry diseases.* PLoS One, 2019. **14**(1): p. e0210617.

76. Kiselyov, K., et al., *Autophagy, mitochondria and cell death in lysosomal storage diseases.* Autophagy, 2007. **3**(3): p. 259-62.

77. Kiselyov, K. and S. Muallem, *Mitochondrial Ca2+ homeostasis in lysosomal storage diseases.* Cell Calcium, 2008. **44**(1): p. 103-11.

78. Annunziata, I., R. Sano, and A. d'Azzo, *Mitochondria-associated ER membranes (MAMs) and lysosomal storage diseases.* Cell Death Dis, 2018. **9**(3): p. 328.

79. Sabatini, D.D. and M. Adesnik, *Christian de Duve: Explorer of the cell who discovered new organelles by using a centrifuge.* Proc Natl Acad Sci U S A, 2013. **110**(33): p. 13234-5.

80. Wang, F., R. Gomez-Sintes, and P. Boya, *Lysosomal membrane permeabilization and cell death.* Traffic, 2018. **19**(12): p. 918-931.

81. Ono, K., S.O. Kim, and J. Han, *Susceptibility of lysosomes to rupture is a determinant for plasma membrane disruption in tumor necrosis factor alpha-induced cell death.* Mol Cell Biol, 2003. **23**(2): p. 665-76.

82. Aits, S. and M. Jaattela, *Lysosomal cell death at a glance.* J Cell Sci, 2013. **126**(Pt 9): p. 1905-12.

83. Raffaello, A., et al., *Calcium at the Center of Cell Signaling: Interplay between Endoplasmic Reticulum, Mitochondria, and Lysosomes.* Trends Biochem Sci, 2016. **41**(12): p. 1035-1049.

84. La Rovere, R.M., et al., *Intracellular Ca(2+) signaling and Ca(2+) microdomains in the control of cell survival, apoptosis and autophagy.* Cell Calcium, 2016. **60**(2): p. 74-87.

85. Feng, X. and J. Yang, *Lysosomal Calcium in Neurodegeneration.* Messenger (Los Angel), 2016. **5**(1-2): p. 56-66.

86. Austin, R.C., *The unfolded protein response in health and disease.* Antioxid Redox Signal, 2009. **11**(9): p. 2279-87.

87.   Park, S.J., C. Li, and Y.M. Chen, *Endoplasmic Reticulum Calcium Homeostasis in Kidney Disease: Pathogenesis and Therapeutic Targets.* Am J Pathol, 2021. **191**(2): p. 256-265.

88.   Feng, X., et al., *Lysosomal Potassium Channels: Potential Roles in Lysosomal Function and Neurodegenerative Diseases.* CNS Neurol Disord Drug Targets, 2018. **17**(4): p. 261-266.

89.   Kiselyov, K., et al., *Aberrant Ca2+ handling in lysosomal storage disorders.* Cell Calcium, 2010. **47**(2): p. 103-11.

90.   Tessitore, A., et al., *GM1-ganglioside-mediated activation of the unfolded protein response causes neuronal death in a neurodegenerative gangliosidosis.* Mol Cell, 2004. **15**(5): p. 753-66.

91.   Ginzburg, L. and A.H. Futerman, *Defective calcium homeostasis in the cerebellum in a mouse model of Niemann-Pick A disease.* J Neurochem, 2005. **95**(6): p. 1619-28.

92.   Tedeschi, V., T. Petrozziello, and A. Secondo, *Calcium Dyshomeostasis and Lysosomal Ca(2+) Dysfunction in Amyotrophic Lateral Sclerosis.* Cells, 2019. **8**(10).

93.   Lloyd-Evans, E., et al., *Niemann-Pick disease type C1 is a sphingosine storage disease that causes deregulation of lysosomal calcium.* Nat Med, 2008. **14**(11): p. 1247-55.

94.   Lloyd-Evans, E. and F.M. Platt, *Lysosomal Ca(2+) homeostasis: role in pathogenesis of lysosomal storage diseases.* Cell Calcium, 2011. **50**(2): p. 200-5.

95.   Christensen, K.A., J.T. Myers, and J.A. Swanson, *pH-dependent regulation of lysosomal calcium in macrophages.* J Cell Sci, 2002. **115**(Pt 3): p. 599-607.

96.   Garrity, A.G., et al., *The endoplasmic reticulum, not the pH gradient, drives calcium refilling of lysosomes.* Elife, 2016. **5**.

97.   Ronco, V., et al., *A novel Ca²⁺-mediated cross-talk between endoplasmic reticulum and acidic organelles: implications for NAADP-dependent Ca²⁺ signalling.* Cell Calcium, 2015. **57**(2): p. 89-100.

98.   Wang, Y., Y. Shi, and H. Wei, *Calcium Dysregulation in Alzheimer's Disease: A Target for New Drug Development.* J Alzheimers Dis Parkinsonism, 2017. **7**(5).

99.   Grosskreutz, J., L. Van Den Bosch, and B.U. Keller, *Calcium dysregulation in amyotrophic lateral sclerosis.* Cell Calcium, 2010. **47**(2): p. 165-74.

100.   Schapira, A.H., *Calcium dysregulation in Parkinson's disease.* Brain, 2013. **136**(Pt 7): p. 2015-6.

101.   Shen, D., et al., *Lipid storage disorders block lysosomal trafficking by inhibiting a TRP channel and lysosomal calcium release.* Nat Commun, 2012. **3**: p. 731.

102.   Wei, H., et al., *ER and oxidative stresses are common mediators of apoptosis in both neurodegenerative and non-neurodegenerative lysosomal storage disorders and are alleviated by chemical chaperones.* Hum Mol Genet, 2008. **17**(4): p. 469-77.

103. Rao, R.V., et al., *Coupling endoplasmic reticulum stress to the cell death program: role of the ER chaperone GRP78.* FEBS Lett, 2002. **514**(2-3): p. 122-8.

104. d'Azzo, A., A. Tessitore, and R. Sano, *Gangliosides as apoptotic signals in ER stress response.* Cell Death Differ, 2006. **13**(3): p. 404-14.

105. Virgolini, M.J., et al., *Neurite atrophy and apoptosis mediated by PERK signaling after accumulation of GM2-ganglioside.* Biochim Biophys Acta Mol Cell Res, 2019. **1866**(2): p. 225-239.

106. Sano, R. and J.C. Reed, *ER stress-induced cell death mechanisms.* Biochim Biophys Acta, 2013. **1833**(12): p. 3460-3470.

107. Sevier, C.S. and C.A. Kaiser, *Ero1 and redox homeostasis in the endoplasmic reticulum.* Biochim Biophys Acta, 2008. **1783**(4): p. 549-56.

108. Oyadomari, S. and M. Mori, *Roles of CHOP/GADD153 in endoplasmic reticulum stress.* Cell Death Differ, 2004. **11**(4): p. 381-9.

109. Rasheva, V.I. and P.M. Domingos, *Cellular responses to endoplasmic reticulum stress and apoptosis.* Apoptosis, 2009. **14**(8): p. 996-1007.

110. Lamkanfi, M. and T.D. Kanneganti, *Caspase-7: a protease involved in apoptosis and inflammation.* Int J Biochem Cell Biol, 2010. **42**(1): p. 21-4.

111. Rao, R.V., et al., *Coupling endoplasmic reticulum stress to the cell death program. Mechanism of caspase activation.* J Biol Chem, 2001. **276**(36): p. 33869-74.

112. Kobolák, J., et al., *Modelling the neuropathology of lysosomal storage disorders through disease-specific human induced pluripotent stem cells.* Exp Cell Res, 2019. **380**(2): p. 216-233.

113. Sano, R., et al., *GM1-ganglioside accumulation at the mitochondria-associated ER membranes links ER stress to Ca(2+)-dependent mitochondrial apoptosis.* Mol Cell, 2009. **36**(3): p. 500-11.

114. Marques, A.R.A., et al., *Enzyme replacement therapy with recombinant pro-CTSD (cathepsin D) corrects defective proteolysis and autophagy in neuronal ceroid lipofuscinosis.* Autophagy, 2019: p. 1-15.

115. Platt, F.M. and T.D. Butters, *Substrate deprivation: a new therapeutic approach for the glycosphingolipid lysosomal storage diseases.* Expert Rev Mol Med, 2000. **2**(1): p. 1-17.

116. Platt, F.M. and M. Jeyakumar, *Substrate reduction therapy.* Acta Paediatr, 2008. **97**(457): p. 88-93.

117. Jeyakumar, M., et al., *Enhanced survival in Sandhoff disease mice receiving a combination of substrate deprivation therapy and bone marrow transplantation.* Blood, 2001. **97**(1): p. 327-9.

118. Jeyakumar, M., et al., *Delayed symptom onset and increased life expectancy in Sandhoff disease mice treated with N-butyldeoxynojirimycin.* Proc Natl Acad Sci U S A, 1999. **96**(11): p. 6388-93.

119. Jakobkiewicz-Banecka, J., A. Wegrzyn, and G. Wegrzyn, *Substrate deprivation therapy: a new hope for patients suffering from neuronopathic forms of inherited lysosomal storage diseases.* J Appl Genet, 2007. **48**(4): p. 383-8.

120. Beck, M., *New therapeutic options for lysosomal storage disorders: enzyme replacement, small molecules and gene therapy.* Hum Genet, 2007. **121**(1): p. 1-22.

121. McCafferty, E.H. and L.J. Scott, *Migalastat: A Review in Fabry Disease.* Drugs, 2019. **79**(5): p. 543-554.

122. Rovelli, A.M., *The controversial and changing role of haematopoietic cell transplantation for lysosomal storage disorders: an update.* Bone Marrow Transplant, 2008. **41 Suppl 2**: p. S87-9.

123. Jeyakumar, M., et al., *NSAIDs increase survival in the Sandhoff disease mouse: synergy with N-butyldeoxynojirimycin.* Ann Neurol, 2004. **56**(5): p. 642-9.

124. Gao, H.M., et al., *Novel anti-inflammatory therapy for Parkinson's disease.* Trends Pharmacol Sci, 2003. **24**(8): p. 395-401.

125. Nagree, M.S., et al., *An update on gene therapy for lysosomal storage disorders.* Expert Opin Biol Ther, 2019. **19**(7): p. 655-670.

126. Ohashi, T., *Gene therapy for lysosomal storage diseases and peroxisomal diseases.* J Hum Genet, 2019. **64**(2): p. 139-143.

127. Edelmann, M.J. and G.H.B. Maegawa, *CNS-Targeting Therapies for Lysosomal Storage Diseases: Current Advances and Challenges.* Front Mol Biosci, 2020. **7**: p. 559804.

128. Saffari, A., et al., *[Gene therapies for neuromuscular diseases].* Nervenarzt, 2019. **90**(8): p. 809-816.

129. Hakomori, S., *Organization and function of glycosphingolipids in membrane.* Proceedings of the Japan Academy, Series B, 2005. **81**(6): p. 189-203.

130. Regina Todeschini, A. and S.I. Hakomori, *Functional role of glycosphingolipids and gangliosides in control of cell adhesion, motility, and growth, through glycosynaptic microdomains.* Biochim Biophys Acta, 2008. **1780**(3): p. 421-33.

131. Sasaki, N., et al., *Ganglioside GM2, highly expressed in the MIA PaCa-2 pancreatic ductal adenocarcinoma cell line, is correlated with growth, invasion, and advanced stage.* Sci Rep, 2019. **9**(1): p. 19369.

132. Guégan, C. and S. Przedborski, *Programmed cell death in amyotrophic lateral sclerosis.* J Clin Invest, 2003. **111**(2): p. 153-61.

133. Li, Q., et al., *The cleavage pattern of TDP-43 determines its rate of clearance and cytotoxicity.* Nat Commun, 2015. **6**: p. 6183.

134. Lindner, P., et al., *Cell death induced by the ER stressor thapsigargin involves death receptor 5, a non-autophagic function of MAP1LC3B, and distinct contributions from unfolded protein response components.* Cell Commun Signal, 2020. **18**(1): p. 12.

135.   Tay, K.H., et al., *Sustained IRE1 and ATF6 signaling is important for survival of melanoma cells undergoing ER stress.* Cell Signal, 2014. **26**(2): p. 287-94.

136.   Sharma, R.B., J.T. Snyder, and L.C. Alonso, *Atf6α impacts cell number by influencing survival, death and proliferation.* Mol Metab, 2019. **27S**: p. S69-S80.

137.   Yang, H., et al., *ATF6 Is a Critical Determinant of CHOP Dynamics during the Unfolded Protein Response.* iScience, 2020. **23**(2): p. 100860.

138.   Brentnall, M., et al., *Caspase-9, caspase-3 and caspase-7 have distinct roles during intrinsic apoptosis.* BMC Cell Biol, 2013. **14**: p. 32.

139.   Wang, M., et al., *Role of the unfolded protein response regulator GRP78/BiP in development, cancer, and neurological disorders.* Antioxid Redox Signal, 2009. **11**(9): p. 2307-16.

140.   Zhang, Y., et al., *Cell surface relocalization of the endoplasmic reticulum chaperone and unfolded protein response regulator GRP78/BiP.* J Biol Chem, 2010. **285**(20): p. 15065-15075.

141.   Louessard, M., et al., *Activation of cell surface GRP78 decreases endoplasmic reticulum stress and neuronal death.* Cell Death Differ, 2017. **24**(9): p. 1518-1529.

142.   Reddy, R.K., et al., *Endoplasmic reticulum chaperone protein GRP78 protects cells from apoptosis induced by topoisomerase inhibitors: role of ATP binding site in suppression of caspase-7 activation.* J Biol Chem, 2003. **278**(23): p. 20915-24.

143.   Liu, Y., et al., *Downregulation of GRP78 and XIAP is correlated with apoptosis during cerulein-induced acute pancreatitis in rats via regulation of caspase activation.* Mol Med Rep, 2013. **7**(3): p. 725-30.